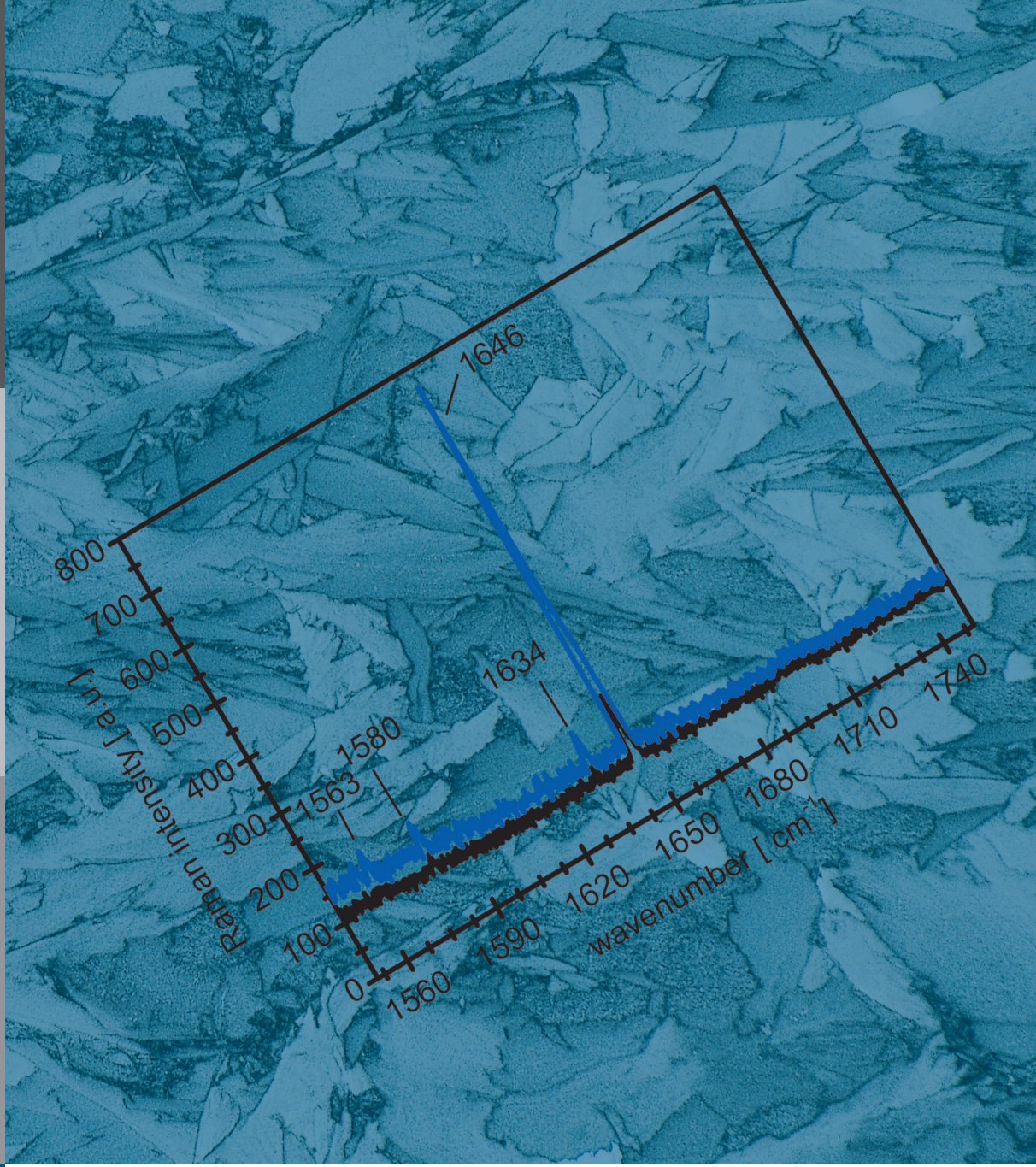

Electromechanical Force Microscopy and Tip-Enhanced Raman Spectroscopy for Polar Oxide Nanoparticles

Serge Röhrig

JÜLICH
FORSCHUNGSZENTRUM

Mitglied der Helmholtz-Gemeinschaft

Schriften des Forschungszentrums Jülich
Reihe Information / Information Band / Volume 7

Forschungszentrum Jülich GmbH
Institute of Solid State Research (IFF)
Electronic Materials (IFF-6)

Electromechanical Force Microscopy and Tip-Enhanced Raman Spectroscopy for Polar Oxide Nanoparticles

Serge Röhrig

Schriften des Forschungszentrums Jülich
Reihe Information / Information Band / Volume 7

ISSN 1866-1777 ISBN 978-3-89336-600-2

Bibliographic information published by the Deutsche Nationalbibliothek.
The Deutsche Nationalbibliothek lists this publication in the Deutsche Nationalbibliografie; detailed bibliographic data are available in the Internet at http://dnb.d-nb.de.

Publisher and Distributor: Forschungszentrum Jülich GmbH
Zentralbibliothek, Verlag
D-52425 Jülich
phone:+49 2461 61-5368 · fax:+49 2461 61-6103
e-mail: zb-publikation@fz-juelich.de
Internet: http://www.fz-juelich.de/zb

Cover Design: Grafische Medien, Forschungszentrum Jülich GmbH

Printer: Grafische Medien, Forschungszentrum Jülich GmbH

Schriften des Forschungszentrums Jülich
Reihe Information / Information Band / Volume 7

D 82 (Diss., RWTH Aachen, Univ., 2009)

ISSN 1866-1777
ISBN 978-3-89336-600-2

The complete volume is freely available on the Internet on the Jülicher Open Access Server (JUWEL) at http://www.fz-juelich.de/zb/juwel

Contents

1 Introduction

1.1 Motivation

Polar oxides cover an increasingly wide range of applications due to their fascinating properties as piezoelectricity, pyroelectricity, and for the materials under investigation in this work also ferroelectricity. These applications range from basic electromechanical transducers in common-rail Diesel engines to ultrasonic sensors in medical devices in the case of piezoelectrics, from motion detection systems to thermal imaging cameras in the case of pyroelectrics, and different non-volatile memory devices in the case of ferroelectrics which rely on remanent polarization [1–4].

The driving forces for the improvement of this class of materials are manifold. Crucial macroscopic material parameters such as the polarization and the coercive field are persistently subject to investigation including the possibilities and improvements of the detection and quantification of these parameters. Considerable effort is devoted to novel deposition techniques to enable or facilitate CMOS-compatibility in terms of the thermal budget, and even completely new materials are investigated in terms of environmentally neutral components or multiferroic behavior i.e. the coexistence of more than one ferroic property (ferromagnetism, -electricity or -elasticity) [5]. It comes as no surprise that the understanding of piezoelectricity, pyroelectricity and ferroelectricity and their associated microscopic manifestations (e.g. crystal symmetry, phonon spectra) is the key to novel devices, better performance and completely new fields of applications.

Scanning force microscopy and especially piezoresponse force microscopy (PFM) has proven to be a powerful tool for the investigations of these materials and its properties. PFM uses the linear electromechanical response of a sample to locally determine the relative orientation of the third rank piezoelectric tensor and therefore the orientation of the polarization. Previous work on the quantification of PFM data did not succeed to eliminate all doubts about the actual numbers derived from PFM images or piezoelectric hysteresis loops obtained with this method [6, 7]. This can mainly be attributed to the effect of sample topography that frequently provides coupling to more piezoelectric tensor elements than initially assumed and adsorbates that act as a voltage divider. As many other scanning probe techniques, PFM already provides superb lateral resolution and is now shifting focus into the time domain and is looking for new fields of application like biomaterials that exhibit piezoelectricity. With respect to the time domain, two different approaches are pursued. Gruverman eliminates topography effects with a macroscopic top electrode and applies a boxcar technique to sample the temporal development of domain nucleation and propagation over several orders of magnitude ranging from several dozen nanoseconds to seconds [8]. This method relies on the assumption that relaxation of

the domain structure is slow compared to the scan speed. Other groups are following the idea to directly enhance the scan speed of PFM to obtain at least the time resolution of several dozen frames per second as monitored with other AFM techniques. PFM however, being inherently a contact mode microscopy strongly depends on the cantilever dynamics. With the choice of an appropriate cantilever the dynamic response can be optimized. This work however highlights the omnipresent effect of domain-specific adsorbates on the phase contrast of PFM images, an effect that cannot be bypassed by the choice of the cantilever. Instead of looking for novel piezoelectric materials to extend the scope of PFM, this work succeeded to apply a slightly modified method to centrosymmetric crystal classes as well, thus entirely eliminating the restrictions imposed by PFM to non-centrosymmetric samples. No hardware modifications are required as the electrostriction of the material under investigation is explored and provides similar sensitivity and lateral resolution as PFM.

Piezoresponse force microscopy relies on the deformation under an applied voltage (units of the piezoelectric tensor being pm/V) and it follows from the need for a minimal detectable deformation that a minimal voltage has to be applied. Especially with ultrathin structures this voltage may correspond to an electric field that already exceeds coercivity. A section of this work is devoted to the investigation of the sample scanning conditions as the scanning voltage exceeds the coercive field. This additional insight obtained by this approach comprises a novel detection scheme for the coercive field and may at a later point provide a novel detection scheme for polarization reversal. In any case it already allows the identification of ”switching upon scanning”which in many measurements will help to clarify the lack of domain contrast.

In the quest for an ultimate size limit below which ferroelectricity can no longer be sustained, any claim to have found such a limit only holds true until it is experimentally crossed [9]. In that sense all techniques that provide digital information (ferroelectric or not) need to be questioned with respect to their sensitivity and this work revisits data from piezoresponse force imaging [10], pyroelectric imaging [11], and impedance studies [12]. This and the limitations of PFM clarify the need of other detection methods of ferroelectricity for small structures and thin films. For $PbTiO_3$ thin films the critical thickness, where the polarization is zero, at room temperature is estimated to two unit cells by x-ray scattering [13, 14]. This method is suitable for thin films but suffers from a poor lateral resolution. Yet another method to explore structural prerequisites of ferroelectricity is Raman spectroscopy. Tetragonality is expressed as a loss of vibrational degeneracy and in addition the study of soft mode phonons in ferroelectrics is possible. Moreover soft mode analysis provides a quantitative fingerprint of the proximity of a size driven phase transition. The feasibility of this technique has been shown by Ishikawa [15] on an ensemble of ferroelectric lead titanate nanograins. However, these structures are electrostatically coupled so it is desirable to investigate them one by one. Raman spectroscopy itself does neither yield sufficient cross-section for nanoparticle sensitivity nor sufficient lat-

eral resolution. With tip-enhanced Raman spectroscopy (TERS) both targets can be aimed at simultaneously. Since all materials under investigation are insulators, the established approach of scanning tunnelling based TERS was transferred to non-contact mode AFM.

1.2 Literature

As the use of PFM as an imaging tool for ferroelectric nanostructures becomes more and more popular, the development is driving into different directions. Kalinin and coworkers are pushing the limits towards a complete mapping of the ferroelectric properties as they are taking a complete piezoelectric hysteresis loop at every single image point, which in principle enables them to map the local coercive field and the work of polarization reversal [16]. Taking the findings of Peter et al. [17] on the effect of adsorbates, the absolute figures are questionable but with the assumption of a homogeneous layer of adsorbates, this technique certainly gives a good impression of relative local variations. The group of Kalinin put a lot of effort into the investigation of the local interaction between tip and sample [18], however the equations are often lacking an analytical solution and the numerical approximations yield results that are similar to finite element studies [19].Scanning probe techniques in general are shifting into real-time imaging which can be achieved by box-car techniques [8] as long as the relaxation to the initial state can be omitted or by sufficiently fast imaging. For the latter case, the lock-in frequency can easily be increased but at the same time the mechanical cantilever response due to electrostatic coupling will run through all possible resonances [20]. While the phase-jump at the resonance peak entirely obsures the phase information that otherwise reveals the relative domain orientation [21], the additional electrostatic phase shift reduces the domain phase contrast [22]. Moreover, the detection of higher harmonics of the excitation frequency allows for two interesting approaches [23]: the second harmonic contains contributions of the electrostatic interaction between tip and sample and the electrostrictive response that is represented by a forth-rank tensor and therefore not restricted by the crystal symmetry. As the sample thickness may now become as small as only a few unit cells [13], the required voltage for PFM of typically a few volts may already exceed the coercive field with the consequence of a complete loss of domain contrast as the sample is persistently switched upon scanning.
Several years ago, TERS [24] was introduced as a consequent application of the well-established surface enhanced Raman spectroscopy [25]. This optical near-field technique uses the resonant excitation of surface plasmon polaritons to create a field enhancement of several orders of magnitude in the very proximity of a noble-metal coated tip. The optical diffraction limit is bypassed and this apertureless microscopy allows for a lateral resolution as small as 12 nm [26]. At the same time the local intensity together with resonant Raman scattering provides single molecule sensitivity. At present this method is widely used for the detection of the radial

breathing modes in single-wall carbon nanotubes (SW-CNT) but restricted to STM tips. It is only since very recently that contact and non-contact mode AFM systems have been modified to investigate insulating systems [27].

1.3 Objectives

This work is devoted to the detection of ferroelectricity in polar oxides by scanning probe microscopy and comprises two main parts. The first part discusses electrical field based contact mode methods to explore the electromechanical response. Starting from piezoresponse force microscopy on ferroelectric nanostructures, earlier results on finite size effects are critically revisited [11,12]. Using PFM as an imaging technique for the existence and orientation of the polarization, this work comprises several investigations on novel material systems such as hollow $BaTiO_3$ nanoparticles and $NaNbO_3$ submicron powders. Furthermore the ongoing debate on non-stoichiometry of lead-based ferroelectrics is addressed in a PFM experiment. Unidentified segregation on top of lead zirconate titanate nanoparticles that were grown under a lead-oxide atmosphere do not show any piezoelectric signature. These additional particles are also visible in SEM scans on top of the nanoislands and their existence is completely in line with global XPS measurements that are averaging over the undistorted perovskite phase with a contribution of these inactive PbO_x nanoparticles. This is furthermore supported by high-resolution TEM images and very recent Nano-XPS measurements conducted at Bessy and Elletra.
In spite of all the achieved results with PFM, some crucial limitations are given by the influences of the topography of the sample and the adsorbates. These influences and limitations are discussed regarding the resulting amplitude due to adsorbates operating as a voltage divider, the accessible regions of the nanostructures, and the thickness dependent coercive field of the sample as well as the resulting phase difference between 180 $^{\circ}$ domains depending on the frequency of the applied voltage due to role of adsorbates in an AC circuit. This leads to restrictions for the investigation of very small nanostructures and ultrathin films by standard PFM, where the applied voltage has to remain below the coercive voltage.
Here the initially undesirable effect of a scanning voltage that exceeds the coercive field provides a new detection method for ferroelectricity in these thin structures coming along with the loss of phase information and therefore the orientation of the polarization. Furthermore it offers an interesting view on the point contact dynamics in PFM. A complete loss of the mechanical and therefore electrical contact as a function of the relative orientation between tip and polarization is shown and suggests a novel detection scheme for polarization reversal e.g. in ferroelectric mass storage devices. In addition, the detection of the local coercive field can be achieved by only applying an AC voltage in contrast to the measurements of hysteresis curves where an AC and Dc voltage is necessary. For every PFM measurement with an applied volt-

age leading to a resulting field above the coercive field on the sample the frequency dependence changes from the first to the second harmonic leading to a superposition with the electrostriction measured at the same frequency.
Furthermore the detection of the second harmonic of the electromechanical response (electrostriction) provides a fascinating generalization of the previous findings from Peter et al. [28] on how to image local heterogeneities. The fourth-rank tensor of electrostriction does not impose a restriction to the crystal symmetry of the sample and therefore can also be used for semiconductors such as silicon. Any local reduction of the global symmetry of the electric field underneath the tip adds a torque on the cantilever that can be monitored by a lateral torsion of the AFM cantilever.
The second section of this thesis addresses the design and the setup of a tip-enhanced Raman setup based on a non-contact mode AFM in ultrahigh vacuum, a joint project with the Zentralinstitut für Chemische Analysen at the Forschungszentrum Jülich. The particular requirements for a narrow focus with a long-working distance objective are sketched and first measurements of Raman-spectroscopy in UHV with this setup are discussed in terms of the effect of the vacuum conditions and their impact on the beam quality. This work also comprises the fabrication, characterization and optimization of silver-coated non-contact mode AFM-tips. First successful tip-enhanced Raman measurements in contact mode under ambient conditions with both, the gold-coated tips with a laser-excitation at 632.8 nm and the silver-coated tips with a wavelength of 488 nm provided an enhancement of approximately $5{\cdot}10^4$ and $1{\cdot}10^4$, respectively.

2 Ferroelectrics

This chapter is devoted to the fundamentals of ferroelectrics as far as they are relevant for this work. For a comprehensive approach the reader is referred to textbooks [29–33].

2.1 Ferroelectricity

Ferroelectricity was first observed in 1921 by J. Valasek investigating the anomalous dielectric properties of Rochelle Salt [34]. It is defined as a system with two or more discrete stable or metastable states of different nonzero electric polarization in absence of an applied electric field referred, to as "'spontaneous"‘ polarization, which has to be switchable by an external electric field.
In all known conventional ferroelectric crystals the spontaneous polarization stems from the atomic arrangement of ions in the crystal structure, depending on their positions. A nonzero spontaneous polarization can only exist in a crystal with a polar point group. Therefore a closer look on the crystallographic point groups is taken.
Depending on the symmetry, crystals are classified into one of the 32 point groups, see Fig. 2.1.

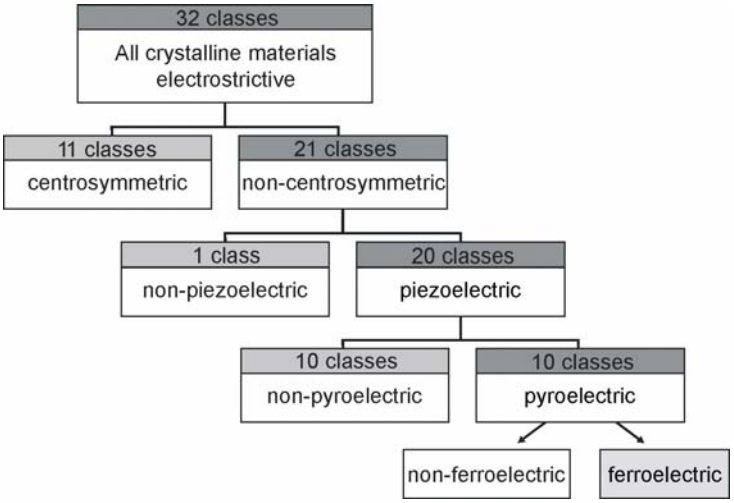

FIGURE 2.1: Block diagram of the 32 crystal classes (point groups). Twenty of the 21 non-centrosymmetric point groups are piezoelectric and 10 of them, the so-called polar point groups are also pyroelectric (with a spontaneous polarization). If this spontaneous polarization is reversible they are called ferroelectric, adapted from [10].

Eleven of these crystal classes possess a center of symmetry and therefore do not exhibit polar

properties. Twenty of the remaining 21 non-centrosymmetric groups exhibit the piezoelectric effect. Application of mechanical stress along selective crystal axes leads to surface charges and therefore an electric polarity. Vice versa, application of an electric field leads to a deformation of the unit-cell, see section 2.5.1[1].

A sub-group of 10 classes has a unique polar axis and exhibits a spontaneous polarization even without any mechanical stress or external electric field. In these materials a change in temperature leads to a deformation of the unit-cell along the polar axis, so the magnitude of the polarization is temperature-dependent. The effect is called pyroelectricity. Here also the inverse effect , the so-called electro-caloric effect exists.

The ferroelectric crystals are a subgroup of these pyroelectric crystals. In ferroelectrics the spontaneous polarization has two stable states and can be switched between each of them by an external electric field. In other words a ferroelectric switches below the breakdown voltage of the ionic crystal. The polarization reversal by the external field shows a hysteretic behavior

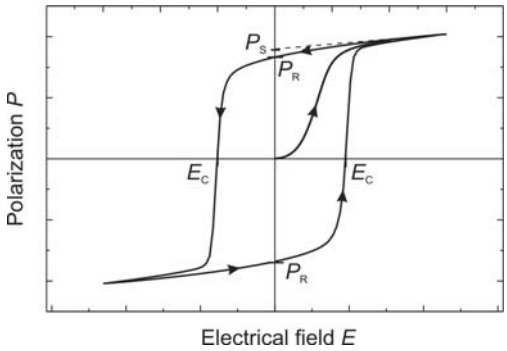

FIGURE 2.2: Sketch of the ferroelectric hysteresis loop with the characteristic points spontaneous P_s and remanent polarization P_r and the coercive field E_c [31]. The area of the curve is proportional to the volume energy density required for one switching cycle.

in the dependence of the polarization on the applied field as sketched in Fig. 2.2. For a non-polarized crystal the polar domains are randomly oriented and the overall polarization without an applied field is zero. For very small fields the material shows a normal dielectric behavior for the relation between the polarization and the electric field and reduction of the field leads to a decrease in the polarization. Increasing the value sufficiently will lead to a permanent polarization aligned along the field direction and a further increase will cause an asymptotic linear dependence of the polarization on the applied field. The polarization will now remain in this direction even for a decreasing field down to zero. The polarization measured for a zero field is the so-called remanent polarization P_r. To switch the polarization into the negative state

[1] Electrostriction converts an electrical field into a mechanical response without an inverse effect

an applied field in the negative direction is needed, which is called the coercive field E_c. The same field with an opposite direction is needed to switch the polarization back in the positive state and to close the hysteresis loop.

2.2 Phenomenology of ferroelectrics

2.2.1 Landau-Devonshire theory

Ferroelectric materials, in analogy to ferromagnetic materials, lose their spontaneous polarization due to a phase transition above a critical temperature, the so-called Curie temperature T_c. Above this temperature the crystal is paraelectric and the dielectric constant follows a Curie-Weiss-law in analogy to the ferromagnetic susceptibility [35]. The paraelectric phase can be piezoelectric or not and is rarely polar. This phase transition can be explained by the Landau-Devonshire theory which was established by Landau [36,37] and afterwards applied to the case of ferroelectrics by Devonshire [38–40] for poled bulk materials.
The thermodynamic state of any system in equilibrium can be completely specified by the values of specific variables. In the case of bulk ferroelectrics these include the temperature T, the polarization P, the electric field E, the strain η and the stress σ. The electric field and stress are external variables because they are applied and the strain and polarization are internal or dependent variables. Two fundamental principles of thermodynamics about the free energy F have to be taken into account, first that it can be generally expressed as a function of ten variables (three components of polarization, six components of stress tensor and one of temperature) and second that the values of the dependent variables in thermal equilibrium are obtained at the free-energy minimum when the free energy is optimized. Finally, approximating that in the vicinity of a phase transition the free energy can be expanded in powers of the dependent variables the following equation can be obtained

$$\mathcal{F}_P = \frac{1}{2}aP^2 + \frac{1}{4}bP^4 + \frac{1}{6}cP^6 - EP \tag{2.1}$$

The origin of energy for the free unpolarized, unstrained crystal is chosen to be zero.The coefficients *a*, *b*, *c* which can be fitted to experiment will be discussed shortly. Here the notation convention is used that $\mathcal{F}$ is the free energy density and the free energy F is given by $F = \int \mathcal{F} dV$. The equilibrium configuration is determined by finding the minima of $\mathcal{F}_P$, where we shall have

$$\frac{\partial \mathcal{F}_P}{\partial P} = 0 \tag{2.2}$$

From these equations the linear dielectric susceptibility above the transition can be obtained, setting $P = 0$

$$\chi = \frac{P}{E} = \frac{1}{a} \tag{2.3}$$

In the Landau-Devonshire theory it is assumed that around the Curie point (T$\sim$T$_0$)

$$a = a_0(T - T_0) \tag{2.4}$$

where T$_0$ is the Curie point temperature, leading to

$$\chi = \frac{1}{a_0(T - T_0)} \tag{2.5}$$

where the Curie-Weiss behavior can be seen. All other coefficients are temperature-independent and the temperature T_0 where *a* changes its sign is close to but not necessary the Curie temperature. Including the temperature dependence an expression for the free energy of

$$\mathcal{F}_P = \frac{1}{2}a_0(T - T_0)P^2 + \frac{1}{4}bP^4 + \frac{1}{6}cP^6 - EP \tag{2.6}$$

is given where *a* and *c* are positive for all known ferroelectrics [31,41]. So *b* will determine the nature of paraelectric-ferroelectric phase transition.
If *b*>0 a second-order i.e. continuous transition occurs. Since all coefficients are positive only the two lowest-order terms retain, leading to a spontaneous polarization (E=0) of

$$P_s = \sqrt{\left[\frac{a_0}{b}(T_0 - T)\right]} \tag{2.7}$$

and a susceptibility of

$$\chi = \frac{1}{2a_0(T_0 - T)} \tag{2.8}$$

It can clearly be seen that the spontaneous polarization is decreasing with increasing temperature and that the susceptibility diverges at $T = T_0$.
For *b*<0 a first-order i.e. discontinuous transition is taking place. With this negative coefficient the free energy may have a minimum even for $T > T_0$ at nonzero *P* with a lower energy and therefore thermodynamically favored over the unpolarized state. The temperature at which that happens is, per definition, $T_c > T_0$. The most important feature is that the order parameter jumps discontinuously to zero at T_c.

The procedure for finding the spontaneous polarization and the dielectric susceptibility is the same as before but now the higher order terms can not be neglected leading to a finite jump of both at the transition.
Independent of the order of the phase transition the two minima of the free energy in the ferroelectric phase with a barrier in between indicate the hysteresis for the switching of the polarization.
The other dependent variable, the strain, is given by the displacement $\vec{u}$ of a point in the solid varying with position $\vec{r}$

$$\eta_{ij} = \frac{1}{2}\left(\frac{\partial u_i}{\partial r_j} + \frac{\partial u_j}{\partial r_i}\right) \tag{2.9}$$

where *i* and *j* indicate the *x,y,z* direction. Concerning a special axis for the coupling of the polarization to the strain, the free energy can be written

$$\mathcal{F}_\eta = \frac{1}{2}K\eta^2 + Q\eta P^2 - \eta\sigma \tag{2.10}$$

Here K is the elastic constant. The total free energy is given by $\mathcal{F} = \mathcal{F}_P + \mathcal{F}_\eta$. Searching again for the minimum with the partial derivative of the strain and no applied external stresses leads to the term

$$\eta = -\frac{QP^2}{K} \tag{2.11}$$

So the tetragonal strain occurs proportional to the square of the polarization and we get a equation for the free energy

$$\mathcal{F}(P, \eta(P)) = \frac{1}{2}aP^2 + \frac{1}{4}(b - 2Q^2/K)P^4 + \frac{1}{6}cP^6 + ... - EP \tag{2.12}$$

In comparison to the clamped system, the only change is the reduce of the quartic coefficient, which means a raise in T_o for an already first-order transition or even a change in the transition from second to first order. Through the strong coupling between polarization and strain, the application of pressure can influence the transition temperature of bulk ferroelectrics. This is known for both hydrostatic [42] and biaxial [43] pressure. But most of the materials do not have a uniform polarization and for thin films or nanoislands the behavior diifers to that from a bulk. Therefore some extensions to this theory are necessary as described in the following section.

2.2.2 Landau-Ginzburg theory

In most materials domains, regions of different orientations of the polarization, are built for a lot of reasons like nonuniform strain, microscopic defects and thermal and electrical history. But even in ideal crystals domains are expected for energetic reasons:
The polarization is produced by the displacement of the positive barycenter relative to the negative one leading to a net charge at the surfaces of the the sample. The surface charge density is given by

$$\sigma = \vec{P} \cdot \vec{n} \tag{2.13}$$

where $\vec{n}$ is the vector normal to the boundary surface. These surface charges generate internal and external electric fields. To minimize the energy of the system, these fields have to be minimized as far as possible by building domains with an orientation of the polarization parallel to the surface, see Fig. 2.3.

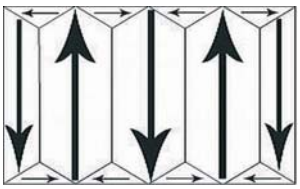

FIGURE 2.3: Domain configuration to minimize the stray field energy in a ferroelectric bulk material, [44].

This causes also domains in the bulk leading to polarization charges unless the walls are appropriately oriented. The interface charge density is given by

$$\sigma = (\vec{P}_1 - \vec{P}_2) \cdot \vec{n} \tag{2.14}$$

where $\vec{P}_1$ and $\vec{P}_2$ are the polarizations of the two domains. This surface charge density vanishes for two cases. First the antiparallel orientation parallel to the domain walls, the so called 180^o domains and second when the domain wall bisects the angle between two head-to-tail pointing domains, the so called 90^o domains. Another involved energy cost is due to the coupling of the polarization to strain, as shown before. So also the strain fields have to be taken into account, some extensions have to be done to the Landau-Devonshire theory. In order to apply the Landau theory to inhomogeneous and finite-size ferroelectrics the total free energy instead of the energy density should be used[2].

[2]The volume can no longer be considered homogenous but will contain surface or domain wall contributions

The so called Landau-Ginzburg theory includes small spatial variations of the order parameter, here the polarization. These small variations in the direction of the polarization lead to an additional contribution to the free-energy that is proportional to $(\nabla P)^2$.

$$F = \int_V [a_0(T-T_0)P^2(\vec{r}) + \frac{1}{4}(b-2Q^2/K)P^4(\vec{r}) + \frac{1}{6}cP^6 + \frac{1}{2}d(\nabla P^2) - \vec{E}\vec{P}(\vec{r})]dV \quad (2.15)$$

where d is connected to the correlation length ξ, $d = \xi^2|a_0(T-T_0)|$.
If now the size is reduced, which means that not a bulk material is investigated but for example a thin film or nanoislands, also the surface term of the free energy has to be taken into account. For the previous discussion of the bulk material the surface energy term is often neglected. With this additional term, the free energy can be written as [45]

$$\begin{aligned} F &= \int_V [a_0(T-T_0)P^2(\vec{r}) + \frac{1}{4}(b-2Q^2/K)P^4(\vec{r})\frac{1}{6}cP^6 + +\frac{1}{2}d(\nabla P^2) - \vec{E}\vec{P}(\vec{r})]dV + \\ &\quad \int_S \frac{1}{2}d\delta^{-1}P^2 dS \end{aligned} \quad (2.16)$$

where *S* is the surface area of the sample and δ the so called extrapolation length. The spontaneous polarization must satisfy the following Euler-Lagrange equation and boundary condition to minimize the free energy:

$$d\nabla^2 P = a_o(T-T_0)P + (b-2Q^2/K)P^3 + cP^5 \quad (2.17)$$

$$\frac{\partial P}{\partial n} + \delta^{-1}P = 0 \qquad \text{at the surface} \quad (2.18)$$

For simplicity, let us restrict to the case of an only z-dependent polarization in a thin film with the surface located at *z*=0 and the sample occupying the space *z*>0. Then the equations can be solved to

$$P = P(0)e^{-\frac{z}{\delta}}|_{z\to 0^+} \quad (2.19)$$

For $\delta > 0$ the polarization at the surface is reduced in comparison to the bulk value. When $\delta < 0$ the polarization and also the phase transition temperature are enhanced [33, 45].
In thin films again the coupling between polarization and strain has to be regarded. It can be distinguished between a homogeneous strain due to the substrate-film lattice mismatch and an inhomogeneous starin due to lattice defects or compositional and thermal gradients. The homogeneous strain shifts the transition temperature and the spontaneous polarization, so room-temperature ferroelectricity has been observed in $SrTiO_3$ thin films thus the bulk is paraelectric at this temperature [46] and for $BaTiO_3$ the spontaneous polarization has been doubled in comparison to the bulk value [47]. Even new stable "epitaxial phases" that would not be stable

in the bulk are indicated by temperature-misfit strain phase diagrams from theoretical studies. [48–50].
For the investigation of epitaxially strained ferroelectrics the films are grown on thick substrates and the ferroelectric is approached as a bulk material with homogeneous elastic terms constrained to match the substrate lattice conditions. Therefore the film thickness d has to be lower than the critical thickness d_c above which inelastic defects appear. The in-plane strains are constant throughout the film thickness and the associated stresses are finite but not fixed and

$$\sigma_3 = \sigma_4 = \sigma_5 = 0 \tag{2.20}$$

For the case of a (001) ferroelectric film grown on a cubic substrate

$$\eta_1 = \eta_2 = \frac{a - a_o}{a} \tag{2.21}$$

where a and a_0 are the constrained and free lattice constants of the film. For this system the elastic free energy can not be used to find the equilibrium properties, but a Legendre transformation to a modified thermodynamic potential must be used

$$\mathcal{F}' = \mathcal{F} + \eta_1\sigma_1 + \eta_2\sigma_2 + \eta_6\sigma_6 \tag{2.22}$$

For a uniaxial ferroelectric with a polarization in the z direction the free energy with the given conditions can be written

$$\mathcal{F} = \mathcal{F}_\mathcal{P} - \frac{1}{2}s_{11}(\sigma_1^2 + \sigma_2^2) - Q_{12}(\sigma_1 + \sigma_2)P^2 - s_{12}\sigma_1\sigma_2 - \frac{1}{2}s_{44}\sigma_6^2 \tag{2.23}$$

where Q_{ij} and s_{ij} are the electrostrictive constants and the elastic compliances. With $\frac{\partial\mathcal{F}}{\partial\sigma_i} = -\eta_i$ and solving for $\sigma_1 = \sigma_2 = \sigma$ and $\sigma_6 = 0$ we find that

$$\mathcal{F}' = \frac{\eta^2}{s_{11} + s_{12}} + \frac{1}{2}(a - \frac{4\eta Q_{12}}{s_{11} + s_{12}})P^2 + \frac{1}{4}(b + \frac{4Q_{12}^2}{s_{11} + s_{12}})P^4 + \frac{1}{6}cP^6 \tag{2.24}$$

where both the quadratic and the quartic polarization terms are renormalized, leading to a shift of the transition temperature from the bulk value

$$T' = T_0 + \frac{4\eta Q_{12}}{a(s_{11} + s_{12})} \tag{2.25}$$

and the spontaneous polarization. The sign of these shifts will be determined by the relative signs and magnitudes of Q_{12} , s_{11} and s_{12} . These shifts and the change in the order of the

phase transition as well as new phases are also calculated by [51].
The inhomogeneous strain is due to a thermal or strain gradient or to lattice defects in the material and leads again to an additional term in the free energy of the system. For example let us take a film with a thickness above the critical thickness d_c and the same configuration as discussed before. Then the contribution of the strain gradient is given by [33]

$$\Delta_{SG} = \gamma \frac{d\eta(z)}{dz} \tag{2.26}$$

The contribution for lattice defects is discussed by [52]. Therefore again a renormalization of the coefficients *a* and *b* is necessary, leading to generalization of the theory.

2.3 Size effects

The previously described changes in the polarization and phase transition temperature including the smearing of the paraelectric-ferroelectric phase transition are only a few of the changes of the material properties due to the change of the geometrical dimensions. Other changes are the increase of the coercive field E_C, the decrease of the dielectric permittivity ε_r, the decreasing piezoelectric constants d_{ijk} and the change in the domain structure. All these parameters are crucial to the different applications due to the wish of a size reduction to as small structures as possible but still remaining useful parameters. Even a complete loss of ferroelectricity below a critical size may be encountered.
One of the most relevant parameters changing significantly as the sample thickness is reduced is the coercive field. Intuitively the switching voltage should linearly depend on the thickness while the coercive field stays constant. But in 1962 H. Kay and J. Dunn introduced a semi-empirical law [53] where they showed a thickness dependence of the coercive field of

$$E_c(d) \propto d^{\frac{2}{3}} \tag{2.27}$$

where *d* is the thickness of the investigated Triglycine Sulphate crystals for a thickness between 0.15 mm and 4 mm. Ever since it has been used successfully to describe the thickness dependence of the coercive field in the range of 100 μm to 1 nm film thicknesses [54].
A new approach based on inhomogeneous nucleation has recently been developed by Chandra et al. [56]. In ultrathin polyvindylin films a deviation from this law was observed for the thinnest films below 15 nm [57]. Dawber et al. [58] showed that the scaling law however holds over six decades of thickness down to 1 nm as illustrated in Fig. 2.4 taking into account the effects of a finite depolarization field due to the incomplete screening in the electrode. Also

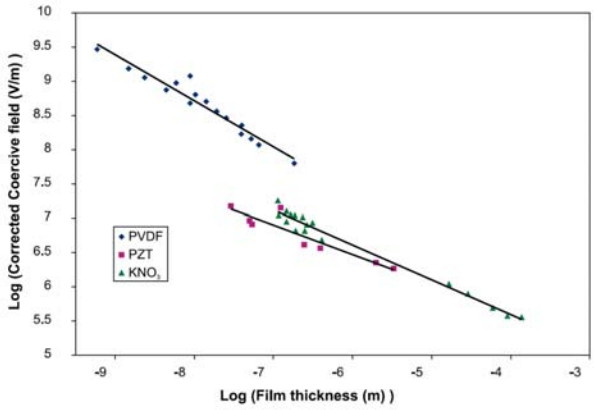

FIGURE 2.4: Coercive field in dependence of the film thickness for different materials [55].

Pertsev et al. [59] measured coercive fields in very thin $PbZr_{0.52}Ti_{0.48}O_3$ films with a good agreement to the scaling law based on a different model.
The decrease of the dielectric permittivity as well as the decrease of the piezoelectric constants is shown for a reduction of the thickness of $PbZr_{0.52}Ti_{0.48}O_3$ films by Lian et al. [60]. While the dielectric permittivity is reduced about 70% for a film thickness of 2 μm to 0.5 μm the dielectric constant d_{33} is decreased to one third of its initial value. Similar investigations showing a decrease of ε_r are presented by Basceri et al. [61] for (Ba,Sr)TiO_3 thin films.
The change in the domain structure can be separated in two different parts. First the change from a different orientation of the domains to a single orientation structure for a reduction of the size. Li et al. [62] reported on x-ray studies on $PbTiO_3$ grown by metal organic vapor deposition. Films thicker than 150 nm showed a mixed *a*- and *c*-axis orientation whereas films below 150 nm showed only *c*-axis orientation. Theis et al. [63] showed the same behavior for pulsed laser deposited $PbTiO_3$ thin films with a change in the orientation structure at 40 nm. These different thicknesses can be explained by other experimental observations. Speck et al. [64] developed a domain stability map with the correlation of the domain formation in thin films and the cooling rate.
Up to now all size reduction is discussed one dimensional, in the thickness of thin films. But as in this work also nanoislands are investigated the reduction of the lateral size is of great interest. To study the domain configuration in differently shaped and dimensioned structures the groups of Gregg and Scott used a focused Ion Beam Microscope (FIB) to cut thin film sheets and nanowires directly from bulk single crystal $BaTiO_3$. The domain characteristics of thin sheets and nanowires are characterized as a function of scale and of morphology [65]. The domain periodicity shows a strong dependence on the size and shape of the structure. The situation is

sketched in Fig. 2.5. The sheet is oriented parallel to the *z*-direction and perpendicular to the *x,y*-direction. In this configuration the surface charges occur only along the *y*-direction. Only along this axis the configuration is sensitive to a reduction of the thickness. The size dependence follows Kittels law $w \propto \sqrt{d}$ [66] where *w* is the domain width and *d* the thickness along the direction.

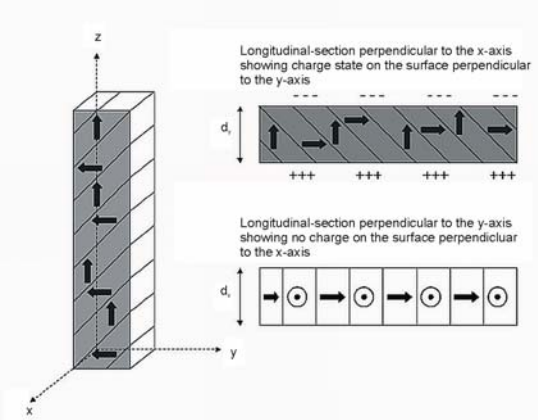

FIGURE 2.5: Schematic of the domain configurations in the ferroelectric columns. Longitudinal sections illustrate the different expected surface charge states on the free surfaces of the columns [65].

Along the other direction no change due to the reduction in size in the range of investigation occurs.

2.4 Soft modes

Polarity of ferroelectrics can be investigated and proven in many ways, two of which are pursued in this work. First by monitoring the third-rank piezoelectric tensor with a piezoresponse force microscope (PFM) and second by the detection of the soft modes with Raman spectroscopy. By the use of tip-enhanced Raman spectroscopy a lateral resolution of a few tens of nanometers is possible, in the same order of magnitude as with the PFM setup. In this chapter the theory of the soft modes is introduced. A more detailed description can be found in [67]. An introduction of Raman spectroscopy of soft modes will be given in section 5.2.
The first soft mode in a structural phase transition was observed by Raman and Nedungadi in 1940 at the $\alpha - \beta$ transition in quartz [68]. This transition is accompanied by a decrease in the frequency of a totally symmetric optical phonon as T_C is approached from below. In 1959 Cochran and Anderson suggested the now well established theory that the phase transition in certain ferroelectrics might result from an instability of one of the normal vibrational modes

of the lattice [69]. In this theory the frequency of the relevant soft phonon decreases on approaching the critical temperature T_C and the restoring force for the mode displacements tends to zero until the phonon has condensed out at the stability limit. The static atomic displacement taking place from the paraelectric to the ferroelectric phase thus represents the frozen-in mode displacements of the unstable phonon. The eigenvector of the unstable phonon is the order parameter of this transition.
One of the Kramers-Kronig relations gives the dependence of the quasi-static dielectric response on the dynamic properties of the system

$$\varepsilon(0,0,T) - \varepsilon(\infty) = \frac{2}{\pi}\int_0^\infty \frac{\varepsilon''(\omega',0,T)}{\omega'} d\omega' \tag{2.28}$$

where $\varepsilon'(\omega,\vec{q},T)$ is the real and $\varepsilon''(\omega,\vec{q},T)$ the imaginary part of the dynamic wave vector $\vec{q}$ dependent constant $\varepsilon(\omega,\vec{q},T)$ and $\varepsilon(\infty)$ the value of the dielectric constant for frequencies much higher than the ferroelectric dispersion frequency. The normal modes of the system are given as the poles of $\varepsilon(\omega,\vec{q},T)$

$$\frac{1}{\varepsilon(\tilde{\omega})} = 0 \tag{2.29}$$

The pole $\tilde{\omega}_i$ which is critically dependent on temperature, represents the soft mode. For ferroelectrics the static dielectric constant follows the Curie-Weiss law

$$\varepsilon(0,0,T) = \frac{C}{T - T_0} \tag{2.30}$$

so that $\frac{1}{\varepsilon(0)} = 0$ at T=T_0 leading to a vanishing complex frequency $\tilde{\omega}$ of the soft mode at the stability limit. On the other hand at $T \neq T_0$ $\tilde{\omega}_i \neq 0$ implies the existence of a soft mode.
The soft modes may have a resonant character where $|\omega'| \gg |\omega''|$ or a relaxational, Debye-like character with $|\omega'| \ll |\omega''|$. For a ferroelectric with a single infrared active mode and no damping we can derive the Lyddane-Sachs-Teller (LST) relation from equation 2.28 as:

$$\frac{\varepsilon(0)}{\varepsilon(\infty)} = \frac{\omega_L'^2}{\omega_T'^2} \tag{2.31}$$

where ω_L' is the zero and ω_T' the pole of the dielectric function $\varepsilon(\omega)$. For a cubic diatomic paraelectric crystal, ω_L' is the longitudinal optical phonon frequency, which is experimentally verified to be temperature independent, at the center of the Brillouin zone and ω_T' the corresponding transverse optical phonon frequency. The soft mode behavior of the infrared active

transverse optical phonon is then predicted by the LST relation and the Curie-Weiss law for the dielectric constant to

$$\omega_T'^2 = a(T - T_0) \tag{2.32}$$

For a pure relaxational ferroelectric ($\omega' = 0$, $\omega'' \neq 0$)

$$\varepsilon(\omega) = \varepsilon(\infty) + \frac{\varepsilon(o) - \varepsilon(\infty)}{1 + i\omega\tau} \qquad \text{with} \qquad \tau = \frac{1}{\omega_p''} \tag{2.33}$$

only one pole *(ω_p'')* and one zero *(ω_L'')* of the dielectric function exists and both are imaginary. The LST relation is then linear in the frequencies.

$$\frac{\varepsilon(0)}{\varepsilon(\infty)} = \frac{\omega_p''}{\omega_L''} \tag{2.34}$$

With the Curie-Weiss law of the dielectric function and the temperature independence of ω_L'' the critical slowing down of the Debye relaxation time τ can be written

$$\tau = \frac{1}{\omega_p''} \propto \frac{1}{T - T_0} \tag{2.35}$$

In contrast to the relaxational soft mode system, where the critical slowing-down takes place in the relaxation time, it shows up directly in the frequency of the soft mode in the resonance type, which can be explained by considering the equation of motion of the polarization

$$c_q \ddot{P}_q + b_q \dot{P}_q + a_q P_q = 0 \tag{2.36}$$

which can be derived from the phenomenological treatment of irreversible thermodynamics [70].
For a pure relaxation system the kinetic energy term is absent (*c_q=0*) and equation 2.36 becomes a diffusion equation so that

$$P_q(t) = P_q(0) e^{-t/\tau_q} \qquad \text{with} \qquad \tau_q^{-1} = \frac{a_q}{b_q} \tag{2.37}$$

It can be shown that a_q is proportional to the inverse wavelength-dependent static dielectric susceptibility which for a characteristic value of *q* diverges at the stability limit. Thus we get for the critical *q* value

$$a_{q_0} \propto (T - T_0) \qquad \text{and} \qquad \tau_{q_0}^{-1} \propto (T - T_0) \to 0 \tag{2.38}$$

as $T \rightarrow T_0$. The relaxation near the critical point is very slow due to the divergence of the susceptibility.
For a resonance type $b_q \neq 0$ and with

$$P_q(t) = P_q(0)e^{-\alpha_q t} \tag{2.39}$$

we find from equation 2.36 the complex soft mode frequency α_q as

$$\alpha_q = \frac{-b_q \pm i\sqrt{4a_q c_q - b_q^2}}{2c_q} \tag{2.40}$$

For a small damping, $b_q \ll 4a_q c_q$ it can be written as

$$\alpha_q = -\frac{b_q}{2c_q} \pm i\sqrt{\frac{a_q}{c_q}} \tag{2.41}$$

with $-\frac{b_q}{2c_q} = \omega_q''$ the imaginary part and $\sqrt{\frac{a_q}{c_q}} = \omega_q'$ the real part of the complex frequency of the polarization mode. Thus c_q is temperature-independent, the critical slowing-down appears here in the real part of the frequency

$$\omega_{q0}' \propto (T - T_0)^{\frac{1}{2}} \tag{2.42}$$

whereas the imaginary part is temperature-independent.
However, close to T_0 the damping increases and the complex soft mode frequency α_q approaches zero.
As examples for the different types of the systems $BaTiO_3$ has a resonant nature of the soft modes and $NaNO_2$ a relaxational character.
Raman spectroscopy provides a quantitative handle on the polar properties of the sample as the energy of the soft mode is proportional to the proximity of the ferroelectric phase transition. This phase transition can either be temperature- or size-driven and Ishikawa et al. [71] showed the feasibility of this technique for lead titanate nanoparticles. They extrapolated the critical size to be 12.6 nm at room temperature. However, these experiments were conducted on an ensemble of nanoparticles that are strongly electrostatically coupled. The investigation of individual ferroelectric nanoislands has not been achieved so far due to the small cross-section of Raman scattering. Tip-enhanced Raman spectroscopy opens a way to obtain both lateral resolution and sufficient field enhancement to image and investigate individual ferroelectric nanoislands for the first time.

2.5 Electromechanics

2.5.1 Piezoelectric effect

As described in section 2.1 every ferroelectric is also piezoelectric. Piezoelectric materials can be polarized by applying a mechanical stress or an electric field. In the first case, the so called piezoelectric effect, the correlation between the mechanical stress σ_{jk} and the resulting surface charge density D_i is given by the piezoelectric tensor d_{ijk}:

$$D_i = d_{ijk}\sigma_{jk} \tag{2.43}$$

d_{ijk} [CN^{-1}] is a third rank tensor. In the second case, the converse piezoelectric effect, the induced strain η_{ij} caused by an electric field E_k is:

$$\eta_{ij} = d_{kij}E_k \tag{2.44}$$

where d_{kij} [mV^{-1}] are the converse piezoelectric coefficients represented by a third-rank tensor. Thermodynamic considerations show that the direct and the converse piezoelectric coefficients are the same [72]. Because both, the stress tensor σ_{jk} and the strain tensor η_{ij} are symmetrical, the piezoelectric tensor is symmetrical with respect to the corresponding indices d_{ijk}=d_{ikj}. Due to this symmetry a maximum of 18 of the 27 tensor elements of this tensor are independent. Thus the piezoelectric effect can be described in the Voigt-notation by a 6x3 matrix. In this notation (D_i=$\sigma_{ij}E_j$ with $i \in \{1,2,3\}$ and $j \in \{1,2,...,6\}$) only two indices are needed. The first is retained and the last two are substituted as follows:

tensor notation	11	22	33	23,32	13,31	12,21
Voigt notation	1	2	3	4	5	6

Due to the crystal symmetry the number of independent piezoelectric constants can be further reduced (Neumann‘s principle). In this work only tetragonal materials are investigated. Only five piezoelectric coefficients remain non-zero within them

$$d_{33}\ ,\ d_{31} = d_{32} \text{ and } d_{15} = d_{24}$$

leading to only three independent piezoelectric coefficients.
The piezoelectric hysteresis, here for example for the d_{33} parallel to the direction of the applied field is shown in Fig. 2.6*a)*. The curve shows a similar behavior as the polarization curve in Fig. 2.2. The only difference is that d_{33} stays constant if the parallel field is enhanced.

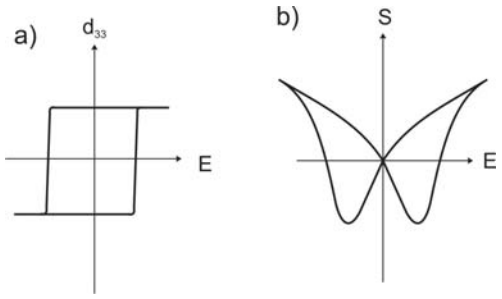

FIGURE 2.6: Schematic of the converse piezoelectric effect: hysteresis loop of the piezoelectric coefficient vs. field (a) and butterfly loop of strain in dependence of the applied field (b), [29].

Inversion of the piezoelectric tensor by an external electric field leads to a strain-electric field hysteresis (see Fig. 2.6*b)*. Without an applied field the strain is zero but upon an increase of the applied field the crystal starts to expand. When the field is decreased but still parallel, the strain is reduced in the same way becoming zero again when the field is zero. For a reversed direction of the applied field, the crystal starts to contract leading to a change in the sign of the strain until the coercive field is reached and the polarization is switched to be parallel again. Therefore the crystal suddenly expands and the strain becomes positive again. For an increasing or decreasing field in this direction now the strain is also increasing or decreasing respectively, becoming zero again for a zero applied field. If then the field is again increased antiparallel to the spontaneous polarization the crystal will contract again until the coercive field is reached. Eventually the polarization is switched and the butterfly-loop of the strain vs. applied field is closed.
Theoretically for a mono-domain crystal the strain field dependence should be linear except for the switching points. But as shown in Fig. 2.6*b)* the real situation is more complicated due to a multi-domain configuration in the materials including non-180^o domains.

2.5.2 Electrostriction

The electromechanical response of matter also comprises higher order terms leading to a non-linear coupling between the mechanical strain and the electric field which can be described by a Taylor expansion of the strain in the applied field:

$$\eta_{ij} = \underbrace{d_{kij}E_k}_{piezoelectric\ effect} + \underbrace{Q_{ijkl}E_kE_l}_{electrostriction} + ... \tag{2.45}$$

where Q_{ijkl} are the electrostrictive coefficients, elements of a fourth-rank tensor. The electrostriction describes the change in length of a dielectric material in dependence of the quadratic

applied field [73]. Since the electrostriction is quadratic in the electric field it is not depending on the polarity of the applied. Being represented by a fourth-rank tensor, electrostriction is omnipresent and not restricted by crystal symmetry.

2.6 Materials

Subsequent to the phenomenology of ferroelectricity, the microscopic origin of the polarization in the used materials is briefly discussed. All materials in this work have the general formula ABO_3 and a perovskite structure. Above the phase transition temperature they have a cubic centrosymmetric phase with the same lattice constant a_c for every direction shown in Fig. 2.7*a)*. The A^{2+} cations are located on the corners and the B^{4+} cations in the center of the cubic unit cell. The oxygen anions are situated on the face centers building an octahedron. In the ferroelectric phase the unit cell becomes tetragonally distorted. The B^{4+} ion is moved out of the center either to a lower or upper position. The oxygen ions in the plane perpendicular to this movement are also displaced but in the opposite direction therefore enhancing the separation of the center of the positive and negative charges, see Fig. 2.7*b)*. The two possible positions of the B^{4+} ion are thermodynamic ground states.

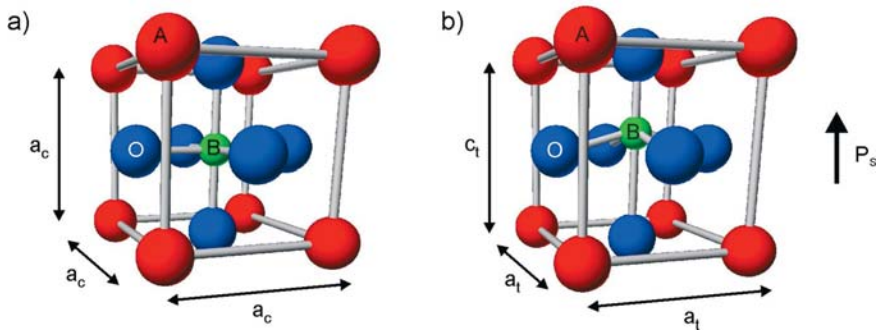

FIGURE 2.7: The unit cell of an ABO_3 type material with perovskite structure showing the positions of the ions in a) the cubic an b) the tetragonal phase. The B^{4+} ion can occupy two different positions, the upper (shown here) and a lower position that comes along with a displacement of the oxygen ions in the opposite direction [10, 29]

In the following subsections the data of the materials in the ferroelectric phase are presented. All given values are valid for room temperature because all experiments are done at this temperature and cited from [74].

2.6.1 Barium titanate

Barium titanate ($BaTiO_3$) is mechanically and chemically stable and is of great interest as it is a lead free ferroelectric. It is ferroelectric at room temperature and even above up, to a temperature of $T_c = 130^{\circ}$C and has a room temperature tetragonal structure with the lattice constants $a = 0.39920$ nm and $c = 0.40361$ nm, resulting in a tetragonality of 1.1%. The values for the piezoelectric coefficients are $d_{33} = 85.6$ pm/V, $d_{31} = -34.5$ pm/V and $d_{15} = 392$ pm/V.

2.6.2 Lead Zirconate Titanate

Lead zirconate titanate ($PbZr_xTi_{1-x}O_3$) is a solid solution of antiferroelectric lead zirconate ($PbZrO_3$) and $PbTiO_3$. Depending on the ratio between $PbTiO_3$ and $PbZrO_3$ the phase transition temperature, the lattice parameters, the crystal structure and the electronic properties of $PbZr_xTi_{1-x}O_3$ can be modified. A phase diagram and the lattice constants as a function of the Zr content are shown in Fig. 2.8. The Curie temperature of $PbTiO_3$ is among the highest in

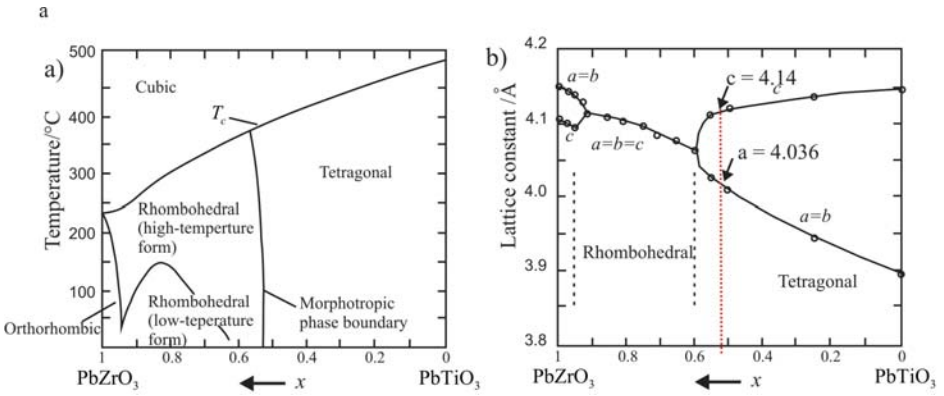

FIGURE 2.8: a) Phase diagram and b) lattice constants of $PbZr_xTi_{1-x}O_3$ in dependence of the $PbZrO_3$ content with the red dotted line marking the composition used in this work , adapted from [29].

perovskite-type ferroelectrics [29] and an increasing $PbZrO_3$ content decreases the phase transition temperature. A morphotropic phase boundary divides the ferroelectric phases into a Ti-rich tetragonal phase region and a Zr-rich rhombohedral phase region, located at room temperature at a Zr-content of 52%, see Fig. 2.8*a)*. At this morphotropic phase boundary the dielectric and piezoelectric constants and the piezoelectric coupling factors exhibit anomalously high values and therefore this composition is especially promissing for piezoelectric applications [10]. Figure 2.8*b)* illustrates the abrupt change of the lattice parameters near this boundary.
In this work $PbZr_{0.48}Ti_{0.52}O_3$ is used with lattice constants $a = 0.4036$ nm and $c = 0.414$ nm

[75]. The piezoelectric tensor elements are $d_{31} = 97.5$ pm/V, $d_{33} = 223$ pm/V and $d_{15} = 494$ pm/V[3].

2.6.3 Sodium Niobate powders

Lead free piezoelectrics are of tremendous interest for applications. Beside $BaTiO_3$ ceramics like (K,Na)NbO_3 modified by Li-substitutions on the A-site and Ta- and Sb-substitutions on the B site are of particular interest. The piezoelectric constant along the tetragonal axis of this material is $d_{33} = 416$ pm/V [76] but it is known to have a rather poor sinterability. Therefore sodium niobate $NaNbO_3$ is investigated as powder. In the bulk structure this material has an orthorhombic *Pbcm* crystal structure and is antiferroelectric [77]. For small particles with a diameter below 400 nm it becomes non-centrosymmetric and changes its structure to an orthorhombic *Pmc2*$_1$ space group with the lattice constants $a = 0.776778$ nm, $b = 0.551759$ nm and $c = 0.556829$ nm. When the grain size is decreased even further (below 70 nm) it becomes centrosymmetric in a *Pmma* structure again.

[3]Samples are courtesy of Marin Alexe at the Max-Planck Institute of Microphysics, Halle.

3 Sample Preparation

The samples used in this work are fabricated by different methods. The thin films and nanoislands are either prepared by pulsed laser deposition (PLD) or by chemical solution deposition (CSD). This chapter introduces these methods and gives a short overview of the production parameters. Furthermore the fabrication of investigated ferroelectric hollow particles and ceramics is introduced.

3.1 Pulsed Laser Deposition

Pulsed laser deposition (PLD) is used for the fabrication of thin films and nanoislands of various materials. The concept is shown in Fig. 3.1. Inside an ultrahigh vacuum-chamber a solid

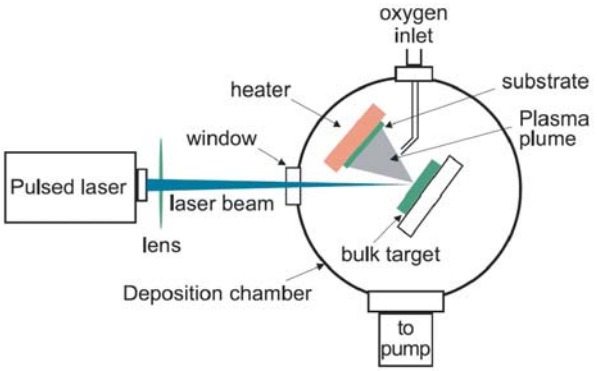

FIGURE 3.1: Sketch of the pulsed laser deposition setup [78]

(typically ceramic, single crystal or metal) target is exposed to short high-energy laser pulses, which ablate some material via vaporization or at higher energies via ionization of the target atoms so that a plasma is formed [10]. The laser beam is incident at an angle of 45° to the target surface. The substrate on which the material is to be grown is placed opposite to the target. Ideally the laser has a short wavelength in the ultraviolet spectral region for a maximum absorption as the materials of interest are wide band-gap semiconductors. Therefore excimer lasers like krypton flourine (KrF) or argon flourine (ArF) with wavelengths of 248 nm or 193 nm are used. This corresponds to photon energies of 5 eV and 6.4 eV (typical band-gaps are between 3.5 eV and 4 eV).

Intense laser pulses with a rise time of only a few nanoseconds heat a small volume at the surface of the target. There the plasma is formed and all elements of the target evaporate simultaneously. So the stoichiometry of the target is directly transferred to the film and the

problem of controlling the needed ratios of several elements can be solved by preparing a target with the desired composition. The advantage of the use of a solid target with the desired film stoichiometry and the big variety of possible materials makes PLD also a convenient tool for depositing complex materials and for the fabrication of heterostructures and devices. [33]. For the growth of epitaxial thin films suitable substrates and the main five deposition parameters, target-substrate distance, partial pressure of oxygen, substrate temperature, laser pulse energy density and pulse repetition rate have to be chosen appropriately. For the sample used in this work a $SrRuO_3$ bottom electrode is grown on a $SrTiO_3$ (001) single crystal substrate from Crystech. The oxygen partial pressure is 0.25 mbar. Subsequently the $BaTiO_3$ is grown on the bottom electrode with a oxygen partial pressure of 1 mbar. For both depositions a substrate temperature of 700°C and the KrF laser with 16 ns pulses at 10 Hz with an energy density of 5 J/cm^{-2} is used. For a epitaxial growth the lattice parameters and the thermal expansion coefficients have to be compatible. The lateral unit cell parameters for the three materials are [79] [74]:

$SrTiO_3$: $a = 0.3905$ nm
$SrRuO_3$: $a = 0.3930$ nm
$BaTiO_3$: $a = 0.3992$ nm

In the layered $SrTiO_3$/$SrRuO_3$/$BaTiO_3$ structure, the strontium titanate substrate stresses the strontium ruthenate compressively. As a result the *a* axis of the barium titanate unit cell fits better onto the strontium ruthenate bottom electrode than its *c* axis ($c = 0.4036$ nm). This leads to the assumption that the barium titanate nanoislands are grown (001) orientated. The piezoresponse force microscopy results indeed provide evidence for *c*-axis oriented grains.

3.2 Chemical Solution Deposition

Chemical solution deposition (CSD) is commonly used for the fabrication of polycrystalline perovskite-type oxide thin films. For this work $PbZr_xTi_{1-x}O_3$ nanoislands are fabricated with this method. The start of every chemical solution deposition process is the preparation of a suitable precursor that contains the required components mixed in a stoichiometric ratio needed for the favored final film composition, dissolved in appropriate solvents. Sometimes compositional corrections with respect to the exact perovskite stoichiometry or the addition of additives like chemical stabilizers are required. Next the coating solution needs to be deposited on the substrate. For the samples used in this work, this is done by spin coating on a rotating substrate. Subsequently the as-deposited film is dried, pyrolyzed, crystallized and optionally post-annealed [80]. The desired film thickness can either be achieved by concentration changes

or by multiple coatings and annealing if necessary.
The $PbZr_{0.52}Ti_{0.48}O_3$ samples are prepared from a commercial precursor [81]. The precursor is diluted 1:10 with butanol. As substrate a cubic single crystalline $SrTiO_3$ (001) with a niobium concentration of 0.5% weight is used which also acts as bottom electrode [82]. The precursor is spin coated on the substrate with a spinning speed of 6000 rpm. The obtained gel film is dried on a hot plate at 80°C for 5 min, pyrolized at 300°C for 5 min and finally crystallized at 800°C for 1 h in a lead oxide atmosphere. During the high temperature treatment, the ultra-thin film breaks up into nanoislands of 20-60 nm lateral size. Epitaxial relationship between substrate and top structures are shown by x-ray diffraction and high-resolution transmission electron microscopy confirms single crystal structure [83]. Unpublished data of Nano-XPS measurements of lead titanate nanoislands also grown under a lead oxide atmosphere on the same substrate show a uniform coverage of the whole surface with lead oxide [84].

3.3 Fabrication of barium titanate hollow particles

Hollow $BaTiO_3$ particles are fabricated with a two-step method. First $BaCO_3$ crystals are coated with a shell of amorphous titania by suspending a barium carbonate powder in an aqueous solution of peroxotitanium with a molar ratio of Ba/Ti of 1, slowly heating the suspension up to 95°C and keeping the temperature constant for 5 h. Since there is no appreciable loss of either barium or titanium during the coating process, the final coated particles have the same stoichiometry as the suspension [85]. The resulting $BaCO@TiO_2$ core-shell particles are then converted in $BaTiO_3$ hollow particles by firing in air in a muffle furnace at 700°C with a heating rate of 5°C/min and a duration of the isothermal treatment of 24 h. Formation of the cavity occurs due to the much faster out-diffusion of the core phase than the in-diffusion of the shell material. Initially, the strong unbalance of the diffusion fluxes determines the formation of Kirkendall porosity close to the original $BaCO_3/TiO_2$ interface. Later, the surface diffusion of the carbonate leads to a pore growth and coalescence with the formation of a single cavity [86]. For the piezoresponse force microscopy experiments, the hollow particles were embedded in a conductive resin, one sample in copper and the other in graphite.

3.4 Synthesis of submicron $NaNbO_3$ powders

Stoichiometric $NaNbO_3$ powders are prepared through microemulsion mediated by hydrolysis of the appropriate mixtures of sodium ethoxide ($NaOH_5C_2$) and niobium ethoxide ($Nb[OH_5C_2]_5$) as precursor solutions. All synthetic procedures are performed with the Schlenk-technique due to the moisture sensitivity of the precursors [76]. Niobium ethoxide is obtained from $NbCl_5$

(Alfa Aesar) dissolved in toluene (Merck, analytical grade) by the addition of ethanol and ammonia (Linde), filtering off ammonium chloride, and subsequent vacuum distillation (158°C, 0.1 mbar). After the preparation of the precursor solutions, a stoichiometric amount of the microemulsion is added in order to form the nanosized powders. Raw powders are annealed in air for 1 h at various temperatures between 200 and 1000 °C. After cooling to room temperature, a part of all these powders is heat-treated for 12 h at the same temperatures in air again [87].
For the piezoresponse force microscopy, first micron and submicron powders are dispersed and fixed in epoxy resin and then polished to realize powder exposures on the surface of the powder-epoxy composites.

The embedding of hollow nanoparticles and nanopowders into conductive resins is necessary for two reasons: PFM is a contact-mode microscopy that moves free particles over the surface unless they are immobilized and very uneven surfaces create topography artifacts in PFM images.

4 Electromechanical Force Microscopy

The structure of this chapter corresponds to the description of optical experiments, following the optical beam from the source to the detection system. For scanning probe experiments such as piezoresponse force microscopy the analogy is given by an electrical stimulus travelling to the tip-sample interface and returning a mechanical response that is again transformed into an electrical signal by means of the optical lever method. The fundamental concept of this method has been shown and confirmed by various groups over the last decade with different emphasis on imaging, lithography or quantitative studies. The present work addresses several crucial points of this method like the measured phase difference between antiparallel domains, the influence of vertical switching on the lateral signal in c-axis oriented materials, the amplitude of the applied field and the restriction to piezoelectric materials that go beyond the conventional interpretation of the method and that pave the way to novel detection schemes and enhanced resolution.
Every electromechanical force microscopy image or experiment starts with a signal from the lock-in amplifier that has an arbitrary electric field amplitude E_0, a frequency ω and a phase φ which can be considered as zero at the source.

$$E(t) = E_0 \cos(\omega t + \varphi) \tag{4.1}$$

The signal of the piezoelectric response already contains two channels, one for the vertical displacement of the cantilever, another one for the lateral displacement. They are also identified by an amplitude, a frequency and a phase. So how does the excitation voltage translate into the displacement of the cantilever, and how does the displacement of the cantilever translate into the signals at the photodiode that are then passed on to the two lock-in amplifier used for detection? What can we learn from the amplitude, from the frequency and from the phase? What does it mean if the detected phase difference between antiparallel ferroelectric domains is not exactly π as predicted by theory? Which influence on the phase difference is given by the adsorbates especially when they are not only regarded as a part of a DC but as given by the experiment as a part of an AC circuit?
The frequency of the experiment plays a central role as it is the reference signal for the lock-in amplifier and does not change in the course of the experiment. A couple of general requirements should be fulfilled for the operating frequency ω: it should not be an integer multiple of the frequency at which standard AC components are operated, typically 50 or 60 Hz and it should not coincide with cantilever resonances as this might blur the phase information that jumps upon resonances. Some microscopes suffer considerably from mechanical loops [88] that should also be avoided as well as acoustic resonances. The last constraint is the contact

mode resonance that should not be exceeded and that can be determined for a clamped cantilever to be about $4 \cdot f_0$ [89]. The used contact mode cantilevers are typically specified to resonate at about 13 kHz which leaves enough frequency range up to 50 kHz to work without undesired resonances. The amplitude of the applied field should be below the coercive field to be able to detect the orientation of the polarization. But what happens if the coercive field is exceeded and switching occurs upon scanning? Is the polarization reversal still detectable and how can it be measured than?

This chapter starts with measurements on novel material systems as examples for the possibilities PFM offers for the investigation of ferroelectricity. The measurements show locally resolved impurities on well known materials as well as hints for ferroelectricity in the novel material systems which where investigated by piezoelectric response microscopy for the first time. Subsequently the restrictions or limitations due to the topography and the adsorbates on the applied voltage are discussed especially for very thin films. In chapter 4.3 the adsorbates are regarded in addition to further investigations as an not longer a part of a Dc but as a part of the AC circuit and an additional influence on the phase difference between antiparallel domains becomes obvious.

Applying an electric field above the coercive field volitionally or not leads to some interesting results. Still enabling us to detect whether the material is ferroelectric or not, a new method giving us the possibility to locally determine the coercive field and paving the way for a novel detection scheme is presented. Therefore the chapter 4.5 goes beyond the utilization of the first harmonic for piezoresponse force microscopy but also uses the second harmonic of the electromechanical response. The first realization of electromechanical force measurements at higher harmonics including the second and third harmonic has recently been demonstrated by Harnagea et al. [21] with the focus on the separation of electrostatic and piezoelectric contributions in soft cantilevers that are prone to a strong electrostatic coupling [90]. The present work deals with ferroelectric nanostructures that are tetragonal and typically *c*-axis oriented. Thus the only lateral piezoelectric and electrostrictive response might stem from a local reduction of the symmetry around the AFM-tip causing a lateral torsion of the cantilever. Electrostriction is by no means restricted to materials without a center of inversion symmetry as required for the existence of piezoelectricity. So in principle the in chapter 4.6 presented technique is applicable to monitor local heterogeneities in all materials as long as they exhibit a sufficiently large electrostrictive response, which leads to a huge amount of new possible applications for this technique.

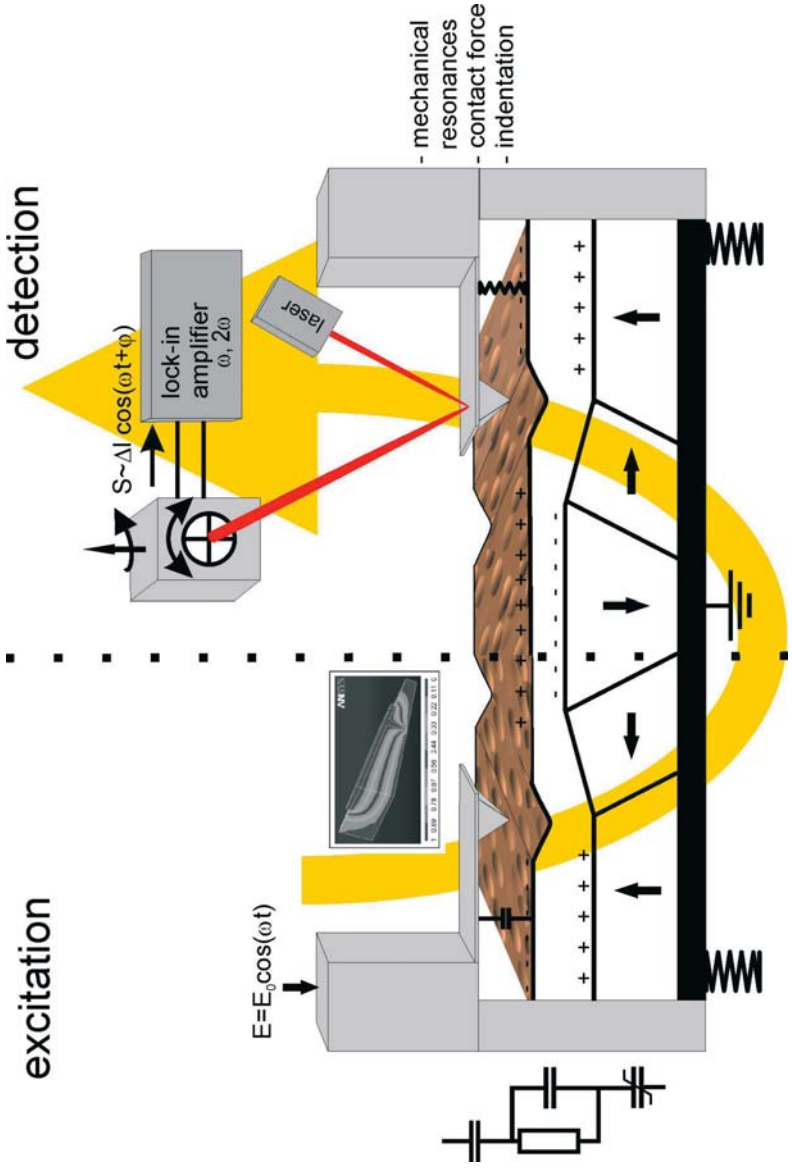

FIGURE 4.1: Sketch of the PFM-setup: The image is divided into two parts: The excitation (left) and detection (right) of the signal. The path of the signal is indicated by the orange arrow in the background starting with the excitation of the tip in the upper left part. At the bottom left the transmission of the electrical signal from the tip to the sample is described. In the lower right part the reversed transfer of the mechanical response of the sample to the tip is shown. Afterwards the signal is translated into a deflection of a laser beam on a photo diode and finally detected by a lock-in amplifier in the upper right part. In the following sections the different contributions will be addressed and explained following this sequence.

4.1 Piezoresponse force microscopy on specific samples

The synthesis of ferroelectric particles and structures with specific arrangements, size and morphology is of particular interest for the exploitation and optimization of already established materials. The investigation of different 1D, 2D and 3D structures with unusual geometries will thus help to develop new devices and to improve the miniaturization of existing devices.

4.1.1 Global non-stoichiometry of $PbZr_{0.52}Ti_{0.48}O_3$ nanoislands locally resolved by PFM

The composition of the sample i.e. the purity of the composition also contributes to the PFM image contrast. Integrating XPS measurements with a lateral resolution of 800 μm provided evidence of different oxidation states of lead. This can be interpreted as a non-stoichiometry of the nanoislands but obviously there is a more conservative interpretation. High resolution transmission electron microscopy images of the PZT nanoislands under investigation showed almost perfect crystallinity except for misfit dislocations as predicted by theory. This is in strong contradiction to individually non-stoichiometric nanoislands. However the growth in a lead oxide atmosphere favors the segregation of PbO_x on top or in between the perovskite nanoislands. We discuss our PFM findings in terms of such a deposition of non-piezoelectric lead oxide on top of the desired structure.
The $PbZr_{0.52}Ti_{0.48}O_3$ sample prepared from the M. Alexe group in the Max-Planck Institut in Halle as described in section 3.2 shows almost perfect crystallinity and epitaxial growth [83]. Piezoresponse force microscopy shows a clear piezoelectric response as can be seen in Fig. 4.1. On these nanostructures also ferroelectric switching was shown [91]. A closer look on the obtained images reveals that in some areas on the sample surface on the ferroelectric or at least piezoelectric nanoislands which show piezoelectric response, smaller structures of a few nanometer exist which do not exhibit any piezoresponse. Figure 4.1 *a)* shows a 500 x 500 nm^2 scan of the topography where the non-piezoelectric regions are marked. The same markers are set exactly at the same positions in the pictures of the vertical piezoresponse amplitude (Fig. 4.1*b)*) and phase (Fig. 4.1*c*). Within the marked areas there is no vertical piezoresponse detectable and the measured phase signal shows only noise in contrast to the other parts of the nanoislands. So the areas with the disappearance of the vertical amplitude and phase of the piezoresponse coincide with the small structures on the nanoislands. These structures are higher than their direct surroundings, which means they are formed after the deposition of the initial material. The structures are most likely lead oxide, which is not piezoelectric, due to the crystallization in lead oxide atmosphere. Independent measurements which show evidence for lead oxide support this assumption [92].

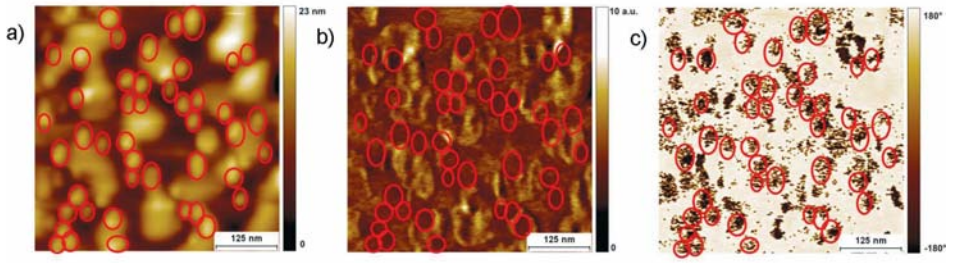

FIGURE 4.1: PFM images of 500 × 500 nm^2 on $PbZr_{0.52}Ti_{0.48}O_3$ nanoislands with the non-piezoelectric regions marked by red circles. Not that these red circles are at the same position in topography (a), vertical amplitude (b) and phase (c).

4.1.2 Ferroelectric hollow particles

One example of novel material structures are hollow crystals and particles. The ferroelectric properties and domain arrangements in this unconventional geometries (see Fig. 4.2) are not well known up to now. In this work these nanoscale ferroelectric properties and the domain

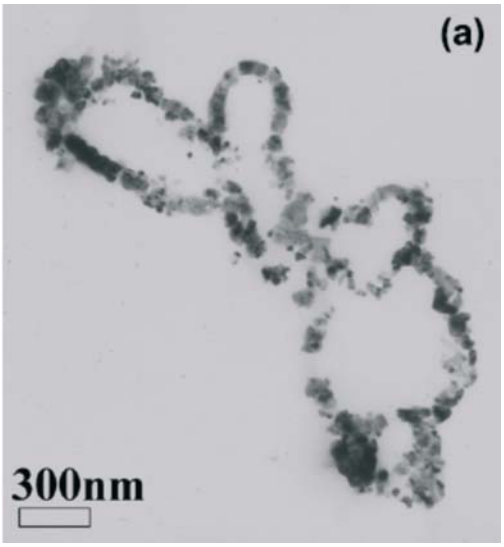

FIGURE 4.2: TEM cross-section of $BaTiO_3$ hollow particles obtained after 24 h calcination at 700°C of the $BaCO_3$@TiO−2 powder. [86].

structure of $BaTiO_3$ hollow particles are investigated by PFM. Therefore the particles were embedded in a conductive resin to enable an electric contact.

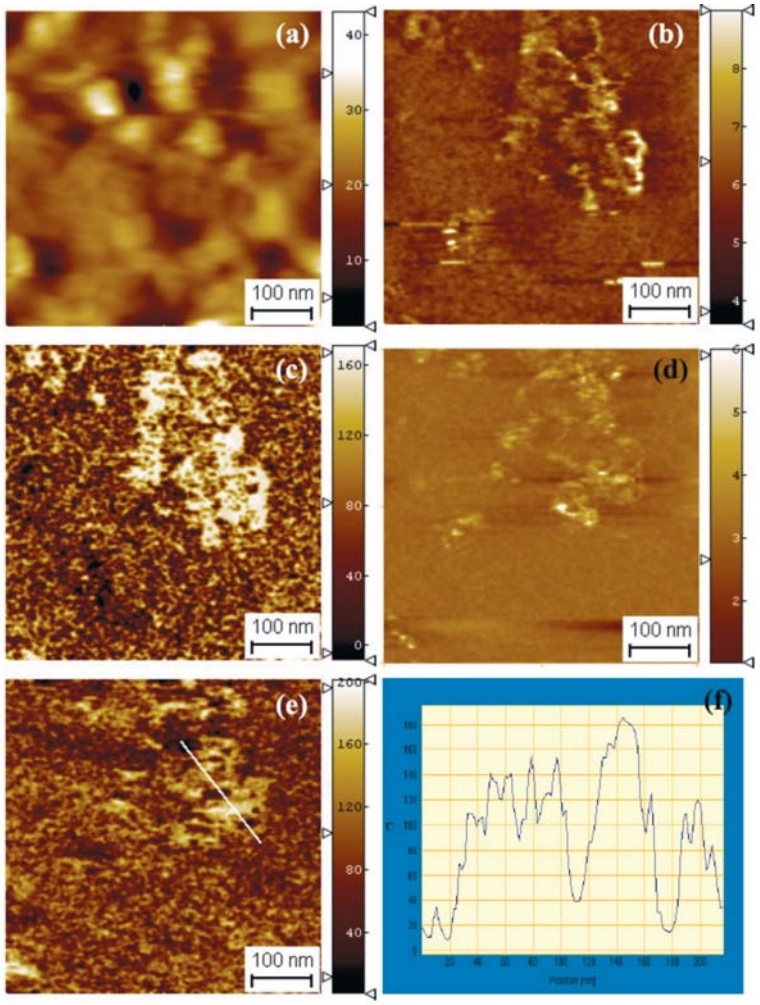

FIGURE 4.3: PFM images of 524×524 nm^2 on embedded $BaTiO_3$ hollow particles: topography (a), note that the preparation procedure did not provide perfectly flat samples, vertical amplitude (b) and corresponding phase image (c) showing an obvious piezoactivity in the planarized structure, lateral piezoresponse amplitude (d) and phase (e) and a line scan (f) providing evidence of 180^o domain walls [86]

The piezoactivity was investigated by applying a voltage of 2 V at 7 kHz to the probe tip. The obtained images for hollow particles after 24 h calcination at 700°C are shown in Fig 4.3. The topography image of Fig. 4.3*a)* shows two sectioned hollow particles. The first one, circular, is next to the center whereas the second one, elongated, is located in the left upper side of the figure. The preparation procedure did not provide perfectly flat samples, causing a negative effect on the image quality. Both in-plane and out-of-plane piezoactivity were detected. The in-plane phase signal (Fig. 4.3*e)*) indicates the existence of ferroelectric domains. A scan along the white line indicated in Fig. 4.3*e)* shows antiparallel polar phases. Small deviations of the 180° phase shift are due to electro-mechanical side-effects. The width of these domains is in the order of the size of the $BaTiO_3$ crystallites (≈50 nm).

Independent X-ray and Raman measurements indicate a tetragonal ferroelectric structure with an axial ratio of $\frac{c}{a} = 1.005$ of the hollow particles. Our findings confirm local ferroelectric functionality and further macroscopic studies will aim at the performance of the entire structure.

4.1.3 Submicron $NaNbO_3$ crystallites

Another promising material for piezoceramics is $NaNbO_3$ due to its ease in preparation in comparison to the $[(K_{0.5},Na_{0.5})_{1-x}Li_x](Nb_{1-y}Ta_y)O_3$ ceramics wich already showed high piezoelectric performance at the morphotropic phase boundary between an orthorhombic and tetragonal modification of this mixed crystal system [93]. At room temperature $NaNbO_3$ is antiferroelectric, but for submicron powders X-ray powder diffraction and Raman measurements showed an up to then unknown noncentrosymmetric crystal structure for this crystallites [94]. The average grain size is evaluated by the use of the line intercept method from the SEM image (see Fig. 4.4) to $0.3 \pm 0.1\,\mu$m.
Here again a preparation of the samples for the PFM-study is necessary. First micron and submicron powders were dispersed, then fixed in epoxy resin and afterwards polished in order to achieve powder exposures on the surfaces. In-plane PFM measurements are carried out with an applied voltage of 3 V_{AC} at 7 kHz. Furthermore, the magnitude of the piezoresponse is measured as a function of the applied generator voltage.
Figure 4.5 shows the PFM results of both submicron and coarse reference $NaNbO_3$ crystals. Part *a)* and *b)* of Fig. 4.5 illustrate the topography of these samples, respectively. In the case of the submicron sample several grains of approximately 200 - 300 nm in diameter can be recognized. The corresponding in-plane piezoresponse signal is depicted in Fig 4.5 *c)* and *d)*. For the coarse reference sample only a very small and noisy signal is recorded. No correlation between the response and the topography can be found. On the other hand much larger piezoelectric displacements are measured for the submicron crystals. The regions of maximum piezoactivity correspond to the locations of the grains identified in the topography image and

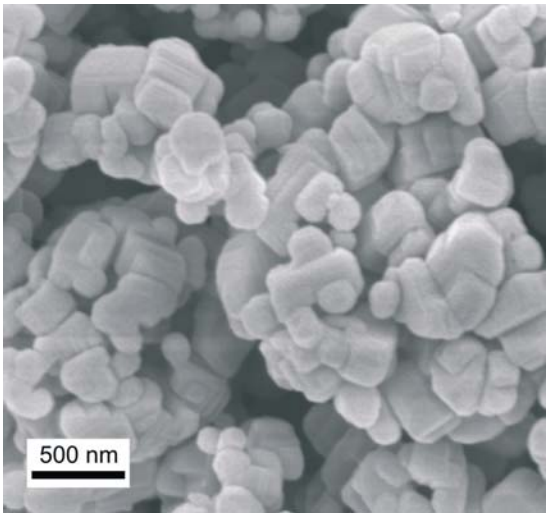

FIGURE 4.4: SEM micrograph of the submicron $NaNbO_3$ powder [94].

exhibit a maximum signal, which is more than 10 times the value observed for the coarse reference. For a more thorough comparison of both cases, the in-plane piezoelectric displacement was measured several times in dependence of the excitation voltage, using the same tip in order to reduce the influence of the tip form on the applied electric field [19]. The results are plotted in Fig. 4.5 *e)* and *f)*. In the case of the submicron sample an almost linear correlation can be found up to 2.5 V. Due to experimental limitations (drift of the PFM-tip) only 6 values can be recorded for each of the two measuring sequences. The lack of data for voltages above 2.5 V for this sample is believed to be related only to the instability of the tip with progressing time and not to the actual value of the voltage. As a reference, the in-plane piezoelectric response was measured several times on four different spots. In this case only signals with amplitudes ranging from 0.08 up to 0.4 a.u. can be recorded up to a maximum voltage of 5V. Up to this maximum the signal is only comparable to the noise value (0.65 a.u.) of the submicron sample.

Submicron sodium niobate particles exhibit a non-centrosymmetric phase as independently confirmed by the PFM measurements of this section. A discrimination of a ferroelectric against an antiferroelectric phase seems premature based on the findings illustrated in Fig. 4.5*e)* and requires additional experiments.

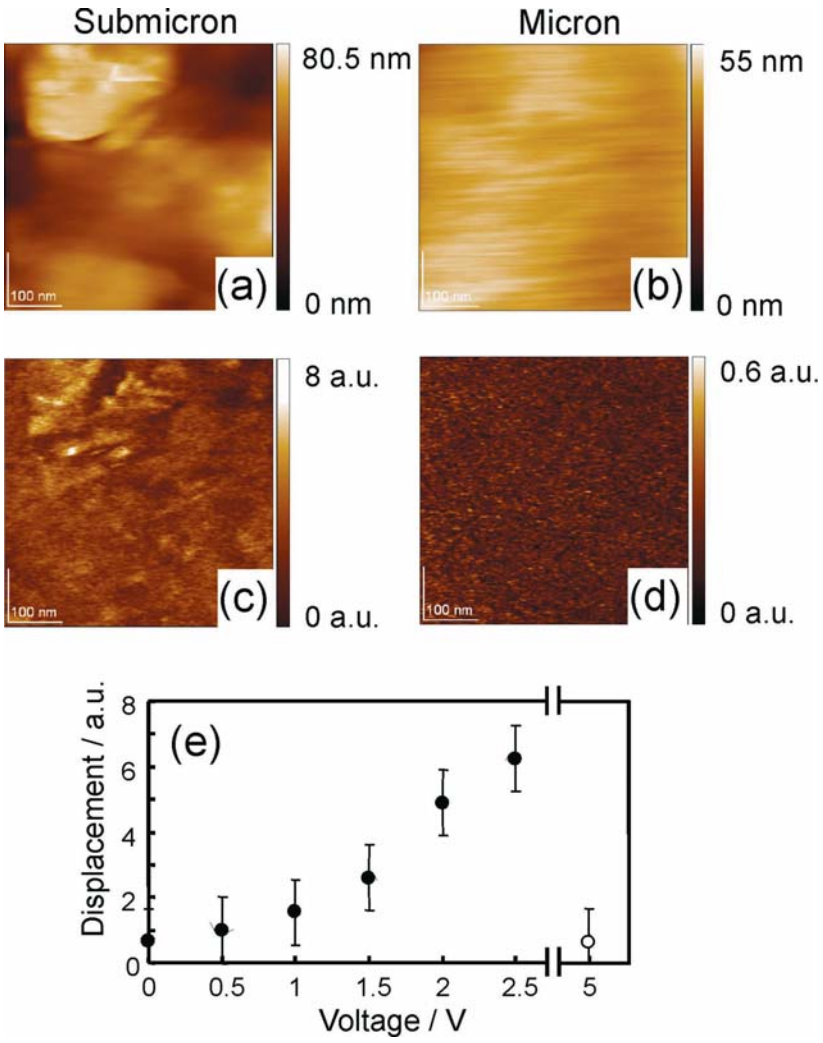

FIGURE 4.5: In-plane PFM images of a 500×500 nm^2 scan showing the topography (a, b), mapping (c, d) and voltage dependence (e) of the in-plane piezoresponse for submicron and coarse (f) $NaNbO_3$ crystals respectively. The error bars indicate the maximum mechanical uncertainty with respect to the measured piezoresponse signal [94].

4.2 Perimeter limitations in electromechanical force microscopy

In order to detect a linear piezoelectric response and to be sensitive for the phase shift between the applied field and the piezoresponse a moderate excitation field as compared to the coercive field is mandatory. As indicated above, the voltages actually applied to nanoislands might exceed the coercive field of bulk ferroelectrics. This section deals with the application of three different contributions that either enhance the coercive field or reduce the applied field in typical experiments. This is in line with the observation that PFM in fact does work in many cases where the bulk values of the coercive field already indicate a polarization reversal upon imaging.

In PFM an AC voltage is applied to the cantilever of an Atomic Force Microscope (AFM). The value of the coercive field of bulk BTO single crystals, measured at room temperature, varies from a minimum of 500 V/cm to a maximum of about 2000 V/cm [29, 95]. For $KNbO_3$ it is $5.5 \cdot 10^4$ V/cm [95]. When measuring the piezoresponse the applied electric field should be small, so as to be in the linear part of the "butterfly" loop and clearly below the coercive field as discussed in section 4.5.

Typical values of the applied field are in the range of 1 V and are applied to samples only a few tens of nanometers thick in some cases [96, 97]. Assuming a plate capacitor setup which does not take the field enhancement due to a sharp tip into account, this leads to an applied field above 10^5 V/cm. This exceeds the experimental values of the coercive field E_c of common bulk ferroelectric materials by two orders of magnitude. So why does the electric field in PFM stay below the threshold of nanoislands?

Measurements on grains suggest that the applied field is smaller than E_c. An enhancement of the piezoelectric response along the perimeter of grains often seen in PFM images can be explained by taking the spherical potential distribution as well as all direction of the piezoelectric tensor into account [19]. The best indication of successful PFM is the imaging of ferroelectric domains that would disappear if the coercive field was persistently exceeded.

4.2.1 Kay-Dunn-Law applied to ferroelectric nanoislands

Back in 1962 H. Kay and J. Dunn described the dependence of the coercive field E_c by a semi-empirical law [53]. They found that on Triglycine Suplphate crystals between 0.15 mm and

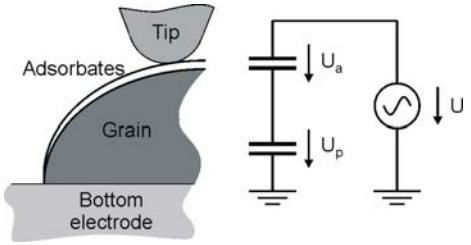

FIGURE 4.6: Model of an AFM tip contacting a ferroelectric nanograin. The adsorbate layer of constant thickness as well as the piezoelectric can be modelled as a capacitor. Only U_p of the tip voltage U_a is actually applied to the grain.

4.00 mm thick the coercive field shows a variation with the crystal thickness d according to

$$E_c(d) \propto d^{-2/3}. \tag{4.1}$$

Dawber et al. discussed [58] that the law holds true for different materials (PVDF, PZT, KNO_3) for films ranging from 100 μm down to 1 nm. For a 50 nm thick film a corrected coercive field of around 10^5 V/cm has been found for PZT and KNO_3. The extrapolated value for a 10 nm thick film is around 3×10^5 V/cm. With this thickness dependence the applied electric field is generally smaller than the coercive field.

4.2.2 Voltage divider due to adsorbates

In [17] and [98] it is shown that single crystalline $BaTiO_3$ and $KNbO_3$ are covered by adsorbates under ambient conditions and measurements on the influence of the adsorbate layer on the piezoresponse were presented. After partial removal of the adsorbates, an increase in the piezoresponse of at least 250% has been observed. Under the assumption of equal areas, the ratio of the voltages is:

$$\frac{U_p}{U_a} = \frac{\varepsilon_0\varepsilon_a\frac{A}{d_a}}{\varepsilon_0\varepsilon_p\frac{A}{d_p}} = \frac{\varepsilon_a d_p}{\varepsilon_p d_a}. \tag{4.2}$$

The applied voltage U is the sum of the U_a and U_p (Fig. 4.6):

$$U = U_a + U_p = U_p\left(1 + \frac{\varepsilon_p d_a}{\varepsilon_a d_p}\right) \tag{4.3}$$

$$U_p = U\left(\frac{1}{1 + \frac{\varepsilon_p d_a}{\varepsilon_a d_p}}\right) \tag{4.4}$$

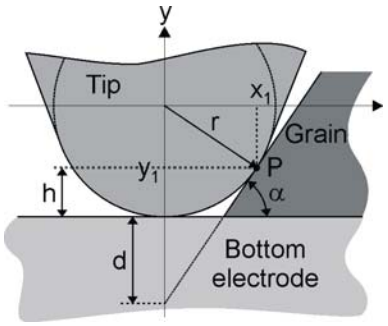

FIGURE 4.7: Scenario for the lowermost contact point just before the AFM tip shorts the electric field at the bottom electrode. The tip is assumed to consist of a half-sphere with radius r and an inclination angle α. Point P denotes the contact-point. The height h of the grain on top of the electrode cannot be contacted by the tip and cannot be characterized electrically or topographically.

Using the values of the simulation in [98] ($\varepsilon_p = 75$, $\varepsilon_a = 6$, $d_a = 2$ nm) the voltage over the piezoelectric is the following function of the thickness:

$$U_p \approx U \frac{1}{1 + \frac{25\text{ nm}}{d_p}} \tag{4.5}$$

In a first approximation the voltage over the piezoelectric follows the topography. The electric field at the piezoelectric is given by

$$E_p = \frac{U_p}{d_p} \approx U \frac{1}{d_p + 25\text{ nm}} \tag{4.6}$$

i.e. E_p increases with decreasing material thickness. For a negligible thickness d_p the maximum electric field E_p for $U = 1$ V is $E_{pmax} \approx 4 \times 10^5$ V/cm. This value is comparable to the coercive field of thin film $KNbO_3$. Taking just the adsorbates into account can explain why no ferroelectric switching occurs in PFM.

4.2.3 Influence of the tip radius

The AFM tip can be roughly regarded as a half-sphere with a radius r. Using the coordinate system shown in Fig. 4.7 with its origin in the center of this semi-sphere the tip-surface can be expressed geometrically as

$$y = -\sqrt{r^2 - x^2} \tag{4.7}$$

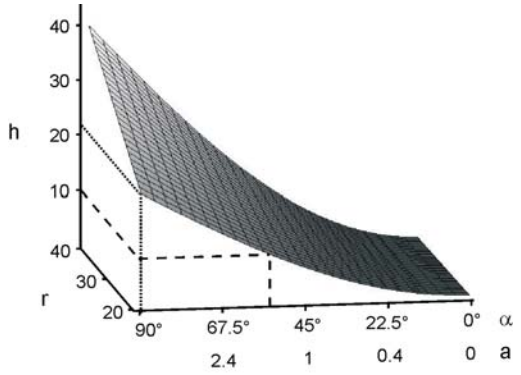

FIGURE 4.8: Inaccessible height h of a grain with an inclination angle α, slope $a = \tan\alpha$ and a tip with radius r. Note that for coated cantilevers ($r \approx 20$ nm) the inaccessible region can have a height of more than 10 nm for steep slopes.

The left border of the grain is defined by:

$$y = ax - d \tag{4.8}$$

At the point of contact between the tip and the grain the two slopes are equal. For the tip the slope is given as

$$\frac{dy}{dx} = \frac{x}{\sqrt{r^2 - x^2}} \tag{4.9}$$

The coordinates (x_1, y_1) of the contact point P are calculated to be

$$P = \left(\frac{ar}{\sqrt{1+a^2}}, -r\sqrt{1 - \frac{a^2}{1+a^2}} \right) \tag{4.10}$$

This results in a height h of

$$h = r\left(1 - \sqrt{1 - \frac{a^2}{1+a^2}}\right) \tag{4.11}$$

which is plotted for typical values of r and a (or the angle α) in Fig. 4.8. Note that for coated cantilevers ($r \approx 20$ nm) and steep grains the lowest 10 nm at the slopes cannot be detected, neither topographically nor electromechanically. As a result, no electric field is applied to the part of the ferroelectric grain less than about 10 nm thick. This further reduces the maximum electric field at the piezoelectric.

We have quantified three contributions to the applied electric field during PFM on ferroelectric nanoislands. Firstly, according to the Kay-Dunn-Law, the coercive field increases with decreasing crystal thickness. Secondly, adsorbates cover the piezoelectric acting as a voltage divider between tip and sample. Finally, due to the finite tip radius, certain parts like steep slopes close to the surface cannot be contacted at all. Combining all these effects supports the assumption that in many cases, no ferroelectric switching is induced in PFM measurements as long as the voltage is kept low.

4.3 Adsorbate-induced phase shift

Piezoresponse force microscopy is expected to provide a phase shift of π for antiparallel ferroelectric domains. As a general observation neither the parallel nor the antiparallel domain is exactly in phase with the excitation voltage. This can easily be attributed to time constants in the circuit such as the cantilever capacity with respect to the bottom electrode of the sample [90] but also mechanical vibrations may cause additional phases [88]. However, this phase shift should be identical for both polarization directions leaving the phase difference at π. Experiments instead do provide a frequency-dependent phase difference that might drop from π to almost zero.
Jesse et al. [22] invoked the global electrostatic contribution from the cantilever to introduce a phase shift which in principle allows to separate the electromechanical from the electrostatic contributions.

This model is now modified by an adsorbate-induced phase shift. Peter et al. [17] highlighted the relevance of adsorbates as a voltage divider that reduces the effective electric field at the sample surface by up to one order of magnitude, an effect that also had to be taken into consideration in various parts of this work. However, the adsorbates were always treated as part of a DC circuit, while PFM in fact is an AC technique.

A quantitative analysis of the polarization state of ferroelectric surfaces by Kelvin probe microscopy indicated that for ambient conditions, the surface charges of artificially written domains with a well defined polarization state were out of phase by π to what was expected from the free ferroelectric surface. The bound surface charges of the ferroelectric domain surface are instantaneously compensated by adsorbates of different polarity that invert the surface charge density. Under UHV conditions, after removal of any physisorbates, the anticipated surface charge is observed again.
Adsorbates are obviously domain specific and being part of the voltage divider, will not only

contribute their dielectric permittivity to the circuit but also their specific conductivity that gives rise to a domain specific RC-time constant that will subsequently be discussed.

Both amplitude and phase of the piezoelectric response are required to discriminate different types of domains and their relative orientation. Especially the phase contrast is the key to monitor the 180 degree domain pattern of technologically relevant thin films. Frequency dependent PFM scans on a PZT thin film with 180 degree domains are performed and a quantitative model of this additional phase shift is developed.
The sinusoidal modulation of the electric field E_0 causes a corresponding piezoelectric response that can be monitored as a deflection of a laser beam reflected from the backside of the cantilever according to:

$$E_0 \cdot \cos(\omega t) \rightarrow \Delta\ell \cdot \cos(\omega t + \varphi) \tag{4.12}$$

where t denotes the time, ω is the angular frequency, ℓ the sample thickness and φ is the phase-shift between excitation and measurement e.g. ideally 180 degree for polarization reversal. The piezoresponse is given as:

$$\Delta\ell = \ell \cdot d_{eff} \cdot E' \tag{4.13}$$

where E' denotes the electric field actually applied to the sample. Adsorbates reduce the applied field E_0 according to:

$$E' = E_0 \frac{1}{1 + \frac{\varepsilon_p d_a}{\varepsilon_a d_p}} \tag{4.14}$$

For an average angle θ between field and polarization vector as in polycrystalline samples d_{eff} is given by [99]:

$$d_{eff}(\theta) = (d_{31} + d_{15}) \sin^2\theta \cos\theta + d_{33} \cos^3\theta \tag{4.15}$$

The voltage divider created by the adsorbate layer between tip and sample as depicted in Fig. 4.6 has a capacity C and as it operates in an AC circuit with angular frequency ω we need to consider its resistance R as well since both induce an extrinsic phase shift φ according to:

$$\tan\varphi = \frac{1}{\omega RC} = \frac{1}{2\pi f \varrho \varepsilon \varepsilon_0} \tag{4.16}$$

Here the last term provides the geometry-independent description of our experiment, where f is the electric excitation frequency from the lock-in amplifier [100], ε_0 is the vacuum permittivity, ε the permittivity and ϱ the resistivity of the adsorbates. We treat the sample underneath as an insulator with a considerably higher permittivity than the adsorbates. The permittivity of the adsorbates was reported by Halbritter to amount to approximately 6 [101]. Note that the only remaining unknown is the adsorbate resistivity.

The polarization charges of the ferroelectric are compensated by adsorbates introducing an inverted surface potential as to what is anticipated from the polarization state [102]. Starting from this observation the physisorbates are carrying a charge: mainly anions for P^+ domains and preferentially cations for P^- domains.

Any difference in either the dielectric permittivity or the resistivity of the two adsorbate layers

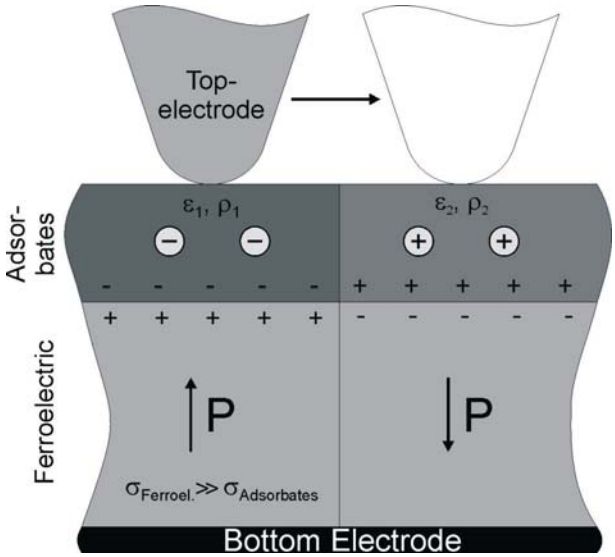

FIGURE 4.9: Sketch of the adsorbate coverage of different oriented domains. On the left side with an upward polarization and therefore positive bond charges at the surface cations adsorbate leading to a negative measured surface charge. On the right side the contrary situation is given leading to positive charged adsorbates. These different adsorbates may have different properties ε_1, ϱ_1 and ε_2, ϱ_2

will give rise to an individual frequency dependent phase shift according to Eq. 4.16 with distinct ε_1 and ϱ_1 for the P^+ domains and ε_2 and ϱ_2 for the P^- domains as depicted in Fig. 4.9.

Figure 4.10 illustrates the topography and piezoresponse phase image of the PZT sample under investigation with two areas of reversed polarization. We extracted the maximum phase difference between the nominally 180 degree domains as a function of frequency as illustrated in Fig. 4.11. According to Eq. 4.16 and considering adsorbates 1&2 with different properties

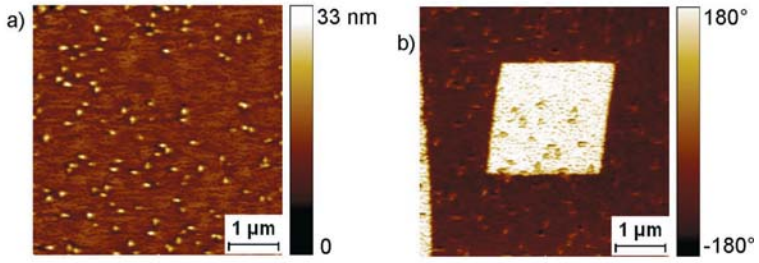

FIGURE 4.10: Topography (a) and vertical phase (b) image of an 5×5 μm^2 scan of PZT indicating antiparallel domains

we come to:

$$\begin{aligned} \Delta\varphi &= \varphi_1 - \varphi_2 \\ &= \arctan(\frac{1}{2\pi f \varrho_1 \varepsilon_1 \varepsilon_0}) - \arctan(\frac{1}{2\pi f \varrho_2 \varepsilon_2 \varepsilon_0}) \end{aligned}$$

Here, it is already worth stating that this model cannot account for phase differences larger than $\pi/2$ so it cannot be considered as a stand-alone model to replace the model of Jesse et al.
We consider the dielectric permittivity of both adsorbate layers relatively constant thus $\varepsilon_1 = \varepsilon_2 = 6$ which leaves us with two parameters ϱ_1 and ϱ_2 to fit. Fitting with a fixed conductivity of clean water for one adsorbate layer ($5 \cdot 10^{-6}$ S/m) provides a conductivity of 50% more for the other layer. This difference of 50% is marginal considering the wide range of conductivities over several orders of magnitude even for moderate electrolyte concentrations. In that sense the phase difference between ferroelectric domains as detected by PFM is inherently sensitive to adsorbates. Moreover the absolute values of water that is to well a resistor requires further consideration and experiments. In this model we treated the adsorbates as a homogeneous layer ignoring the chemisorbates that are unlikely to be domain specific adsorbates but may modify the overall conductivity.
In conclusion, the previous section provides a simple model of an in-series AC circuit element to show that the loss of domain contrast in PFM phase imaging originates from adsorbed water including domain specific ions. The experimentally determined difference in resistivity between adjacent domains is moderate thus suggesting a generally high sensitivity to adsorbates. Further investigations to determine a phase dependence from ambient conditions will help to model the layered adsorbate system.

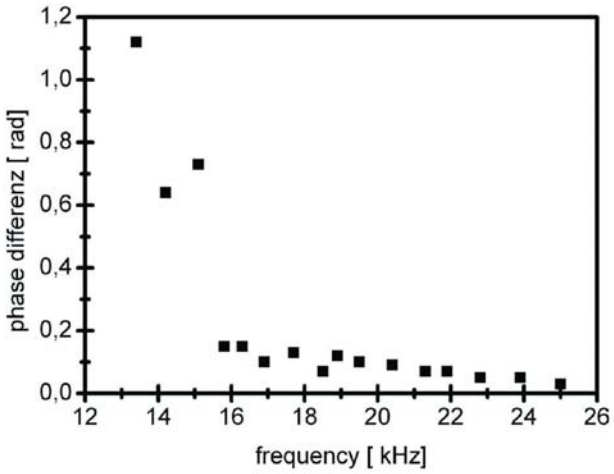

FIGURE 4.11: Maximum phase difference between the two antiparallel domains in dependence of the frequency

4.4 Detection enhancement for polarization reversal in ferroelectric nanoislands

Polarization reversal for technologically relevant applications and materials occurs in the direction perpendicular to the substrate and bottom electrode plane. This direction corresponds to the vertical deflection mode of the cantilever in PFM measurements, however lateral torsion of the cantilever benefits from a better optical enhancement due to the geometry of the optical lever-arm method, typically a factor of 20 [103]. The subsequent section proposes a novel detection scheme for the vertical polarization reversal by means of lateral PFM which makes use of the particular electromechanical response on the slope of a *c*-axis oriented nanoisland.
In reference [19] the origin of the enhanced signal on the slopes of the nanoislands was derived. In this section this detection enhancement for the polarization reversal as a proof for ferroelectricity is presented and discussed. Conventionally [104] the sample is scanned twice with an AC-field below the coercive field and in between with a DC-field exceeding this coercive field. Switching implies the inversion of the piezoelectric tensor which can be monitored as a phase shift of 180^{o} in the piezoelectric response between these two scans. This phase shift is monitored in the vertical piezoresponse on *c*-axis oriented $BaTiO_3$ thin films because switching occurs parallel to this direction. This vertical signal provides rather small signals with a weak optical amplification in comparison to the lateral signal, see Ref. [19]. So is there a pos-

sibility to use this enhanced signal for the detection of polarization reversal in *c*-axis oriented ferroelectric nanoislands?
Let us take a look at the influence of the polarization reversal and therefore an inversion of the piezoelectric tensor on this signal. Figure 4.12 shows a drawing of the top view on the situation. The AFM-tip is located at the slopes of a *c*-axis oriented nanoisland with the cantilever axis oriented along the *x*-direction. The positions *a* and *b* are the same as used in Fig. 4.13 which gives a side view of the same situation. The scanning direction has no influence on this effect, it is only affected by the cantilever axis. In part *a* of Fig. 4.13 the tip is located on the left side of the

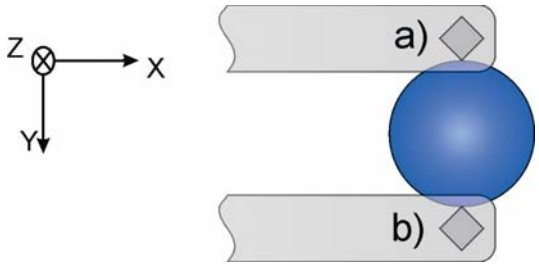

Figure 4.12: Top view of the discussed cantilever (gray) positions with respect to the slopes of the nanoisland (blue), adapted from [105].

nanoisland with a downwards pointing polarization. The application of a negative field leads to an elongation of the nanoisland along the *y*-direction and the tip is pushed into the -*y*-direction. A positive field leads to a contraction along this axis, but this motion is not detectable with the AFM-tip, because there is no force on the tip in this direction and therefore no movement of the tip. Part *b* of Fig. 4.13 shows the situation for a polarization pointing upwards which can be detected by a positive field and which then leads to a movement of the tip in +*y*-direction. Due to the same arguments as in part *a*, a negative field would not lead to any signal. In the piezoresponse force microscopy a sinusoidal field is applied which leads to the phase shift of 180° on the monodomain nanograin as shown in Fig. 4.14. This figure shows the simulation

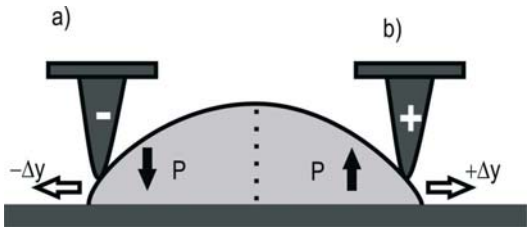

Figure 4.13: Side view of the situation at the slopes of the nanoisland parallel to the tip axis. In part a) the tip is pushed in the -*y* direction and in part b) along the +*y* direction

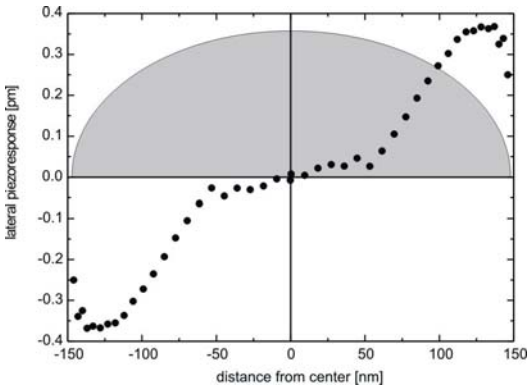

Figure 4.14: Finite element analysis of the lateral piezoresponse in y-direction as a function of the distance from the center of the *c*-axis oriented $BaTiO_3$ nanoisland. The sign of the piezoresponse depends on the sign of the slope.

of the lateral response on a *c*-axis oriented nanoisland in dependence from the distance to the center. Here the tip is moved to the opposite directions on the slopes with the same applied voltage. On a nanoisland as depicted in Fig. 4.13 with two antiparallel domains on the two complementary slopes the tip is also moved in the opposite directions but this time the applied field has also reversed directions. The application of a positive field leads to a movement of the tip along the $+y$-direction and the application of a negative field to an opposite movement of the tip. So the measured signal in position *a* and position *b* are in phase and the 180° phase shift of the monodomain grain disappears.
This means that a vertical polarization reversal in the nanostructure also leads to 180° phase shift in the lateral piezoresponse signal on the slopes of the structure. Consequently the polarization reversal and hence the ferroelectricity in c-axis oriented nanoislands should be detectable by the enhanced lateral piezoresponse signal on the slopes.

4.5 Polarization reversal during scans and loss of point contact

Piezoresponse force microscopy relies on the applied voltage to stimulate a piezoelectric response i.e. the piezoelectric tensor is defined in units of pm/V. One volt, be it applied to a thick or a thin sample will always cause the same elongation or contraction. Especially for the investigation of ferroelectric nanoislands this voltage cannot be increased arbitrarily as the bottom electrode is accessible by the tip and the resulting currents in case of a galvanic contact will wear off the tip rapidly. But even for low voltages this resulting electric field across the sample might become considerably close to or even larger than the coercive field, see section

4.2. In a good piezoelectric, one volt will cause a change in length of typically 100 pm which can still be monitored by a lock-in amplifier in the optical lever arm configuration. However this one volt applied to a structure of only 10 nm thickness creates a field of 10^8 V/m which is larger than most of the coercive fields, even when the thickness-dependent increase due to the Kay-Dunn law and the effect of a voltage divider due to adsorbates are considered. But what happens to a PFM scan if the applied AC-voltage reverses the polarization upon scanning? The question gained some very recent interest for the investigation of ultrathin ferroelectric films of only a few unit cells thickness [13]. Up to now there are no domain contrast images of these structures at all which could be an indication that the anticipated 180 degree domains are reversed upon scanning. To look further into the dynamics of this process underneath an AFM tip we investigated this scenario. Our findings on nanostructured ferroelectrics will be sketched and discussed in the subsequent paragraph and the experimental findings by electromechanical force microscopy at 2ω on the flat surface of a c-axis oriented ferroelectric nanoisland as well as from the slopes of these structures are in excellent agreement with the model prediction.
Moreover we present a new detection scheme to use lateral piezoresponse force microscopy for the local determination of the coercive field of PZT nanoislands. In contrast to the established way of the detection, where a DC-offset and an additional small AC-voltage is applied to the sample to obtain piezoelectric hysteresis loops, the method presented in this work just uses an AC-voltage for detection. Increasing the voltage above the coercive voltage leads to a strong qualitative change in the response measured at the second harmonic frequency of the applied voltage. Through the identification of the value of the applied voltage where the change in the response occurs the relative coercive field can be locally determined [4].
The local estimation of the coercive field is of a great importance for the characterization of ferroelectric nanostructures as it qualifies the basic needs for an operational device. Due to the need of fast memories with a low power consumption the coercive field should be low and the permanent polarization high. Like all nanoelectronic systems, these structures get more and more complex and smaller in their lateral dimensions [106]. So the measurements carried out on macroscopic top-electrodes can just give a statistic mean value over a big number of nanostructures. With the use of an AFM-tip it is possible to measure single nanostructures with a lateral dimension of a few nanometers. Up to now, the coercive field is estimated by measuring hysteresis loops of the materials. Therefore a DC-field is necessary as an offset and a small AC-field for the determination of the direction of the polarization with the piezoresponse of the material [107, 108]. The AC-field should be as small as possible but for sure lower than the coercive field. This technique relies on an AC voltage that is sufficiently small not to switch the ferroelectric as the DC voltage is still relatively far away from the coercive voltage which

[4] Absolute measurements of the coercive field require first of all the knowledge of the actually applied field at the sample surface which, due to adsorbates, is not necessarily identical with the applied field

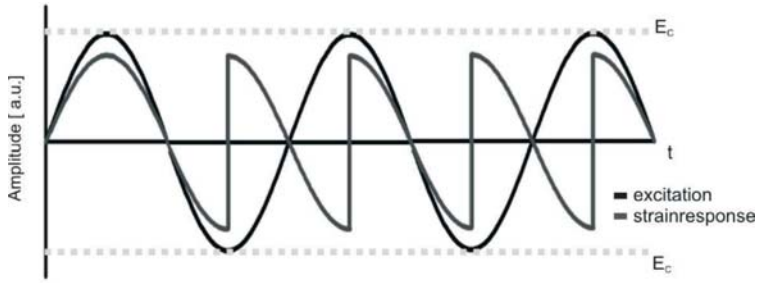

FIGURE 4.15: Amplitude of the applied field and strain response of the sample for an applied field reaching the coercive field so that switching just occurs at the maximum applied field

is not possible for all material systems.
With the method presented in this work only an AC-voltage is necessary for the estimation of the coercive field. In PFM measurements a sinusoidal field is applied to the sample for measuring the piezoelectric response [109]. But the general response of the material contains more terms which will not be measured during normal PFM measurements due to the restriction of the detected signal to the first harmonic ω of the applied field by the lock-in amplifier. The complete signal has also higher order terms of the applied field and the total response can be written as shown in section 4.6.
The response has a static term, a term proportional to ω, the piezoresponse and a term proportional to 2ω, the electrostriction. This equation is valid for applied fields below the coercive field. When the coercive field is reached, the behavior of the sample depends on the orientation of the polarization and the direction of the applied field respectively to each other. If the electric field and the polarization are parallel, the sample keeps expanding along this axis, the *c*-axis of the material, even when the coercive field is reached or exceeded, see Fig. 4.15. For an antiparallel polarization with respect to the applied voltage, the sample shrinks along the *c*-axis until the coercive field is reached. Then the polarization is suddenly switched and the applied field and the polarization are oriented parallel again. Within the next half-period of the applied voltage, see Fig. 4.15, the orientation is antiparallel again and switching occurs when the coercivity is reached. So the period length of the measured signals is divided in halves, which means that the signal is not periodic at the frequency ω, but at the second harmonic 2ω of it, just like the electrostriction. In contrast to the electrostriction, which is proportional to the square of the applied field, the piezoresponse stays linear in the field. So the measured signal at the second harmonic contains to different parts. One with the quadratic dependence of the electrostriction on the applied field, and another one that only occurs above the coercive field with the piezoresponse depending linearly on this field. Typical values for the piezoelectric tensor element d_{33} are of the order of 100 pm/V and for the electrostriction Q_{33} about 10 nm^2/V^2 [110]. Taking

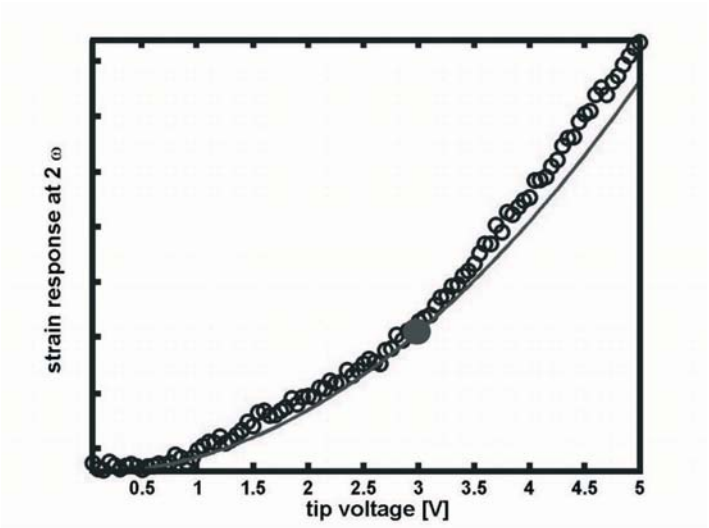

FIGURE 4.16: Measured vertical response at 2 ω and the quadratic fit for the electrostrictive fraction of the response measured on the top of a PZT nanoisland

the field dependence and the values into account the electrostriction should be the leading term in our signal.

To confirm these calculations and assumptions measurements are done on a PZT sample from M. Alexe from the Max-Planck-Institute of Microphysics in Halle. This sample consists of c-axis oriented nanoislands on a metallic $SrTiO_3$:Nb which means that the polarization is directed along this axis and switching will also occur parallel to this axis. Therefore the vertical response is measured at the second harmonic frequency of the applied voltage with the AFM-tip positioned at the top of the grain. The frequency of the applied field is 7 kHz and the voltage is increased from 0.05 V to 5V in 0.05 V steps. Figure 4.16 shows the measured response. The quadratic fit for low voltages (<3V) is also included and as can easily be seen above an applied voltage of 3 V the measured signals deviates from the quadratic fit. This observation is in line with the aforementioned considerations. As the coercive field is exceeded, the quadratic electrostriction term is complemented by a linear piezoelectric term. A closer look at the data reveals the linear characteristics of this additional term:

Figure 4.17 illustrates the difference between the best fit of a quadratic term with the values taken up to 3V and the total curve that also contains values above the coercive voltage. As can be seen in Fig. 4.17 they are around zero up to the estimated value for the voltage needed for switching ($\approx 3V$ due to the fit) and above 3V they are linearly increasing. This linear increase also confirms the estimated additional linear dependence of the measured signal at the frequency 2ω on the applied voltage due to the ferroelectric switching. The deviation from

zero at lower voltages is due to noise in the measured signal. The remaining problem is to find

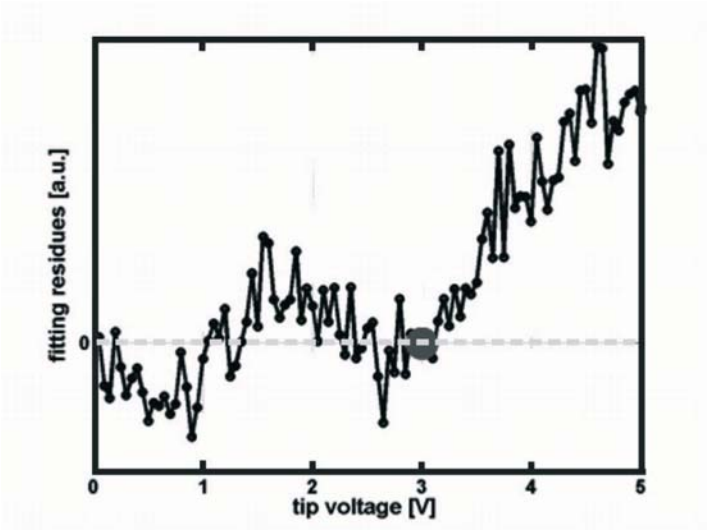

FIGURE 4.17: Residuals of the measured vertical response at 2ω from the quadratic fit with a constant value underneath and a linear increase above the coercive voltage.

the best quadratic fit to the measured values underneath the voltage necessary for switching without knowing this voltage. So it is important to have a good amount of measurement points below the coercive voltage to find out the best fit for this values. It is necessary to do several fits, which can be done by computer programs. In this sense the method is appropriate for automatization.

During the analysis of the signal measured at the slope of a nanoisland an interesting behavior in the lateral response can be seen as illustrated in Fig. 4.18. The dependence of the measured signal is, as expected and seen in the vertical signal, also quadratic in the applied voltage until the coercivity is reached. Above this value, the behavior changes unexpectedly to just a linear dependence of the applied voltage, without any quadratic behavior caused by the electrostriction. Moreover the signal becomes extremely noisy.

What is the reason of the loss of the quadratic response due to electrostriction? The situation for the two different tip positions on the nanoislands is sketched in Fig. 4.19. In position *a*, at the top of the grain, the sample is expanding or contracting along the z-axis parallel to the tensor element d_{33} depending on the direction of the applied field to the polarization. If they are parallel to each other the material is expanding and the tip is moving upwards. In an antiparallel configuration the nanoisland is contracting and therefore the tip moves downwards until the coercive voltage is reached. Then the grain is expanding suddenly and the tip shoots up. During this polarization reversal the sample surface is pushing the tip upwards and stays in

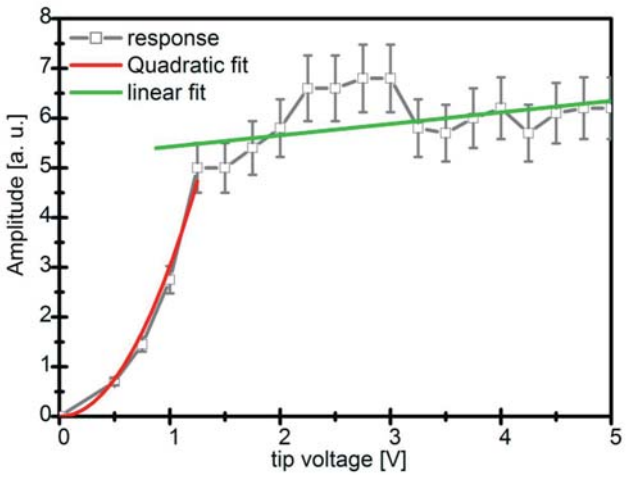

FIGURE 4.18: Measured lateral response at 2 ω including the quadratic fit for the electrostrictive part below and the linear fit for the part determined by switching above the coercive field at the slope of a PZT nanoisland

contact as the tip is pressed down with a force of typically 10 nN.

At the slope of the nanoisland shown in position *b* of Fig. 4.19 the situation is totally different. Due to the piezoelectric tensor elements d_{31} and d_{15} the nanoislands also contracts or expands along the x-direction [19]. When the direction of the applied voltage and the polarization are parallel, the grain contracts and with an antiparallel orientation, the nanoislands expands along this direction for an applied voltage. Below the coercive voltage, due to the Poisson ratio, the vertical expansion is associated with a lateral contraction, mainly to preserve the unit cell volume. Exceeding this coercivity, the grain keeps contracting for the parallel orientation. But for the antiparallel orientation the polarization switches and due to change in the orientation the grain contracts and the torque pushing the tip outwards suddenly vanishes with the speed of sound in the ferroelectric which is much faster than the resonance frequency of the cantilever. So the mechanical contact between the tip and the sample is interrupted and the electrostriction is not detectable anymore. The noise stems from the variation of the point of contact.

In this case the estimation of coercive voltage is much easier due to the obvious change in the dependence of the signal measured at the second harmonic on the applied field. Here no fit is necessary, but the measurements can only be done on the slopes of the nanoislands. Starting with this measurements, an upper limit for the coercive voltage at the top of the grain can be obtained due to the lower height of the nanoisland at their slopes.

The estimation of the coercive voltage with a PFM setup by application of only an AC-voltage

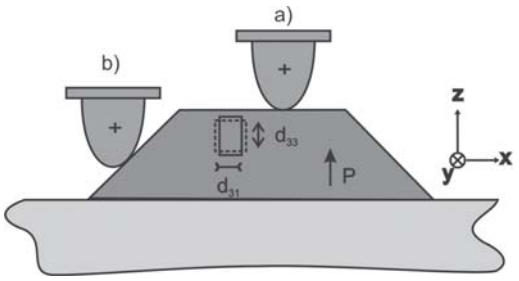

FIGURE 4.19: Sketch of the tip position on the grain. Upon polarization reversal, the tip on the top of the grain is pushed up a) and on the slope the contact between tip and sample is interrupted b), due to the elongation along d_{33} and the contraction along d_{31} during switching.

is shown. The response of the material at the second harmonic frequency of the applied voltage is detected. For the vertical signals the quadratic dependence of the applied voltage due to the electrostriction is measured as well as the additional linear dependence due to the piezoresponse for voltages above the coercive voltage. Measurements carried out at the slopes of the nanoislands show the quadratic behavior only for voltages below the coercivity. Above this voltage only the linear dependence of the piezoresponse is detectable due to the loss of the mechanical contact during switching. With these lateral measurements the value for the coercive voltage on the slopes of the nanoislands can be estimated quite easily. This value is an upper limit for the coercive voltage in the middle of these grains. There the value for the coercive voltage can be determined by implying a quadratic fit and thereby the voltage at which the additional linear term appears. To be able to create a good quadratic fit for the voltages below coercivity and not to include values above this point, the estimated value at the slopes of the nanoislands might be used as starting point for fitting the vertical data.

4.6 Detection of local defects at 2ω

The benefits of lateral piezoresponse force microscopy are not only restricted to the additional degree of freedom for an in-plane projection of the polarization. The optical amplification is typically a factor of 20 larger than for vertical detection and therefore provides a significantly better signal to noise ratio (in first order $\sqrt{20} \approx 4.5$). The exact values depend on the cantilever geometry as calculated in Ref. [111]. The electromechanical force microscopy is now operated at 2ω and offers a new possibility for the determination and investigation of local inhomogeneities and defects. It is based on a standard piezoresponse force microscopy used for the characterization of piezoelectric samples. But with very small changes in the settings of the lock-in amplifier the method can be used for the detection of local defects in

non-piezoelectric samples. Extensive and destructive sample preparations like for transmission electron microscopy are not necessary anymore with just a small loss in the lateral resolution from atomic resolution to a few nanometer resolution like in piezoresponse force microscopy. The concept has been filed for a Patent by the author.
The detection of local defects and inhomogeneities rises great interest due to smaller and more complex nanostructures fabricated and used in nanoelectronics for example like strained silicon. So far this detection is done by transmission electron microscopy (TEM) [112]. This method delivers atomic resolution [113] but a very extensive sample preparation is necessary for those measurements. For example the samples have to be cut in very thin slices which means obviously that TEM is a destructive analysis method. The new approach presented in this work, the electromechanical force microscopy (EMFM) is based on a conventional piezoresponse force microscope (PFM). PFM is a well established method for the investigation and characterization of piezo- and ferroelectric samples [104, 114–116]. In PFM measurements a sinusoidal AC-field is applied to the sample and the piezoelectric answer is detected by a lock-in amplifier. In the electromechanical force microscopy the excitation and the detection with a lock-in amplifier is similar but the detected signal is the electrostrictive answer and not the piezoresponse. With the applied sinusoidal field the electrostriction can be measured at the second harmonic of the applied frequency. So only the 2ω button at the lock-in amplifier has to be pressed to change from the PFM setup to the electromechanical force microscopy. This method delivers the same lateral resolution as PFM, of about a few nanometers. This defect detection can also be done by piezoresponse force microscopy [28] but then a limitation to at least piezoelectric samples is obvious. Measuring the electrostriction of the samples allows the use of samples without any restriction due to symmetry or crystal classes.
How does the detection of inhomogeneities with a PFM or EMF setup work? Applying an AC-field to a piezoelectric sample leads to a strain response of the sample underneath the tip which includes terms of different order of the applied field

$$\eta_{ij} = d_{ijk}E_k + Q_{ijkl}E_kE_l \tag{4.17}$$

Here η_{ij} is the strain of the sample, d_{ijk} the piezoelectric tensor, Q_{ijkl} the electrostriction and E_k and E_l the applied fields.

With a sinusoidal field $E = E_0 cos(\omega t)$, where ω is the angular frequency of the applied field and *t* the time, equation 4.17 can be written as

$$\eta_{ij} = d_{ijk}E_k cos(\omega t) + \frac{1}{2}Q_{ijkl}E_k^2(1 + cos(2\omega t)) \tag{4.18}$$

Here it can be seen that the electrostriction is detectable at the second harmonic 2ω of the applied field. If now a non-piezoelectric sample is used, the piezoelectric tensor vanishes and equation 4.18 changes into

$$\eta_{ij} = \frac{1}{2} Q_{ijkl} E_k^2 (1 + cos(2\omega t)) \tag{4.19}$$

This strain response can be detected by the EMFM-setup by filtering out the parts of the measured signal appearing at 2ω with a lock-in amplifier.
Previous work showed the influence of defects on the lateral piezoelectric response [28]. A finite element simulation of the applied field to symmetric $BaTiO_3$ single crystal shows a symmetric potential distribution in the plane of the sample underneath the tip, see Fig. 4.20 [28]. The electric potential underneath the tip is not spherical due to the different dielectric constants along the different crystal axes but either a rotational oblate or prolate ellipsoid. With a symmetric potential distribution no lateral piezoresponse or electrostriction can be measured because all lateral components in the plane of the sample cancel out each other.

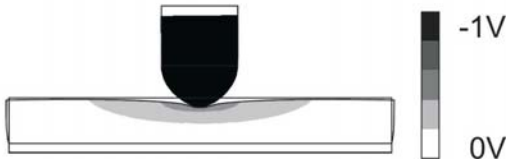

FIGURE 4.20: Simulated potential distribution for a tetragonal anisotropic sample adapted from [28]

With a given defect or inhomogeneity in the sample, the situation shown in Fig.4.20 changes. These defects imply a change in the dielectric constant and therefore the symmetry is broken and a lateral piezoresponse and electrostriction is measurable. Figure 4.21 *a)* shows the distribution of the electrostriction and part *b)* the cross-section of the measured signal over the inhomogeneity. The value for the dielectric constant ε in the inhomogeneity is increased of about 10% above the surrounding bulk value [28] during the simulation. The lateral signal depends on the distance from the center of the inhomogeneity, as shown in Fig.4.21*b)*. If the tip is far away from the defect, there is no influence of the increased dielectric constant on the measurement, the symmetry is given and no lateral electrostriction is measurable. When the tip is scanning closer to the defect, the influence of the changed dielectric constant becomes relevant and the lateral signal is increasing until the inhomogeneity is reached. At its center the signal is zero again because the symmetry in the plane of the sample is restored. Scanning further on, the signal reaches its maximum again at the slope of the defect and decreases to zero when the tip is far away from the sample. In contrast to PFM measurements the phase of the signal has no significance.

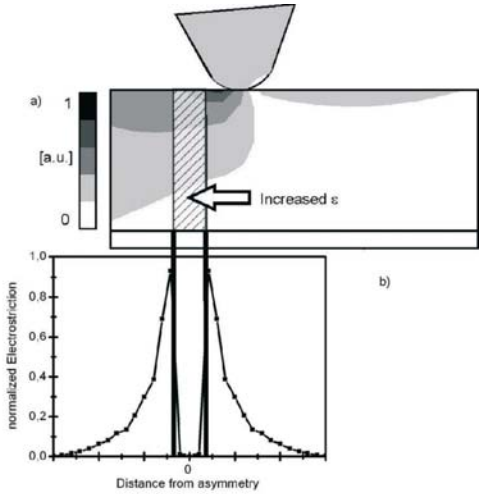

FIGURE 4.21: Simulated potential distribution for a $BaTiO_3$ sample at an inhomogeneity with an increased dielectric constant (a) and electrostriction for a scan over the inhomogeneity (b). Note that the slopes are steeper than for the piezoelectric simulation shown in [28]. Experimental evidence of this simulation is given in Fig. 4.23.

One possibility for measurable inhomogeneities are misfit-dislocations due to different lattice constants in epitaxial heterostructures. Up to a critical thickness this lattice-mismatch leads to a strained material, which can have improved performances like strained silicon in semiconductor devices for example. Above this critical thickness misfit-dislocations are implemented to inelastically accommodate the strain. In this work a $BaTiO_3$ thin film grown on a $SrTiO_3$ substrate is investigated. $SrTiO_3$ is cubic at room temperature with a lattice constant of a=0.3905 nm [117] and $BaTiO_3$ is tetragonal below 130°C with lattice constants of c=4.036 nm and a=0.3992 nm [117]. The outcome of this is a lattice mismatch of 2.2% between the a-axes of the two materials. Misfit-dislocations in this system have been investigated by TEM [118]. The here investigated $BaTiO_3$ thin film has a thickness of 60 nm which is thicker than the critical thickness of the system, so misfit-dislocations should exist and independent XRD measurements confirmed their existence above 30 nm thickness.
High-quality eptiaxially grown heterostructure $SrRuO_3$-$BaTiO_3$ was deposited by high pressure sputtering technique [119] on (001)-oriented $SrTiO_3$ substrates. The substrates were used as received i.e. no further chemical or thermal treatment was applied. The conductive $SrRuO_3$ layer was grown at a substrate temperature of 610 ° C and the oxygen partial pressure inside the sputtering chamber was kept at 3 mbar. The $BaTiO_3$ films were deposited at 700 ° C in a 2.6 mbar pure oxygen atmosphere. These two layers were grown in situ with the $BaTiO_3$.

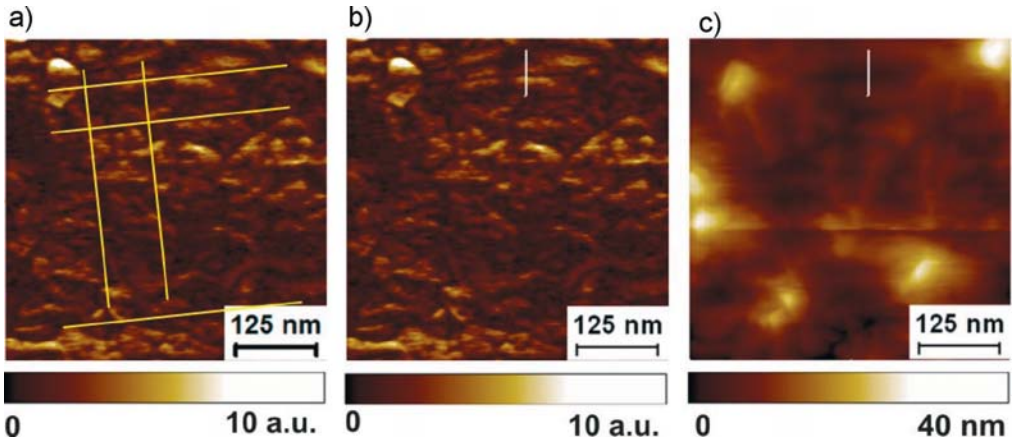

FIGURE 4.22: EMFM measurement of a 500 $\times$ 500 nm^2 scan of a $BaTiO_3$ thin film at 2ω. Part a) shows the electromechanical response with the dislocation emphasized by the yellow bars. The same image is shown in part b) without these bars to enable a closer look on the measured results. Part c) shows the topography . The small white bar in part b) and c) indicates the area of the cross-section shown in Fig.4.23.

The heterostructure was then investigated at room temperature in the as-grown state without postprocessing.
X-ray diffraction was performed with a Philips X'Pert High resolution diffractometer and indicated that the $BaTiO_3$ films crystallized in the tetragonal (4mm) phase with the c-axis orthogonal to the substrate plane. The $BaTiO_3$ film initially grows coherently on the $SrTiO_3$ substrates as confirmed by ϕ-scans of the (101) reflection, and the ω-scan of the (002) reflection shows that it has a high degree of crystallinity. Additional details on the crystal growth and structural analysis can be found in Ref. [120].

The electromechanical force microscopy measurements on this sample are done at an applied frequency of 7 kHz and an amplitude of 2 V on a scan area of 500 x 500 nm^2 with a standard PtIr-coated contact-cantilever. For the detection of the electrostriction the lock-in amplifier is set to measure the signals at the second harmonic of the applied frequency. The experimental results are shown in Fig. 4.22, part *a* and *b* show the lateral electrostriction and part *c* the topography of the investigated area. The measured lateral electrostriction shows clearly the expected lattice-structure of misfit dislocations as can be seen in Fig.4.22 *a)* emphasized by the yellow lines in the figure. To get a closer look on the measured results, part *b)* of Fig. 4.22 shows the same picture without the yellow bars. Here the misfit-dislocation can be seen as a black line, which implies a very weak measured response. The white line symbolizes the

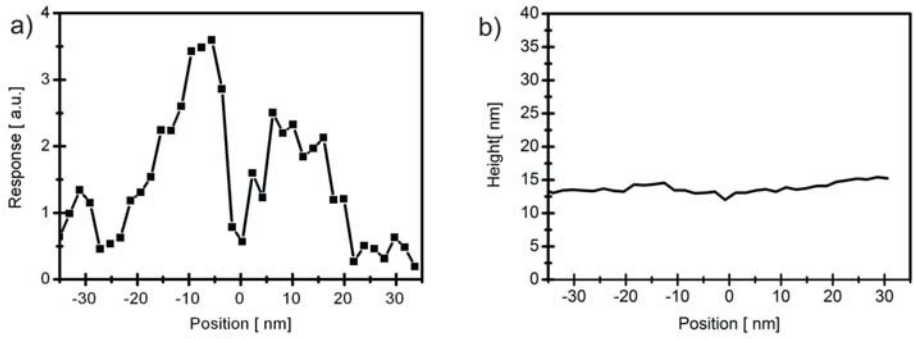

FIGURE 4.23: Cross-section perpendicular to the dislocation shown in Fig. 4.22 of the electromechanical response (a) and the topography (b). Note the good agreement of the experimental and simulated values (shown in Fig. 4.21).

area of the cross-section over the dislocation shown in Fig. 4.23*a*). This cross-section shows the measured lateral electrostriction in dependence of the distance of the center of the dislocation. The measured electrostrictive response is also very weak far away from the sample and increases when the tip is approaching to the dislocation. Also the drop of the signal at the center of the dislocation is measured. So the experimentally obtained cross-section confirms the simulated values. The underground value of the measured signals is due to electrostatic contributions. Topography effects can be excluded as the sample surface is extremely flat (rms < 1 nm).

The measured topography in Fig. 4.22*c)* and the cross-section of the topography scan at the same place as in the electrostriction shown in Fig. 4.23*b)* show no significant change in the topography at this place. That underlines that a real electrostrictive signal is measured without any relation to the topography.

This section establishes a novel method for the detection of local inhomogeneities on the nanoscale with some advantages in comparison to the established methods for example: a non-destructive approach without need for a sample preparation as long as it fits in the AFM setup. The setup for the EMFM can be realized with every standard PFM just by setting the lock-in amplifier on the 2ω detection. Dislocations are detected by the electrostrictive answer of the sample and the experimental results show a good agreement with the finite element simulations. Measurements were carried out on a ferroelectric and hence piezoelectric $BaTiO_3$ thin film but due to the measured electrostriction which is not restricted to this classes of materials it should also be possible to obtain signals from dislocations in non-piezoelectric materials like silicon for example which is of a great interest in the semiconductor industry.

4.7 On the origin of the perimeter enhancement in pyroelectric scanning microscopy

As both the third-rank piezoelectric tensor as well as the first-rank pyroelectric tensor are closely related to the structural preconditions of ferroelectricity, both of these effects have been used to investigate finite size effects in ferroelectrics. A very detailed analysis of piezoresponse force images that indicated a perimeter enhancement [19] revealed that on ferroelectric nanoislands of about 100 nm diameter no lateral finite size effect could be observed.
Peterson et al. [11] published results on a perimeter effect in PVDF-thin films that were sandwiched between Al-electrodes in a crossbar structure. The idea of the experiment is as follows: A pulsed laser is scanning the surface of the thin top electrode in the area of the crossbar intersection. Each pulse deposits a certain amount of energy, thus heat ΔQ. This heat is translated into a change in temperature ΔT by the specific heat capacity C_p as long as thermal conduction can be neglected. In fact this turns out to be the crucial mistake of this experiment as published. According to the line of argument of the authors, the heat is converted into a change in temperature according to:

$$\Delta T = C_p \Delta Q \tag{4.20}$$

This change of temperature is translated into a change of polarization and therefore surface charge density (which can be monitored in an external circuit as the pyroelectric current) according to:

$$\Delta P = \gamma \Delta T \tag{4.21}$$

where γ denotes the pyroelectric tensor. This pyroelectric tensor is proportional to the change of polarization as a function of temperature, seen from the partial derivative of the last equation. In particular, this yields a diverging pyroelectric coefficient in the proximity of ferroelectric phase transitions where P disappears. In the case of a size-driven phase transition with a modified polarization in the surface of the ferroelectric (at the perimeter of the PVDF film), γ should therefore become large at the perimeter indicating the proximity of a phase transition. As the laser is now scanning the surface and depositing equal amounts of heat at various positions of the sample, the idea is to obtain a map of γ as the pyroelectric current is always mapped after every single light pulse.

The experiment as depicted in Fig. 4.24 however only shows a perimeter enhancement at the parallel sides where the top electrode ends. This is not in line with the argument that the perimeter in general should be different.

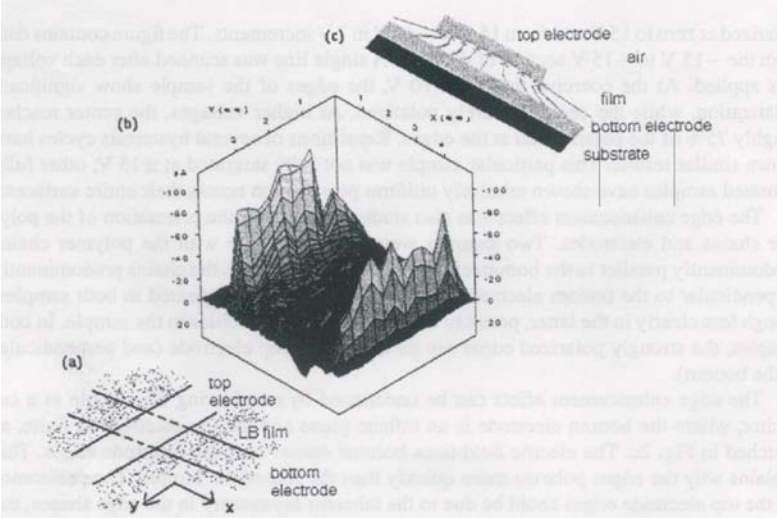

FIGURE 4.24: Top-view of the PVDF-thin film sandwiched between Al-electrodes in a crossbar structure (a), mapping of the heat distributon showing largest values at the edges of the top electrodes (b) and side-view of a single crossbar (c) [11]

A closer look at the experimental configuration shows that the thermal conduction must not be neglected. Experiments with lasers that are cutting steel sheets demonstrate that a laser with constant power propagates much faster as it cuts through the edge of a sheet than it does at the center. The explanation is due to the loss of thermal energy by thermal conduction. At the edge, the steel sheet and the aluminium top electrode are limited by a poor thermal conductor on one side, air. The change of temperature for a given amount of heat is thus considerably larger than in the center of the structure where heat is dissipated into all radial directions and not just a half-plane. For the assumption of a perfect thermal insulator at the outside of the structure, the Greens-functions look exactly like for an electric field distribution with an image charge at the opposite side of the surface and therefore provide a temperature change which is exactly twice as large as in the center. Numerical simulations with finite elements according to the equations from Ref. [121] are illustrated in Fig. 4.25 and 4.26. The first simulation shows the Gaussian distribution of the thermal profile under perpendicular illumination with a TEM 00 mode laser while the second simulation compares the temperature change in the center of the structure with a change in temperature at the perimeter. The simulations are in good qualitative agreement with the experiments in Ref. [11].
In principle this method provides a pyroelectric current but the assumption of a constant change of temperature was too strong, as in fact these images provide a map of the temperature change instead of γ-maps.

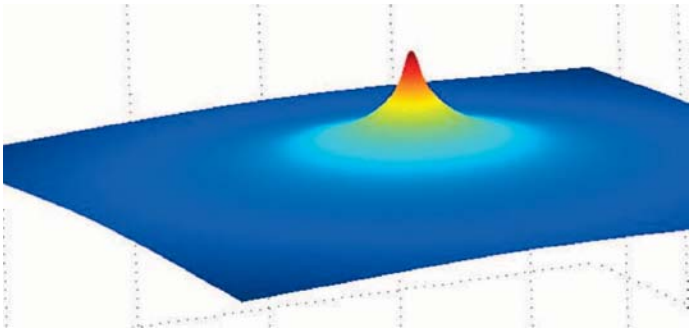

FIGURE 4.25: Thermal profile under perpendicular illumination of the sample with a TEM 00 mode laser and an isotropic lateral thermal conductivity of the sample.

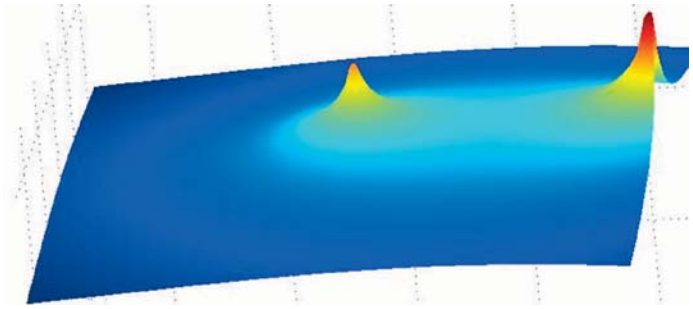

FIGURE 4.26: Comparison of the temperature change in the center and at the perimeter of the structure

4.8 Effect of the top electrode geometry on the perimeter enhancement in dielectric impedance spectroscopy

This section briefly suggests an additional contribution to the model provided by Dawber et al. [12] on the origin of dielectric loss peaks in ferroelectric nanocapacitors. In their original publication they attribute the frequency dependence of the dielectric losses to a preferential nucleation along the perimeter of the capacitor due to strain. Their findings are self-consistent in terms of the involved phonon-frequencies and quantitatively explain the frequency dependence. We also invoke a field-enhancement due to the geometry of the top electrode [122] that might facilitate the nucleation of domains along the perimeter. This leaves the physics of the domain propagation unaltered, it essentially adds to the activation of ferroelectric domain nucleation. While compressive strain, as described in the paper, is known to reduce the coercivity, the geometry of the top electrode (which is smaller than the active capacitor structure) contributes a field enhancement as depicted in Fig. 4.27. Exact figures are difficult to determine as the edges are not well defined but their curvature enters directly into the field enhancement factors.

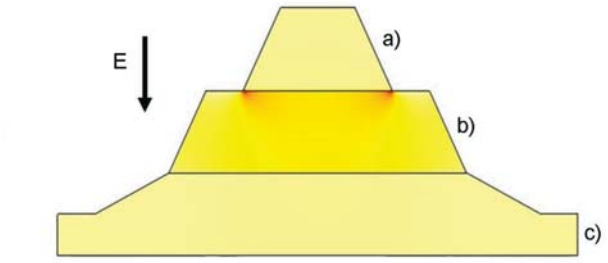

FIGURE 4.27: Sketch of the capacitor structure with : the top electrode a), the ferroelectric b), and the bottom electrode c). The local field enhancement takes place in the ferroelectric underneath the perimeter of the top electrode

In addition the fabrication of these capacitor structures might also leave some of the perimeter damaged which will not interfere with the domain propagation towards the inner part of the capacitor but which might contribute to the screening of the field.

This part of the thesis underlined the relevance of piezoresponse force microscopy for the investigation of novel polar material systems and various structures on the nanoscale, its imaging capabilities and several ways to extend the scope of this technique beyond present fields of application. The use of the higher optical amplification of the lateral signal for the enhancement of the detection for polarization reversal and in particular the use of the second harmonic signature of polarization reversal for applied fields above the coercive field gives the possibility for the investigation of ultrathin films and nanostructures. As the applicability of this scanning probe technique will, by measuring the electrostriction instead of the piezoelectric response,now also be shifted to non-piezoelectric materials, the major challenges of this method however remain and became even more obvious by this work, showing some of the limitations and influences like, thickness, shape, adsorbates and possibilities to overcome a few of the them, like in particular the measurements of the electromechanical response instead of the piezoresponse. To obtain quantitative data on ferroelectric nanostructures is virtually impossible as the determination of the polarization by PFM generally requires particular assumptions about the materials system [5] and additional knowledge of both the dielectric permittivity and the electrostriction, both of which are not well documented in most material systems. The second macroscopic key figure of ferroelectrics, the coercive field, is even more problematic as shown by Peter et al. [17]. The necessary mechanical contact for the electrical characterization

[5]The direct association between the piezoelectric tensor element d_{33} and the polarization requires the assumption of a cubic paraelectric phase

can either be chosen soft, i.e. with a cantilever that has a low spring constant or hard i.e. high spring constant. For the first case, the tip will essentially ”float” on the adsorbate layer with a poor electrical contact or make a nanoindentation for the latter case with entirely modified mechanical boundary conditions due to clamping and an additional drawback as the scanning to find an appropriate spot becomes abrasive.

This work also emphasized that the use of PFM for ultrathin structures may completely lose the information of relative domain orientation (cf. section 4.5). So the reversal of the polarization by ferroelectric or piezoelectric hysteresis loops and the in this work presented estimation of the linear dependence of the field in the measured second harmonic become the only ways to probe ferroelectricity. However, the mere existence of a polar phase (pyroelectricity) still holds the promise for the existence of ferroelectricity and has been subject to various studies, either by direct pyroelectric imaging on ferroelectric thin films [11] or Raman investigations on these structures. During the last decade, the scope of Raman studies has been widened to polar nanoislands. In contrast to pyeoelectric current imaging, Raman imaging requires fewer assumptions about the thermal properties of a material. However, both methods are traditionally limited in lateral resolution by the optical diffraction limit and Raman in particular suffers from a poor cross-section for the excitation of optical phonons. The second part of this work is therefore dedicated to develop a new Raman microscope that uses the near-field enhancement at a metallic tip to overcome these limitations and to allow for Raman investigations with nanoscale resolution on individual ferroelectric nanoislands.

5 Raman spectroscopy

After the discussion of several limitations of piezoresponse force microscopy at the end of the last paragraph, this chapter addresses a novel imaging scheme to extract quantitative data of the ferroelectric properties by optical phonon spectroscopy. This part of the work is therefore devoted to an extension of Raman spectroscopy by means of an additional noble-metal-coated tip in the proximity of the sample surface to locally enhance the electrical laser field, a technique that recently became known as tip-enhanced Raman spectroscopy (TERS). This method paves the way to enhance the cross-section of Raman scattering by several orders of magnitude and at the same time, to undergo the optical diffraction limit of confocal Raman imaging with the evanescent field at the tip apex that provides an aperture-free resolution as small as 15 nm.
Raman scattering, also for the case of TERS, interacts differently with the sample as compared to PFM. Piezoresponse force microscopy relies on the contact-area between tip and sample to determine the electric field inside the material. This field creates a certain volume of interaction and thus PFM integrates a piezoelectric response from within a certain volume, the symmetry of which can be used for various means of application, as discussed in the previous section. Tip-enhanced Raman relies on the evanescent and therefore rapidly decreasing near-field at the apex of a tip and will therefore also integrate over a finite volume underneath the surface of the sample, certainly a lot smaller than the wavelength of the light divided by the refractive index. To some extent this method might therefore collect data from the substrate but the key advantage is that it is contact free and therefore less susceptible to extrinsic contributions such as adsorbates. Adsorbates do have a Raman signature of their own; this is in particular true for carbon-derivatives. A laser focus with an optical near-field creates extreme gradients of the electric field and will therefore act like a ”nano-vacuum cleaner” at the sample surface. All kind of dipoles will stick to the tip and sooner or later deteriorate the signal, an effect that often occurs under ambient conditions already in the first hour of operation. This is why we decided to move this setup right into the vacuum [6]. This chapter describes in detail by which criteria and how the setup was designed and eventually realized. Starting with the laser wavelengths, shape and coatings of the AFM tips and the different methods to achieve these coatings, going on with the optical setups and the choose of the AFM system ending with the description of the first TERS experiments under ambient conditions and confocal Raman measurements documenting the advances towards this goal.
TERS is a surface sensitive method with a lateral resolution of more than one order of magnitude below the diffraction limit. So far, it has mainly been applied to material systems such as

[6] It should however be kept in mind that UHV conditions, or thermal treatment in UHV to prepare a certain sample surface condition might deteriorate or even destroy perovskite structures, this will be subject to additional investigation.

carbon nanotubes on metallic surfaces, so the tip could be readily realized by an STM tip. Perovskite ferroelectrics are wide-bandgap semiconductors and therefore not accessible by STM, especially not when they are dispersed on a metallic substrate. Any scan across this surface will provoke a tip crash due to the extremely different electrical conductivities. This is why our experiment uses an AFM. For a couple of reasons that will be described in the theoretical part of this chapter, non-contact mode AFM turns out to be more beneficial than contact mode AFM.
The theory of TERS in terms of the origin of the field enhancement is still in its infancy and subject to an ongoing debate as referred to in this section but even more demanding is the understanding of the photon-phonon coupling in the material. The ferroelectric soft-mode phonon condenses at Γ=0 as it is a global transition of the structure. In a finite structure with dimensions well below the wavelength of the excitation lightsource, the theory needs to be adapted to this finite size effect. This theoretical work goes beyond the scope of this thesis but should be taken into consideration for future investigations.

5.1 Principles of Raman scattering

The first publication on Raman scattering was published in 1922 by the Indian physicist Sir Chandrasekhara Venkata Raman and in 1930 he was awarded the Nobel prize for his discovery of inelastic scattering of photons [123–125]. When light is scattered from an atom or molecule, most photons are elastically scattered, the so called Rayleigh scattering, which means that they have the same frequency (energy) as the incident photons. A very small fraction of about 10^{-7} of the light is inelastically scattered, see Fig. 5.1. The difference of the energy between the incoming and scattered photon can be written as:

$$h\upsilon = h\upsilon_0 \pm h\Omega \tag{5.1}$$

where υ_0 is the frequency of the incident light, υ of the scattered light, Ω of the elementary excitation, and h the Planck constant. The energy difference is used for excitation, Stokes scattering with a lower frequency of the scattered photon (minus sign in Eq. 5.1), or for de-excitation, anti-Stokes scattering with a higher frequency of rotational or vibrational states of the molecule (plus sign in Eq. 5.1). If instead of a molecule a crystalline solid-state sample is used for investigation, the energy is used for the excitation of lattice vibrations e.g. the soft modes of ferroelectricity. Stokes scattering is always dominant, since the vibrational ground state, according to the Boltzmann distribution, is always more populated than the excited states. In fact the ratio of Stokes to Anti-Stokes lines of corresponding vibrations is a direct indication of the sample temperature. The incident photons will thus interact with the present absorber,

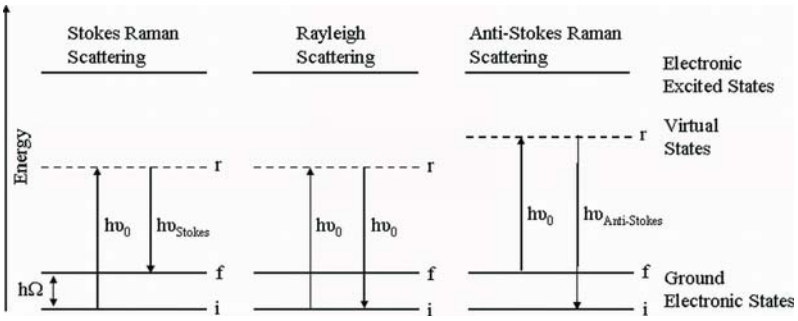

FIGURE 5.1: Energy diagram for the different types of light scattering, adapted from [126].

and the amount of energy change by a photon is a fingerprint of the nature of each bond or vibration that is associated with a change in polarizability i.e. Raman-active. Those vibrations associated with a change of the dipole moment are Raman-inactive but IR-active. Illuminating a bond with light, a dipole moment μ is induced depending on the polarizability α of the sample and the electric field from the incident light $E = E_0 cos(2\pi\upsilon t)$ with the frequency υ_0 given by:

$$\mu = \alpha E_0 cos(2\pi\upsilon_0 t) \tag{5.2}$$

If an additional vibration Ω which changes the geometry and polarization of the dipole occurs, the polarizability can be written as

$$\alpha = \alpha_0 + \alpha' cos(2\pi\Omega t) \tag{5.3}$$

leading to a dipole moment

$$\mu = \alpha_0 E_0 cos(2\pi\upsilon_0 t) + \frac{1}{2}\alpha' E_0[cos(2\pi(\upsilon - \Omega)t + cos(2\pi(\upsilon + \Omega)t)] \tag{5.4}$$

Here again the three frequencies for the Rayleigh, Stokes and Anti-Stokes scattering are visible. In addition it becomes obvious that the Raman scattering takes place only for $\alpha' \neq 0$ that means for vibrations with a change in the polarizibility. In equation 5.4 the polarizability is used as a scalar but in reality it can vary for the different axes and a tensor notion is necessary. Although not every vibration is detectable with Raman spectroscopy sufficient information is usually present to enable a very precise characterization of the structure which makes Raman spectroscopy one of the most important tools in analytical chemistry and physics.
A big disadvantage of Raman spectroscopy is the very poor cross-section of Raman scattering of 10^{-28} to 10^{-31} cm^2. Therefore a high laser power, which may damage or even destroy the sample, a large quantity of the investigated material, which is not possible for nanostructures

or molecules and highly sensitive detectors are necessary. To overcome this problem near-field enhancement methods like surface-enhanced and tip-enhanced Raman scattering, which will be introduced in the following two subsections, may be used.

5.2 Raman spectra of soft modes

The scattering of acoustic phonons is measured by Brillouin scattering and that of optical phonons by Raman scattering. Within this work only the scattering of the optical phonons will be discussed. The Raman shifts $\nu - \nu_0$ due to the scattering by optical phonons are in the range of 10 cm^{-1} to 3000 cm^{-1}

As mentioned in section 5.1 Raman scattering induces a change in the electronic polarizability tensor α of the the system. The components of the this tensor per unit volume α_{mn} may be expanded in terms of generalized phonon wave normal coordinates *Q(q,t)* [67]:

$$\alpha_{mn} = \alpha_{mn}^{(0)} + \sum_j C_{mn}^j Q_j(q,t) + \sum_{ij} C_{mn}^{ij} Q_j(q,t) Q_i(q,t) + ... \tag{5.5}$$

$$= \alpha_{mn}^{(0)} + \alpha_{mn}^{(1)} + \alpha_{mn}^{(2)} + ... \tag{5.6}$$

with the coefficients $C_{mn}^j = \frac{\partial \alpha_{mn}}{\partial Q_j}$ and $C_{mn}^{ij} = \frac{\partial^2 \alpha_{mn}}{\partial Q_i \partial Q_j}$. The constant term $\alpha_{mn}^{(0)}$ here again gives rise to the Rayleigh scattering, the first order term $\alpha_{mn}^{(1)}$, which is linear in Q, to the first order Raman scattering where one phonon is involved, and the second order term $\alpha_{mn}^{(2)}$, which is quadratic in Q, to the second order Raman scattering involving two phonons. In the following only the first order scattering is discussed.

The spectrum *I($\omega_{s,j}$)* of the scattered light is obtained from the Fourier transformation of the far field solution of the inhomogeneous wave which describes the scattering of the incident field $\vec{E}_0$ on the dielectric inhomogeneity $\delta\varepsilon(\vec{r},t)$. Expanding the components of the dielectric constant tensor in terms of the normal coordinates Q_j

$$\varepsilon_{\alpha\beta} = \varepsilon_{\alpha\beta}(0) + \sum_j \left(\frac{\partial \varepsilon_{\alpha\beta}}{\partial Q_j} \right) Q_j \tag{5.7}$$

is leading to

$$I(\omega_{s,j}) = \frac{K^2}{2\pi} \int_{-\infty}^{\infty} e^{i\tilde{\omega}\tau} \langle Q_j(t+\tau) Q_j(t) \rangle d\tau \tag{5.8}$$

where $\tilde{\omega} = \omega - \omega_0$ is the frequency deviation from the frequency of incoming light ω_0. The first order Raman spectra thus reflects the spectral density of the autocorrelation function of the normal coordinates *Q_J(t)* of the various excitations. The spectral density of this autocorrelation

function can be related by the fluctuation-dissipation theorem to the imaginary part $\chi''(\omega)$ of the complex dynamic susceptibility $\chi(\omega)$ associated with this mode. For high temperatures ($\mathrm{k_B T} \gg \hbar\tilde{\omega}$) the integral from equation 5.8 ca be solved to

$$\frac{1}{2\pi}\int_{-\infty}^{\infty} e^{i\tilde{\omega}\tau}\langle Q_j(t+\tau)Q_j(t)\rangle d\tau = \frac{k_B T}{\pi\tilde{\omega}}\chi_j''(\tilde{\omega}) \tag{5.9}$$

leading to

$$I(\omega_{s,j}) = K^2\frac{k_B T}{\pi\tilde{\omega}}\chi_j''(\tilde{\omega}) \tag{5.10}$$

That means that the spectral distribution of the light scattered by a ferroelectric soft mode reflects the spectral distribution of the polarization fluctuations whereas the total integrated Raman intensity I_t estimates the time average polarization fluctuation $\langle \mathrm{P(t)}^2\rangle$. With the Kramers-Kronig relation it can be calculated to [67]:

$$I_t = \int_0^{\infty} I(\tilde{\omega})d\tilde{\omega} \propto \chi'(0) \propto \frac{1}{\tilde{\omega}^2} \tag{5.11}$$

5.3 Surface-enhanced Raman spectroscopy

Surface-enhanced Raman spectroscopy (SERS) was first demonstrated by Fleischmann [127] in 1974. A roughened silver surface leads to very intense Raman scattering from the adsorbate on this surface. The signal enhancement can be as high as 10^6.
In a SERS setup a laser is focused onto the rough sample but not the entire surface supports intense Raman scattering as showed by calculations from Shalaev and coworkers [128]. Only a few spots of certain geometries, the so called 'hot spots' provide an enhancement. Up to now the discussion about the best geometry for the enhancement is continuing, see for example [129–131] but surface roughnesses in the nanoscale range (10-100 nm) seem to provide the largest enhancements [132]. There are two different mechanisms which are invoked to influence the strong enhancement. The electromagnetic field enhancement and the charge transfer mechanism.
For the charge transfer mechanism an electronic interaction takes place between metal and adsorbate [133,134]. Therefore a sufficient orbital overlap is required which means that this effect is restricted to the outermost layer of surface atoms and adsorbate which is most efficient when the molecule is chemisorbed on the surface. The chemical enhancement factor ranges typically from 10 to 10^3 [131].
The electromagnetic field enhancement is caused by resonant excitation of localized surface plasmons. This can be achieved optically using lasers of certain wavelengths for nobel metal

particles of different shapes and sizes. On rough surfaces these plasmons are supported by protrusions and hollows. For a smooth metal surface the optical excitation is challenged by the phase matching condition between the radiation and the plasmons. The surface plasmon dispersion $\omega(k)$ is located outside the light cone $\omega = ck$ and therefore no excitation is possible. To realize an excitation the photon momentum or the wavevector have to be artificially increased by either increasing the refraction index of the incident medium or by engineering the metal surface, see section 5.5.
For aggregates of interacting particles, which are often structured as fractals, plasmon resonances can be excited in a very broad spectral range [135]. Due to this broad spectral range the incident field at the frequency ω and the scattered field at the frequency ω_s can both experience the enhancement. Thats leads to an enhancement factor which is given by the product of the enhancements of the two fields.

$$G \sim [|\frac{E_\omega}{E_\omega^0}|^2 |\frac{E_{\omega_s}}{E_{\omega_s}^0}|^2] \tag{5.12}$$

where E_ω and E_{ω_s} are the local enhanced fields at the frequencies ω and ω_s respectively and E_ω^0 and $E_{\omega_s}^0$ the non-enhanced fields at these frequencies. Setting both non-enhanced amplitudes equal to unity and regarding the case for a broader plasmon resonance width than the Stokes frequency shift the enhancement factor can be written as

$$G \sim [|E|^4] \tag{5.13}$$

because the two enhancements are fully correlated. This factor became known as the g^4 Raman enhancement factor. The value for the enhancement factor reaches 10^{10} or even 10^{12} for optimal conditions [131]. Metal substrates as silver, gold or copper are used because the resonance of their local surface plasmon oscillation lies in the visible range [136]. Therefore, under optimal conditions when both the electromagnetic and the chemical mechanism contribute, the SERS enhancement can be as high as 10^{15}.

Applications for nanoelectronics typically involve atomically flat surfaces that are not necessarily noble metals but semiconductors or even insulators. SERS is therefore inappropriate for use with these systems but scanning probe microscopy offers an elegant way to locally introduce a noble metal surface with arbitrary curvature: A coated tip.

5.4 Tip-enhanced Raman spectroscopy

With SERS the possibility for Raman measurements on small structures with a little amount of material is given through the large enhancements. But the required rough surface of the

substrate imposes a big constraint. To overcome this limitation an external roughness might be introduced by a SPM tip, the so called TERS. With the combination of a scanning probe microscope and a Raman spectrometer, it is possible to bring the scanning probe tip very close, about a few nm, above a smooth surface. The excitation laser is focussed on the very apex of the tip and then also localized surface plasmons are excited in the apex or in the gap between the tip and the sample (see Fig.5.2). Unless the tip is direct contact the enhancement only stems from the electromagnetic field enhancement as a charge transfer mechanism may not occur.

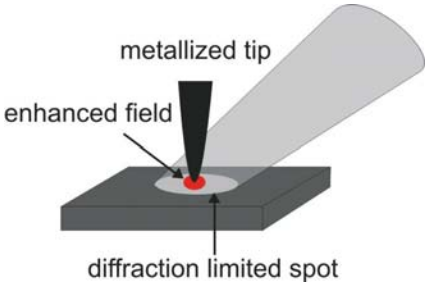

FIGURE 5.2: Principle of tip-enhanced Raman spectroscopy. The excitation of localized surface plasmons in the apex of the tip leads to an enhancement of the field underneath the tip, adapted from [137].

The enhanced electromagnetic field originates from a combination of an electrostatic lightning rod effect and surface plasmon resonances. The electrostatic lightning rod effect is a direct result of the geometric singularity of sharply pointed metal structures. The surface plasmon resonances depend on the excitation wavelength and tip material and geometry [138]. The enhancement only occurs for a longitudinal polarization of the incident light along the tip axis. The surface charge oscillates with the frequency of the exciting light. The free electrons are driven parallel to the direction of the polarization and thus parallel to the tip axis. The surface charge density is rotationally symmetric with the highest amplitude at the end of the tip. A standing wave with a shorter wavelength than the illuminating light is formed by the surface charges [138]. For a polarization perpendicular to the tip axis no charge accumulation takes place in the tip apex. The localized field in the vicinity of tip apex can be described by the field of an effective dipole $P(\omega)$, oscillating at the angular frequency ω and being located at the center of the tip apex with the magnitude [139].

$$p(\omega) = \begin{pmatrix} \alpha_\perp & 0 & 0 \\ 0 & \alpha_\perp & 0 \\ 0 & 0 & \alpha_\parallel \end{pmatrix} E_0(\omega) \tag{5.14}$$

with the z-axis chosen parallel to the tip axis and E_0 the exciting field without a tip. The perpendicular polarizability $\alpha_\perp$ can be described by a quasi-static polarizability of a small

sphere

$$\alpha_{\perp} = 4\pi\varepsilon_0 r_0^3 \frac{\varepsilon(\omega) - 1}{\varepsilon(\omega) + 2} \tag{5.15}$$

and the longitudinal polarizability is given by

$$\alpha_{\parallel} = 8\pi\varepsilon_0 r_0^3 f_e(\omega) \tag{5.16}$$

where ε_0 and ε are the dielectric constant of the tip and the surrounding dielectric, respectively, r_0 the tip radius and f_e the complex field enhancement factor. The electric field E at a given position of the tip relative to the exciting light r is now approximated as

$$E(r,\omega) = E_0(r,\omega) + \frac{\omega^2}{\varepsilon_0 c^2} G^0(r, r_0, \omega) p(\omega) \tag{5.17}$$

with r_0 specifying the origin of p and G^0 the free space dyadic Green's function. The possible enhancements are in the range of 10^6 up to 10^8. The gap is acting as a cavity for the correct distance in combination with the right laser wavelength and tip coating.
As TERS is used for the investigation of nanostructures the resolution of the method is of great interest, the vertical resolution and the tip-sample distance as well as the lateral resolution.
For the lateral resolution a lot of different theories exist. Just like in the AFM or in the PFM measurements the tip shape and dimension plays an important role for the lateral resolution. Wessel [140] stated a lateral resolution of $0.4 \times r_{tip}$ leading to a 8 nm resolution with a tip radius of 20 nm and a tip sample distance of 1 nm. Pettinger et al. [141] stated the lateral resolution to be half of the tip radius by estimating that the lateral extension of the near-field can be obtained according to the well-known $1/R^3$ near-field distance dependence (oscillating dipole in the tip apex regarded as sphere), leading to a $1/R^{10}$ distance dependence for TERS. The radius is defined as the drop of the field intensity to $1/e$. Also finite element analysis was done for the estimation of the lateral resolution. Downes et al. [142] made these calculations for various tip radii as shown in Fig.5.3. Their calculations achieve even atomic resolution for tips with a radius of 1 nm. Generally they estimate the resolution to be 3/4 of the tip radius but assumed the full width half maximum (FWHM) method which leads to a larger radius. In the case of a perfect gaussian profile these two radii are equal to each other. So in general the estimated lateral resolution differs from 0.4 to 0.75 of the tip radius, but it is for sure smaller than the tip radius. The application of a continuous model for the dielectric function at these dimensions is under strong debate.
Just as for the lateral resolution for the influence of the tip-sample distance on the Raman intensity various calculations were done by Festy et al. [143], Brown et al. [144], Nothinger

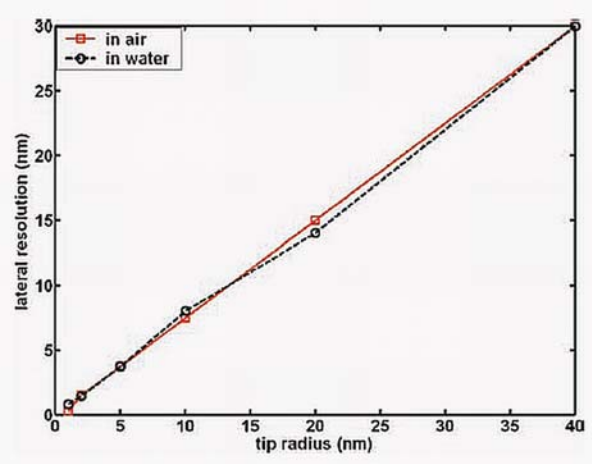

FIGURE 5.3: Lateral resolution as a function of the tip radius for gold tips with a tip as close as possible to the image plane, adapted from [142].

et al. [145] using an ellipsoidal tip shape and Pettinger et al. [141] using a spherical tip shape. Their results vary obviously as can be seen in Fig. 5.4. Especially, the calculations from Brown [144], who uses a 2D approach for the tip, in contrast to the others who use a 3D approach. Due to the spherical curvature of the tip, and especially the strong local concentration of the surface charges at the apex of the tip the assumptions from Pettinger [141] seem most appropriate. With these assumptions the decrease of the field between the tip and the substrate can be described by $\sqrt{2dr_{sp}}$, where d is the distance from the sphere and r_{sp} the radius of the sphere [147]. Here again the distance dependence of the electromagnetic field enhancement is given by the R^{-3} dependence with R the distance between the sphere (tip) and the place of enhancement. Using a metal substrate the introduction of a mirror dipole is necessary, which leads again to the g^4 Raman enhancement factor for the intensity with the same assumptions as in the case of the surface enhanced case. Regarding the tip sample distance of 1 nm as reference, integrating and normalizing the Raman intensity for this setpoint it can be written in the dependence of the distance z as

$$I_{2D}^{TERS}(z \geq d) = (r_{sp} + d)^{10}(r_{sp} + z)^{-10} \tag{5.18}$$

Here the strong z-dependence of the enhancement which can already be seen in Fig. 5.4 is quantified to a z^{-10} dependence. Up to now the TERS is realized with STM and AFM tips in air and STM tips in ultra-high vacuum. In this work a setup in reflection geometry using an AFM is used, which is introduced in details in section 6.3 and 6.4.
As the enhancement only takes place in the direct environment of the tip, within a region smaller

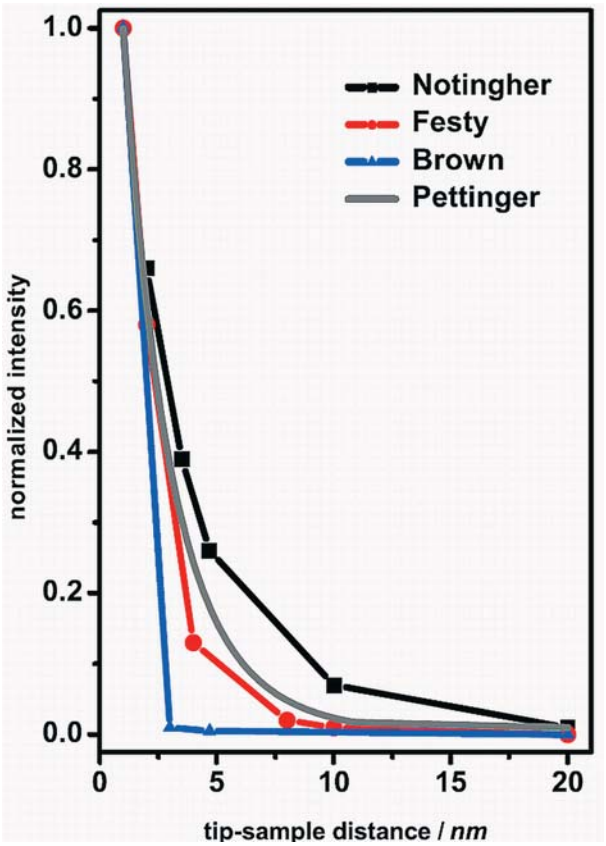

FIGURE 5.4: The normalized intensity in dependence of the tip sample distance shows different curves for the different theories, values taken from [146].

than the tip radius while a Raman background or signal is collected from the total laser spot area in a confocal setup it is necessary to create a focus as small as possible to be able to discriminate the enhanced signal against a confocal background. For example if an enhancement takes place in an area with a radius of 20 nm the total area is $A_1 = \pi(20\text{ nm})^2 \approx 1257\text{ nm}^2$ and the focus has a radius of 5 μm leading to an illuminated area of A_2=78539816 nm^2 an enhancement of $A_1/A_2 \approx 6 \times 10^5$ is necessary to achieve the same amount of scattered photons out of both regions.

5.5 Localized surface plasmons

Metals are defined by their quasi-free electrons in the ground state, which are not bound to single atoms but to the bulk. These free electrons are responsible for the well-known properties of high electric conductivity and optical reflectivity. They behave like a gas of free charge carriers, a so called plasma, and can be excited to plasma waves. These waves are longitudinal electromagnetic charge density waves and their quanta are called plasmons. There are two different kinds of plasmons, the bulk plasmons in the volume and the surface plasmons which are bound to the interface of a metal or dielectric. Both can not couple directly to light in adjacent dielectrics. For most metals the surface plasmon frequency is in the UV range, depending on the dielectric function of the metal and the surrounding dielectric. For Raman spectroscopy the nobel metals with surface plasmon frequencies in the visible range are of great interest.
In the non-retarded limit the dielectric function $\varepsilon(\omega)$ is given by:

$$\varepsilon(\omega) = -1 \tag{5.19}$$

This equation determines the frequency of the surface plasmon ω_s in this limit. With the Drude model

$$\varepsilon(\omega) = 1 - \frac{\omega_p^2}{\omega^2} \tag{5.20}$$

where

$$\omega_p = \sqrt{\frac{Ne^2}{m_e \varepsilon_0}} \tag{5.21}$$

is the bulk plasmon frequency, N the conduction electron density, e and m the electron charge and mass and ε_0 the permittivity of the free space. Then the surface plasmon frequency is obtained to

$$\omega_s = \frac{\omega_p}{\sqrt{2}} \tag{5.22}$$

For the excitation of surface plasmons in a planar metal surface by incident laser light energy and momentum conservation has to be fulfilled. Therefore the incident wave vector parallel to the surface $k_\parallel$ has to equal the transmitted wave vector parallel to the surface $k_{t\parallel}$. $k_\parallel$ is given by

$$k_\parallel = \frac{\hbar\omega}{c}\sqrt{\varepsilon}_1 sin\theta_i \tag{5.23}$$

with c the speed of light and θ_i the angle of the incident light and ε_1 ($\varepsilon_1 = 1$ in air) the dielectric constant of the medium above the metal surface.The transmitted wave vector is given by

$$k_{t\|} = \frac{\hbar\omega}{c}\sqrt{\varepsilon_2(\omega)}sin\theta_t \tag{5.24}$$

with θ_t the angle of the transmitted light. A propagation is only possible for $\varepsilon_2(\omega) > 0$ which is not given for frequencies below the plasma frequency in the metal, see equation 5.20. Therefore in this case only a propagation along the crystal surface is possible, the so called surface plasmons. Their wave vector can be obtained out of Maxwell's equations to [132]:

$$k_{sp} = \frac{\hbar\omega}{c}\sqrt{\frac{\varepsilon_1\varepsilon_2}{\varepsilon_1 + \varepsilon_2}} \tag{5.25}$$

This wave vector k_{sp} is always larger than $k_{\|}$ and so they can also not match and the surface plasmons cannot be excited by light or be transformed into light at a flat interface between two media.
One chance to enable the excitation of this surface plasmons is to elongate the wave vector of the incident light by the use of a prism with a refractive index $n > \varepsilon_1$. Therefore two approaches, the so called Otto configuration [148], with a gap in the order of the wavelength between the prism and the metal and the Kretschmann configuration [149] where the prism is located directly at the surface are used. Here for a given wavelength and given dielectric functions ε_1, ε_2 and ε_{prism} at exact one angle of incidence the surface plasmons can be excited. Figure 5.5 shows the case for a planar surface and air with no excitation and the case for the use of a prism with one intersection of the two dispersion curves.
Another possibility to support an efficient coupling between the photons of the incident light and the surface plasmons is to provide the missing momentum by introducing a surface roughness. The excitation of surface plasmons can take place on curved and closed surfaces. In this case the surface plasmons are called localized and their dispersion relation depends strongly on the surface geometry [151], see section 5.3. In the non-retarded limit the localized surface plasmon modes of a sphere are given by the relation

$$\varepsilon_2(\omega) = -\varepsilon_1\frac{l+1}{l}, l = 1, 2, 3, ... \tag{5.26}$$

The modes denoted by l are radiative and can be excited by light or transferred into light. The frequency of the lowest mode ($l = 1$) obeys

$$\varepsilon_2(\omega) = -2\varepsilon_1 \tag{5.27}$$

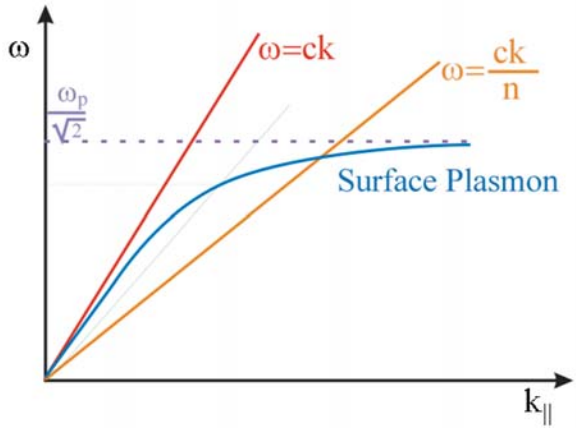

FIGURE 5.5: Surface Plasmon dispersion curve at an air-metal-glass interface with and without the use of a prism for the elongation of the wave vector, adapted from [150].

Regarding a small sphere with a radius much smaller than the wavelength is leading to a uniform field inside the sphere [152]. Taking the boundary conditions for the normal and tangential components at the surface of the sphere into account, and the complex quantity of the dielectric function $\varepsilon_2 = \varepsilon_2' + i\varepsilon_2''$, a maximum enhancement of factor at the resonance $\varepsilon_2'(\omega) = -2\varepsilon_1$ is given by:

$$g_{max} = \left|\frac{E_{ex}}{E_i}\right|^2 = \left(\frac{3\varepsilon_2'}{\varepsilon_2''}\right)^2 \tag{5.28}$$

For a spheroid with the electric field at the apex of its major axis oriented parallel to the electric field of the light, with the axes a and b much smaller than the wavelength and and a depolarization factor A, the resonance condition changes into:

$$\varepsilon_2'(\omega) = 1 - \frac{1}{A} \tag{5.29}$$

The enhancement at resonance is given by:

$$g_{max} = \left|\frac{E_{tip}}{E_i}\right|^2 = \left(\frac{\varepsilon_2'}{\varepsilon_2'' A}\right)^2 \tag{5.30}$$

Inserting the depolarization factor for a sphere $A = 1/3$ in the equation leads to the same result as equation 5.28. In the case of an ellipsoid the factor A gets smaller the more the ellipsoid is elongated resulting in a greater enhancement factor.

For the tip-enhanced Raman spectroscopy this means, the more elongated the tip apex, the higher is the enhancement. For AFM tips coated with an ensemble of differently large and shaped nobel metal nanoparticles, a resonant transfer of electric field energy will occur to the very particle that matches the dispersion condition best, even if it is not the particle which is the closest to the sample surface. This still imposes a major problem for the fabrication of AFM tips as compared to STM tips where only the tip apex of a homogeneous wire contributes.

6 Raman spectroscopy: Results and discussion

In the frame of this work two units for TERS are developed and built up. One is used for measurements in air and the other setup for ultra-high vacuum (UHV) measurements. In both setups atomic force microscopes and confocal optics are used to enable the investigation of non-conductive and opaque samples. Both setups operate with the same Raman spectrometer and laser sources.
The Raman spectrometer is a T64000 from Horiba Jobin Yvon with a triple spectrometer. A nitrogen cooled CCD array is used as detector. Using the high-resolution triple additive configuration Raman shifts in the order of 0.1 cm^{-1} can be observed. In the double subtractive setup it is possible to obtain spectral information up to 4 cm^{-1} away from the laser line. That means, with this setup it is possible to measure the ferroelectric soft-modes, which are in the range of 20 to 100 cm^{-1}. The scattered light from the sample is guided to the Raman spectrometer by a multi-mode optic fiber.
As lasers an Ar^+ ion laser at a wavelength of $\lambda = 488$ nm and a He-Ne laser with $\lambda = 632.8$ nm are used. The different wavelengths are necessary due to the different resonance frequencies of the localized surface plasmons of the gold (632.8 nm) and silver (488 nm) coated tips for the tip-enhancement. The Ar^+ ion laser is guided by single-mode fibers to the two different measurement points to provide a spacial frequency filtering and thus to preserve the TEM00 Gaussian beam profile of the laser. With this setup a power of up to 100 mW can be provided to the optics for the illumination and collection of the scattered light from the sample. The He-Ne laser provides a power of 5 mW and is fixed directly to the needed optics without need for fiber coupling. The use of optical fibers for the Ar^+ ion laser became mandatory due to the mechanical vibrations of the water cooling system that interfere with the resolution of the scanning probe microscope unless they are sufficiently wide apart.
This chapter will first focus on the preparation of nobel metal coated tips due to the fact that a reproducible preparation of an applicable coating is one of the biggest challenges in tip-enhanced Raman spectroscopy. Secondly the specific requirements of the optical setups for reflective configurations in both air and especially UHV are presented. The system requirements for the AFM in combination with the optical system is discussed as well in air as in UHV. In the UHV some new solutions for the combination have to be found due to the fact that the other systems realized in UHV, are using STM systems instead of AFM systems (for example standard optical systems are not UHV compatible and internal damping systems of the AFM will influence the measurements). In this parts the tip-enhanced Raman measurements under ambient conditions and confocal Raman measurements in UHV showing the applicability of teh system for TERS measurements are shown.

6.1 Tip coating

The tip preparation is one of the biggest challenges and problems in making tip-enhanced Raman spectroscopy a standard measuring tool due to the reproducibility of an applicable coating. The tip needs to be coated by metallic nano-cluster, not smooth dense films and one clusters with excellent dispersion matching has to be located at the very end of the tip. So even with

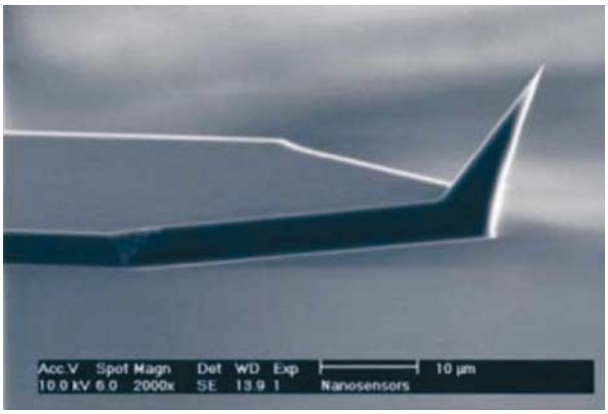

FIGURE 6.1: SEM image of an ATEC AFM cantilever with the tip at the end of the cantilever adapted from [153]

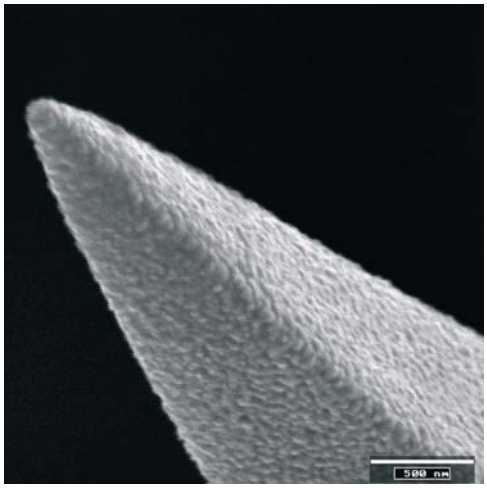

FIGURE 6.2: SEM image of a gold coated ATEC AFM cantilever. The desired clustered structure is visible after a sputtering time of 120 s under argon atmosphere

the correct deposition parameters for the necessary coating structure it is not assured that tip-enhancement occurs with every single tip.
The AFM-tips used in this work are the so called ATEC cantilevers from nanosensors either as contact or non-contact cantilevers. As can be seen in Fig. 6.1 the tip is positioned at the very end of the cantilever and pointing outwards. That permits optical access to the tip and a very exact positioning of the tip. Conventional cantilevers only permit optical access to the tip in a transmission configuration (transparent substrate) and will always cast a shadow on the tip as the beam points from above. The gold and silver is deposited in different ways on the cantilever. While the gold is deposited by sputtering the silver clusters are evaporated on the

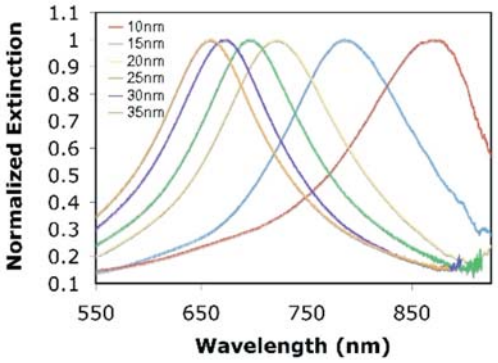

FIGURE 6.3: Localized surface plasmon resonance as a function of the wavelength for different sizes of gold nanoparticles, adapted from [154].

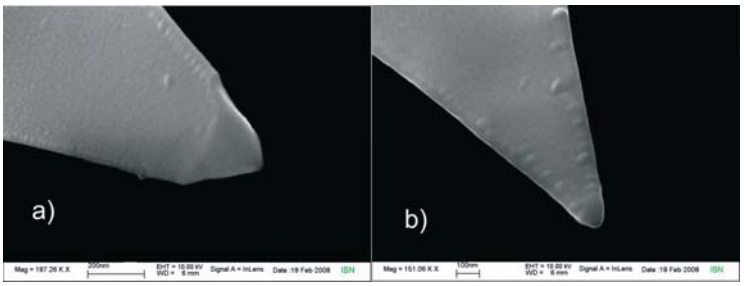

FIGURE 6.4: SEM micrographs of silver coated tips with an evaporated film thickness of a) 5 nm and b) 10 nm. The coatings are not providing the needed roughness.

cantilever.
The gold coating of the ATEC cantilevers is done by sputtering with the table-top sputter tool Scancoat 6. The sputter time is set to 120 s, leading to a film thickness of about 20 nm. The sputtering is done under argon atmosphere with a pressure of 3×10^{-1} mbar. With some of the coated cantilevers SEM micrographs are done to see if the structure of the sputtered gold provides the possibility for the tip-enhancement. This is not a sufficient condition for TERS and cannot be done with all cantilevers. After taking SEM micrographs of the tips they are not usable for tip-enhancement anymore due to a contamination with residual carbon from the SEM chamber. The same problem occurs for the silver coated cantilevers. Therefore most of the SEM measurements are done after the tip-enhanced Raman experiments. Figure 6.2 shows a SEM image of a gold coated cantilever, sputtered with the above mentioned settings. The gold coating shows the necessary cluster structure with a cluster size in the range of a few tens of nanometers which fits in the range of 10-100 nm for the maximum enhancement as introduced in section 5.3. The remaining problem is the location of a cluster at the end of the tip apex, which cannot be seen here, but this might be due to the tip-enhanced Raman experiments made in advance. For the gold coated tips the He-Ne laser with the wavelength of $\lambda = 632.8$ nm is

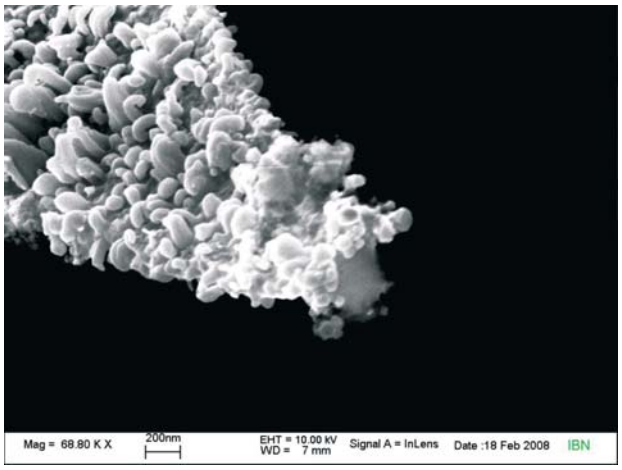

FIGURE 6.5: SEM micrographs of a used silver coated tip with an evaporated film thickness of 20 nm with a damaged tip apex.

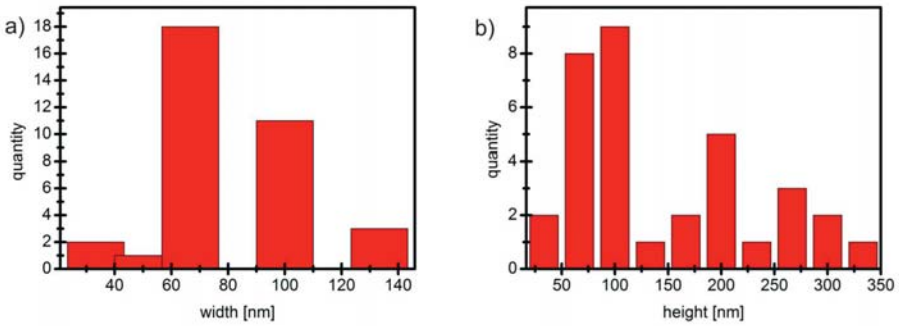

FIGURE 6.6: Width a) and height b) distribution of the silver nanoparticles at the AFM-tip.

used due to the resonance wavelength of localized surface plasmons shown in Fig. 6.3.
For the silver deposition the available sputter tool is not applicable. The silver might oxidize during the sputtering because the initial vacuum before inserting the process gas is not good enough for an adequate removal of the oxygen. The silver deposition is done by vaporization in an UHV-chamber at a pressure of 1×10^{-7} mbar. A coating thickness of 20 nm with an evaporation rate of 0.03-0.05 nm/s is favorable for the desired coating structure [155]. Due to differences in the evaporation itself and the evaporation systems as well as different used cantilevers also thinner coatings of 5 and 10 nm are produced and tested. But for the thin films the surface roughness was too low, as shown in Fig. 6.4 especially at the tip apex. The tip coated with 20 nm silver shows again cluster growth with a columnar structure which is also preferable for the tip-enhancement. As discussed before, used tips are taken for the SEM micrographs as can clearly be seen in Fig. 6.5 by means of the deformation of the tip apex.

The obtained clusters have a width distribution below 140 nm centered around 70 nm, see Fig. 6.6*a)*. The height distribution shows higher values as can be seen in Fig. 6.6*b)* centered arround 100 nm and below 350 nm, leading to the preferred ellipsoidal shape. The best case for the tip-enhancement would be a cluster growth parallel to the tip axis at the very end of the tip which can not be seen here anymore due to the damaged tip. But tip-enhancement may still occur with one of the clusters at the end of the damaged tip. For the silver coated tips the resonance is shifted to higher frequencies, respectively smaller wavelengths, and therefore the Ar^+ ion laser with a wavelength of $\lambda = 488$ nm is used. In spite of the good quality of the silver and gold coatings, only a few of the so fabricated cantilevers show tip-enhancement. The amount of the fabricated cantilevers working successfully is about 10% as also experimentally observed by other groups [155].

The operation of a tip-enhanced Raman microscope in air unintentionally constitutes optical tweezers: Any dielectric on the surface will move along the electric field gradient which directly leads it to the tip apex which will rapidly experience severe contaminations mainly of carbon oxides. These background signals interfere with the sample signature and can be avoided by measurements in UHV.

6.2 T64000 and SERS measurements

The T64000 Raman spectrometer is equipped with a confocal microscope that allows measurements with a diffraction-limited resolution of about 1 μm. The short working distance of the microscope objective comes along with a high numerical aperture and a high photon collection efficiency. We used this microscope to calibrate our TERS confocal setups where the numerical aperture had to be sacrificed for the sake of optical access to the sample.

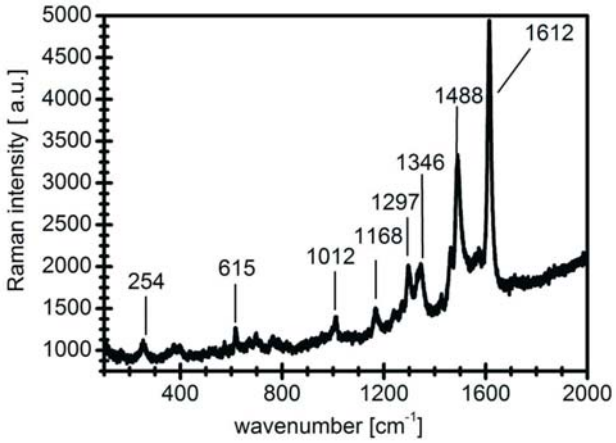

FIGURE 6.7: Confocal Raman measurement at the T64000 of a Rose Bengal dried droplet

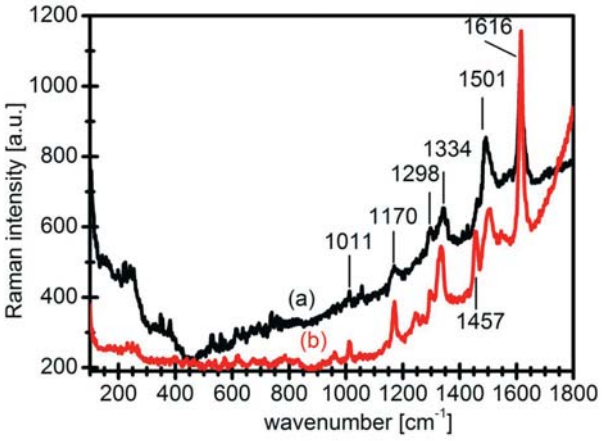

FIGURE 6.8: Confocal Raman measurement (a) and SERS measurement (b) of a Rose Bengal solution

To be able to compare the results of the two new setups with the confocal measurements at the T64000 spectrometer itself the used sample is chosen to provide a high Raman intensity and the possibility for the use in UHV. Therefore Rose Bengal dye as a dried droplet on a glass substrate is used. For the measurements with the built-in microscope at the spectrometer the Ar^+ ion laser is used with a power of 1.8 mW (see Fig. 6.7).
Additionally a solution of Rose Bengal is measured in this setup (Fig. 6.8*a)*) and a SERS measurement (Fig. 6.8*b)*) is carried out. Here the enhancement factor is 1.5 and the background signal is much lower leading to clearer peaks.

6.3 Concept of the experimental TERS setup in air

For TERS the atomic force microscope has to provide a stable optical access to the tip. The CP 2 from Veeco is chosen as it is already prepared for direct optical access with along working distance microscope objective for sample and tip alignment. It therefore offers the possibility to illuminate the AFM-tip with a standard long distance microscope objective, as can be seen in Fig. 6.9. Furthermore this AFM is a sample scanner, which means that the tip stays constant during scanning and the optical alignment is not disturbed. Once the tip is approached to the sample and the laser is focused on the tip the alignment is fixed.

The optics are built up in a confocal setup with a beam splitter cube, two microscope objectives and a beam expansion. The beam expansion is the only difference within the optics for the two laser sources. The Ar^+ ion laser is collimated with a fiber-collimator to a beam diameter of 8 mm and the He-Ne laser to a diameter of 9 mm for a homogeneous illumination of the microscope objective. For the helium-neon laser a pinhole is inserted for *k*-vector filtering. This is not necessary for the other laser because the single-mode optic fiber already is a perfect *k*-vector filter. The collimated beam is guided through a laser line filter with a transmission curve

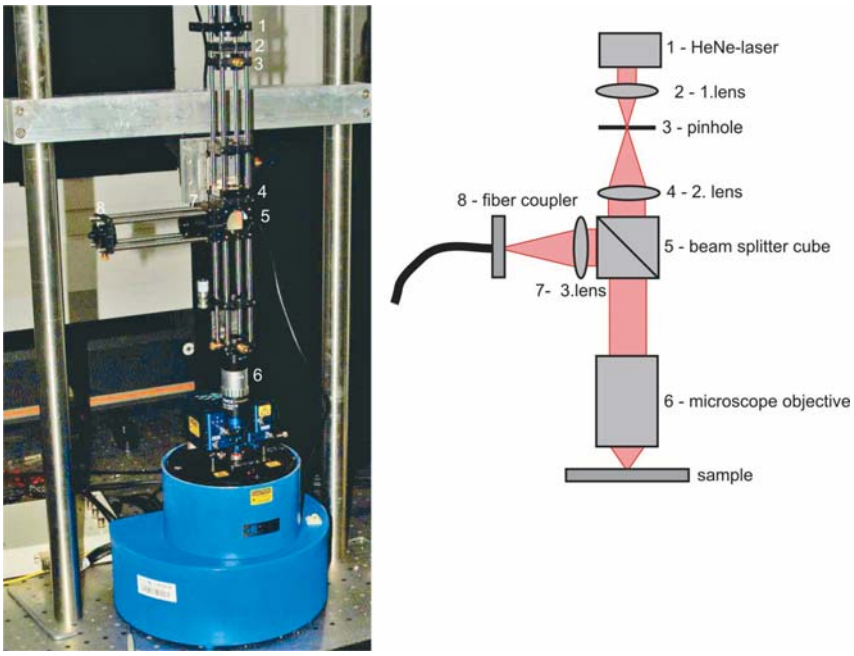

FIGURE 6.9: CP2 with the focusing optics and a sketch of the confocal optical path for the use of the helium-neon laser

of 1 nm FWHM width at the wavelength of the laser to filter out every other wavelength like for example the plasma oscillation of the Ar^+ ion laser or the background of the single-mode optic fiber, as discussed in section 6.3.1. Afterwards the laser beam passes the beam splitter cube which has a transmission of only 25% and a reflectivity of 75% and is then focused by the microscope objective. The low transmission and high reflectivity of the beam splitter cube is chosen for two reasons. First as much scattered photons as possible should be collected and guided to the multi-mode optical fiber and second the intensity of the laser in the very small spot is kept small to prevent heating or even a damage of the sample in the spot. For the collection of a high amount of the scattered photons the microscope objective is selected to enable the biggest solid angle at the needed working distance. This possible solid angle is given by the numerical aperture NA of the objective by $NA = n\sin(\theta)$ where n is the refractive index and θ the half solid angle. For the CP2 a working distance of $d = 33.5$ mm is necessary leading to a numerical aperture of $NA = 0.28$. The scattered photons are then focused by the second microscope objective to an x,y movable fiber coupler and guided by the multi-mode optic fiber to the Raman spectrometer.
The main characteristics of the beam, the beam width, the beam intensity profiles and shape and the power are determined with a BeamMaster system from Coherent in the focus of the laser spot by scanning multiple knife-edges across the beam and capturing the intensity distribution of the laser [156]. The results for the 488 nm laser are shown in Fig. 6.10. In parts *a*) and *b*) of Fig. 6.10 the two perpendicular beam profiles in the focus of the laser beam are shown

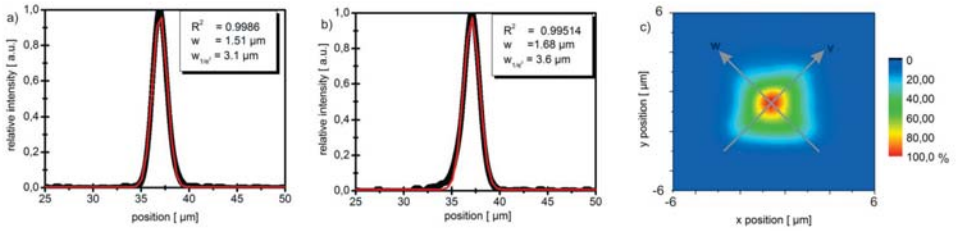

FIGURE 6.10: Characteristics of the beam in the focus spot. Parts a) and b) show the profiles for two perpendicular cross-sections as can be seen in part c) which also shows the projection of the laser beam of the Ar^+ ion laser ($\lambda = 488$ nm).

including a Gaussian fit and the Gaussian correlation R^2 of the real beam. The projection of the beam in the focus is shown in part *c*), including the two cross-sections of the profiles shown in parts *a*) and *b*). For an ideal TEM00 single mode laser this correlation would be 1, a perfect Gaussian beam [157]. The experimental determined values of R^2=0.9986 and R^2=0.9951 indicate excellent beam quality. For optical calculations the spot size at $1/e^2 \approx 13.5\%$ of the intensity not the FWHM value is relevant, leading to a spot size of 3.1 μm respectively 3.6 μm for the two different profiles. The power of the laser is $P = 9.388$ mW.
The resolution of a microscope objective and therefore the theoretical minimal realizable focus size is given by:

$$w = 1.22\frac{\lambda}{NA} \tag{6.1}$$

With the used objective and its numerical aperture of $NA = 0.28$ a minimal focus size of $w = 2.2$ μm is possible. The difference to the achieved focus can be explained by the inhomogeneous illumination of the free aperture of the microscope objective. As discussed in section 5.4 the polarization of the incident light plays an important role for the enhancement at the tip. Therefore polarization maintaining single-mode optic fibers are used to guide the Ar^+ ion laser to the two measurement points. To check the correct installation of these fibers the polarization of the incident laser is measured with a polarimeter from Schäfter und Kirchhoff at the end of the fiber . The He-Ne laser is also polarized but installed directly in front of the optics with a marker for the direction of polarization, so that it is not necessary to control it. The polarimeter measures the direction of the polarization by collimating the beam on a rotating polarizator and afterwards on a photodiode [158]. The photocurrent in combination with the time and position signals allows the determination of the polarization direction and the total amount of polarized light. Figure 6.11 shows a typically measurement. The extinction is a value for the degree of polarization and the sinusoidal modulated photocurrent on the right side is due to the rotational polarizator. The maximum values are an indication of the incoming power and the minima for the quality of the polarization. In the case of a parallel orientation of the polarizator and the polarization a maximum intensity is passing and when they are aligned perpendicular to each other, the less light is passing the better the degree of polarization is. As can be seen by the nearly line-shaped plot in the middle of the picture the laser is highly polrarized. For a worse

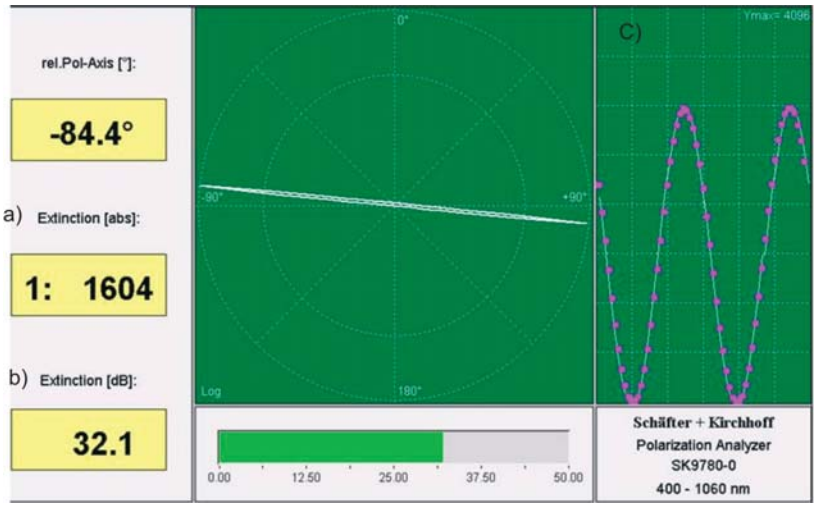

FIGURE 6.11: Polarization measurement showing the absolute and dB extinction values (a), a plot of the axis of polarization (b) and the intensity plot (c)

degree of polarization the plot would get an ellipsoidal shape.
For the He-Ne laser a focus spot of 3.3 μm respectively 3.6 μm with a Gaussian correlation above 91% is measured. The power is much lower with $P = 0.266$ mW (see Fig. 6.12).

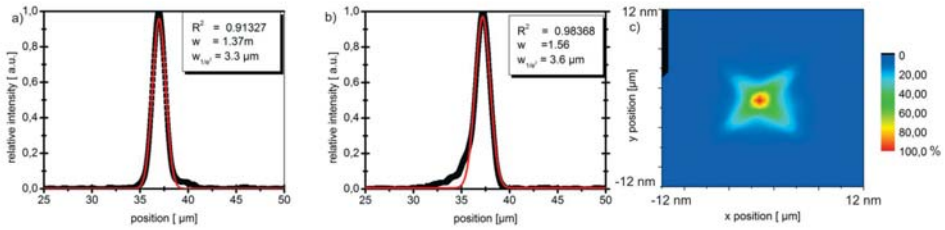

FIGURE 6.12: Plots of the cross-sections of of the laser beam at the wavelength of 632.8 nm (a), (b) and the projection (c) in the focus of the beam

Due to the small cross-section of Raman spectroscopy the amount of the scattered photons which are collected by the optics is very important. The Raman scattering is initially assumed to be isotropic and due to the opaque substrate, the solid angle can be regarded as a half sphere. The optics can only collect the scattered photons out of a part of the solid angle, determined by the NA. So the photons reaching the Raman spectrometer can be calculated by the fraction of the solid angle and the losses of the optics leading to a number of

$$\sharp = \overbrace{0.036}^{solid\,angle} \cdot \underbrace{0.96}_{microscope\,objective} \cdot \overbrace{0.75}^{beam\,splitter} \cdot \underbrace{0.96}_{microscope\,objective} \cdot \overbrace{0.8}^{fiber\,coupler} = 0.0199 \quad (6.2)$$

per scattered photon. This value of 2% is valid for both laser sources. The Raman measurements carried out with this setup are shown in the next section.

6.3.1 Raman measurements

First, the single- and multi-mode optic fibers are investigated if they create their own specific Raman signature. Therefore a mirror is placed at the position of the sample. First the multi-mode optic fiber is checked with the He-Ne laser and the laser line filter for $\lambda = 632.8$ nm directly after the laser source and no Raman spectra could be obtained. This might be due to the low power of the laser light guided by the multi-mode optic fiber. Afterwards the Ar^+ ion laser with the single-mode optic fiber is used. Without a filter a Raman signature of the single-mode optic fiber is detectable (see Fig.6.13). This background cannot be completely eliminated with the laser line filter behind the single-mode optic fiber as can be seen in Fig. 6.13. The measurements are carried out with an exposure time of $s = 30$ s and with an initial power of $P = 10$ mW at the place of the mirror. Adding the laser line filter, the power is reduced to $P = 6.5$ mW, due to the losses at the filter. The small background can further be reduced by misaligning the beam reflected from the fiber directly to the the multi-mode fiber by the beam splitter so that it is not coupled into the multi-mode fiber.

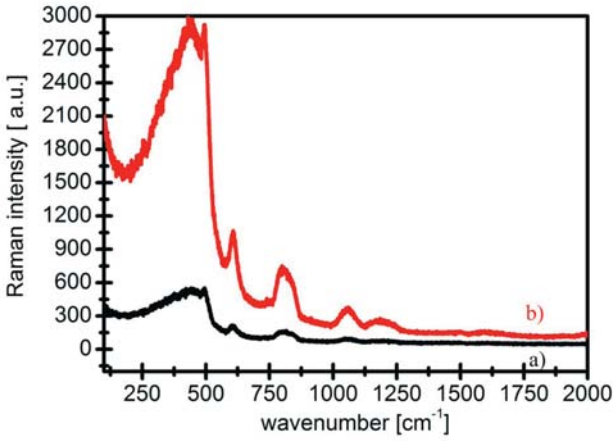

FIGURE 6.13: Raman spectra of the single-mode optic fiber with (a) and without (b) an inserted laser line filter behind the fiber .

With the optics aligned in the described way, first Raman measurements are carried out with the Rose Bengal dried droplet.
The He-Ne laser provides a power of $P = 0.6$ mW at the sample. To obtain a clear Raman spectrum an exposure time of $t = 120$ s is used (see Fig. 6.14*a*). To get comparable results, the time is kept constant for every other measurement and only the power of the laser is varied due to different laser sources and optics. Using a gold coated tip, as described in section 6.1

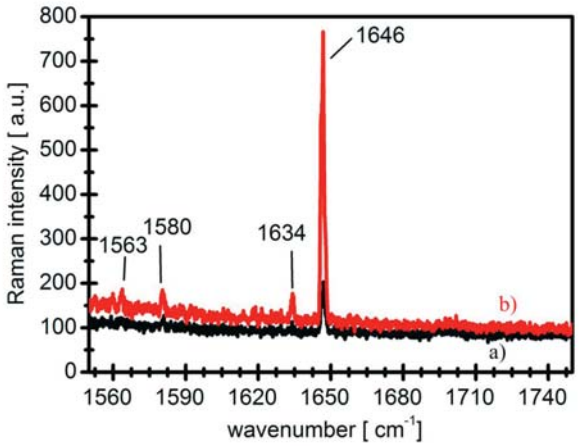

FIGURE 6.14: Confocal Raman (a) and TERS (b) measurements with a gold coated AFM-tip. The net enhancement factor is about 6 providing a conservatively estimated real enhancement of $2.6\times\ 10^4$

for 120 s, in the non-contact AFM mode for the tip-enhancement a clear enhancement of the Raman peak at 1646 cm^{-1} and additional peaks which could not be seen in confocal Raman at 1634 cm^{-1} ,1580 cm^{-1} and 1563 cm^{-1} are measured (see Fig. 6.14*b*). The enhancement at the main peak has a value of 6. In this enhancement the different amount of Rose Bengal due to the different areas contributing, is not considered. For the confocal Raman measurement with a focus size of at least 3.3 μm the illuminated area can be calculated to

$$A_R = \pi \left(\frac{d}{2}\right)^2 = 8.55\, mum^2 \tag{6.3}$$

The area of the tip-enhancement is defined by the tip-diameter of approximately 25 nm, leading to a value $A_{TERS} = 0.0019\ \mu m^2$. Dividing these two areas and multiplying this factor with the measured enhancement, a real enhancement factor of

$$\sim 2.6 \times 10^4 \tag{6.4}$$

is given. The enhancement is not as high as theoretically predicted but some improvements may still be achieved. In this setup the optics are not adjusted in the preferred angle of 55°, the angle where the dipole emission is strongest. Furthermore the optical path and tip axis are oriented parallel to each other preventing a polarization direction of the laser light parallel to the tip axis. In fact this is the least favorable condition for the relative alignment between polarization vector and the tip axis.

The Ar^+ ion laser provides a higher power which is adjusted to $P = 7.7$ mW at the sample. With this higher intensity more Raman bands become visible in the confocal measurement setup. In comparison to the measurements with the He-Ne laser the bands are shifted. The

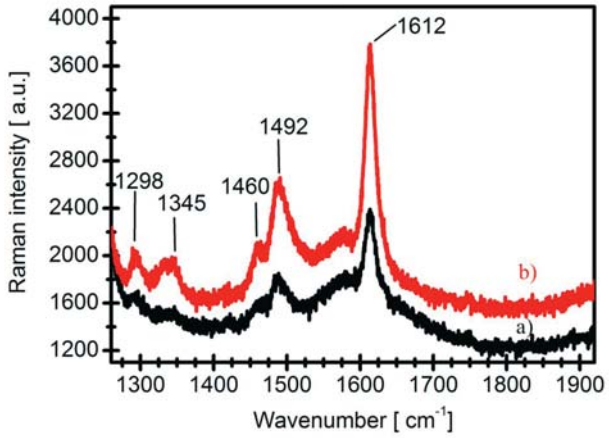

FIGURE 6.15: Confocal Raman (a) and TERS (b) measurements with a silver coated AFM-tip. The net enhancement factor is about 3 providing a conservatively estimated real enhancement of $1.3\times\ 10^4$

main band appears at 1612 cm^{-1} and the additional at 1492 cm^{-1}, and 1298 cm^{-1} (see Fig. 6.15*a*). For TERS the Ar^+ ion laser and the silver coated tips have to be used. The applied tip has an evaporated coating thickness of 20 nm. The tip-enhancement obtained with this setup is a little bit smaller than with the gold coated tip. An enhancement factor of 3 occurs for the band at 1612 cm^{-1} and a factor of 2 can be determined for the other two bands at 1492 cm^{-1} and 1298 cm^{-1} (see Fig. 6.15). Additionally, the bands at 1460 cm^{-1} and 1345 cm^{-1} occur. Since the change in the ratio between the two effective areas can be neglected due to the very small change in the focus radii, the real enhancement can be calculated again to $\sim 1.3 \times 10^4$ and $\sim 8.7 \times 10^3$, respectively.

These results indicate the feasibility of tip-enhanced Raman with low-end components and enhancement factors that are sufficiently large to discriminate the tip-enhanced local signature against the confocal background. As described above there is still some room for improvement with an adapted beam geometry. This might require modifications of the microscope as they are typically not optimized for optical access.

6.4 Conception of the ultra-high vacuum setup

Since TERS is an inherently a surface measurement technique where only the near field is contributing to the enhanced signal, it is desirable to work in well defined environment conditions on defined surfaces, especially for ambient sensitive samples. A lot of sample surfaces undergo a change in ambient conditions due to oxidation or accumulation of adsorbates, for example the perovskites discussed in the first part of this work. Another advantage is the reduction of

bleaching for example of dyes like Rose Bengal under oxygen free atmospheres. Therefore the TERS setup is transferred into the UHV. This transfer causes a lot of challenges. For an AFM in a UHV chamber the optical access is much more demanding and all commercial multi-lens systems are not UHV compatible. To meet these requirements a standard UHV AFM setup with an additional inverted view port (tube) is used (see Fig. 6.16). The tube is mounted in the preferential 55° orientation to the surface normal and is fixed to an external *x, y, z* movable stage enabling the adjustment of laser focus on the AFM-tip and sample. With this inverted view-tube it is possible to keep the optics in air. The transition between air and UHV is done by a fused silica optical plane window with a flatness of $\lambda/4$ and a parallelism of 3 arcseconds at the end of the inverted view-tube. As material of the window fused-silica is used instead of the normal sapphire windows due to the birefringence of the sapphire which would influence the optical path. In the inverted view-tube an additional tube containing the focussing optics is inserted to keep the optics as a unit which may be removed from the UHV chamber, for example during the out-baking of the system (see Fig. 6.17). Depending on the diameter of the tube different working distances are accessible and therefore different fractions of the solid angle detectable. The theoretically possible fraction of the solid angle is calculated by assuming a half sphere at the respective working distance as total solid angle and then dividing the area of the tube window by the total solid angle. Table 6.2 shows the possible combinations leading

working distance [mm]	tube diameter [mm]	fraction of solid angle
27.94	09.652	0.015
33.02	12.700	0.018
38.10	19.050	0.031
44.45	25.400	0.041

TABLE 6.2: Detectable fraction of the solid angle in dependence of the working distance and tube diameter

to a maximal fraction of the solid angle of 0.041 for a tube diameter of $d = 25.4$ mm with a working distance of $w_d = 44.5$ mm.

To ensure the stability of the optical alignment according to tip and sample, the AFM in the UHV chamber has no internal damping and is only damped by the table as the whole instrument and especially the optics. So oscillations or other disturbances will have no influence on the relative alignment. As described already for the air setup the laser beam is expanded and collimated, then guided through the laser line filter and the beam splitter cube and finally focused on the sample. The scattered light is eventually focused in a multi-mode optic fiber and guided to the Raman spectrometer. In contrast to the setup in air here the focusing is done by lenses instead of a microscope objective. The beam splitter cube has a transmission of 20 % and a reflectivity of 80 %. The optical path is sketched in Fig. 6.17. Here two additional

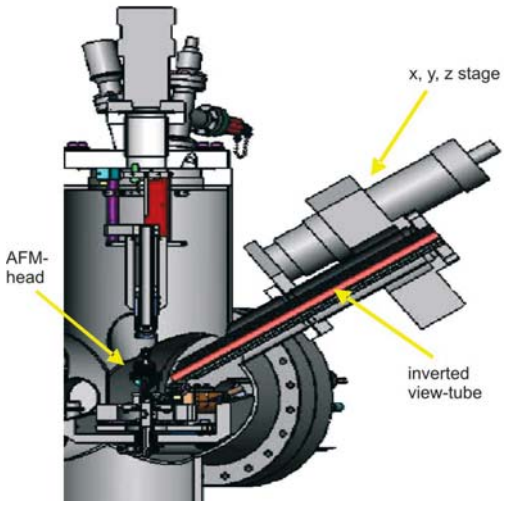

FIGURE 6.16: Sketch of the UHV AFM-chamber with the x, y, z-movable inverted-tube where the optics are placed in.

holders for filters for the incoming and outgoing beam are inserted (marked in green). The gray sketched tube is inserted in the inverted tube. The other optics are mounted outside.

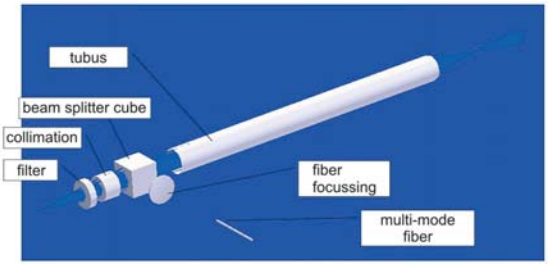

FIGURE 6.17: Sketch of the optics for the UHV-setup. The tubus will be inserted in the inverted-tube.

With this optical configuration a laser focus of about 4.3 μm is realized. The two profiles of the cross-sections in the focus show values of 4.1 and 4.5 μm respectively with a symmetric beam projection in the focus. With a maximum free aperture of 18 mm, due to the additional inserted tube, and a working distance of 44.5 mm the numerical apertur of the focussing unit is given by $NA = 0.18$, leading to a minimum possible focus of 3.8 μm. The detectable fraction of the solid angle calculated with the used optics is given by 0.017. The difference to the theoretical fraction of 0.041 is due to the smaller useable free aperture and the therefore maximal possible NA of the optics. In Fig. 6.19. the polarization measurement with a high degree of polarization

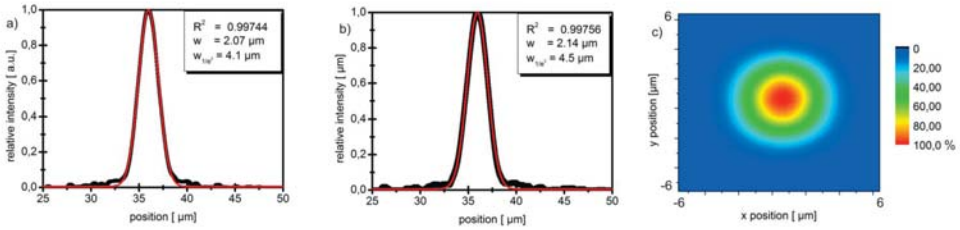

FIGURE 6.18: Laser beam profiles (a, b) of the projection (c) in the focus of the beam for the Ar^+ ion laser and the UHV-optics.

of the incoming laser beam is shown. The direction of polarization can be aligned in the plane perpendicular to the beam direction by rotating the fiber connector of the single-mode fiber, shown in Fig. 6.17, to ensure a net polarization perpendicular to the sample surface.

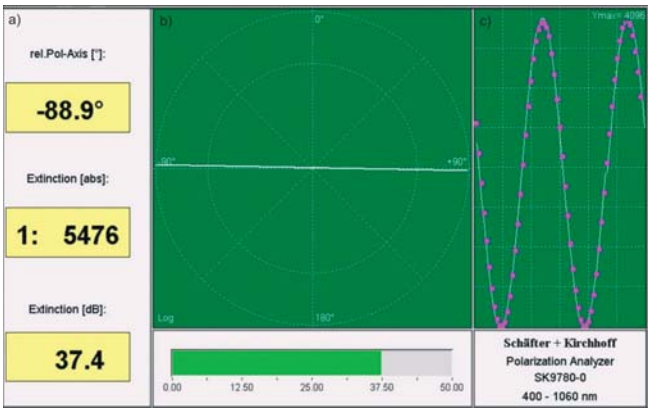

FIGURE 6.19: Polarisation of the Ar^+ ion laser beam in front of the UHV optics.

The amount of the detected photon per scattered photon for this setup can be calculated by:

$$\sharp = \overbrace{0.017}^{solid\,angle} \cdot \underbrace{0.92}_{window} \cdot \overbrace{0.99}^{1.focusing\,lens} \cdot \underbrace{0.99}_{2.focusing\,lens} \cdot \overbrace{0.80}^{beam\,splitter} \cdot \underbrace{0.99}_{lens} \cdot \overbrace{0.8}^{fiber\,coupler} = 0.0097(6.5)$$

This lower percentage of only 0.97 %, in comparison to the setup in air, is caused by the smaller detectable solid angle, due to the longer working distance and smaller numerical aperture of the focusing unit.

6.4.1 Confocal measurements in the UHV

Before starting TERS in UHV the specifically constructed optics have to be tested. Especially the restrictions of the working distance and aperture of the optics due to the UHV chamber and the window at the transition between the UHV and the atmosphere might influence the measurements.

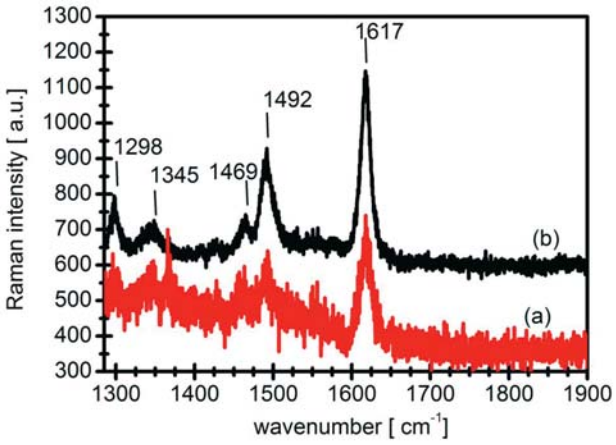

FIGURE 6.20: Raman spectra of Rose Bengal for an incidence angle of 35°, taken in ambient atmosphere outside the UHV chamber (a) and under UHV conditions (b). The difference in intensity is due to reflection losses at the uncoated window.

First tests to ensure that a sufficiently large Raman intensity is measured with the customized optics are done by confocal measurements on a Rose Bengal dried droplet in air. Therefore the optics are mounted with the same angle of incidence and distance as in the UHV to the sample and a Raman spectrum is taken with a laser power of $P = 1.5$ mW and an exposure time of $t = 120$ s. After obtaining an expected Raman spectrum (see Fig. 6.20*a*), the optics were inserted in the inverted view-tube and the measurements are repeated with the same sample and parameters. As can be seen in Fig. 6.20*b* the obtained intensity is about 15 % lower for the main peak at 1612 cm^{-1} due to the reflection losses at the window which are about 8 % per way (see also Equation 6.5). These reflection losses may be prevented by the use of an anti reflection coated window for the used wavelength at least at the side of the window under ambient conditions. Another reason may be a change in the working distance because the focus is adjusted again before measuring in the UHV.
Furthermore the estimation of the laser power in the UHV is more complicated. In air the power can be measured in the focus at the place of the sample by simply removing the sample.

In the UHV it is calculated by the percentage of the laser power behind the fiber connector of the single-mode fiber. At the laser line filter only 60 % of the light is transmitted, the beam splitter cube has a transmission of 20 % and the lenses and the window absorb or reflect another 10 %, leading to an overall transmission of 11 % of the incoming power to the sample. This calculation is confirmed by measuring the power after the single-mode optic fiber and at the location of the sample after the Raman measurements in air. The measurements provide $P = 13$ mW behind the optic fiber and $P = 1.5$ mW at the sample without the window at the transition to the UHV.

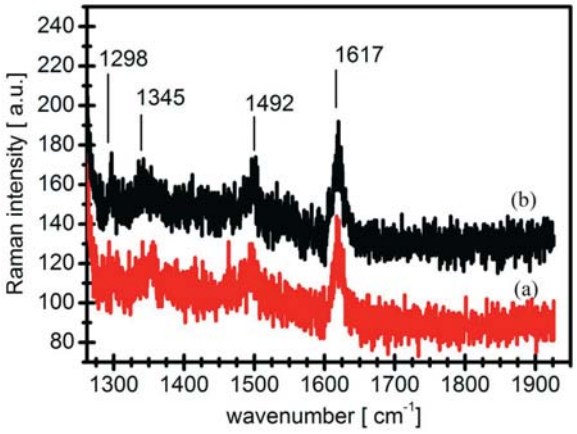

FIGURE 6.21: Raman spectra measured inside the UHV chamber under a) UHV conditions and b) a ventilated chamber under argon atmosphere with ambient pressure. The UHV window does not significantly bend under the mechanical stress induced by the pressure difference and remains optically passive i.e. without effect on the focal spot size.

As mentioned in the previous section the material of the window for the inverted view-tube is fused silica due to its optical passivity. But even for a fused silica window, where no birefringence occurs, the window may influence the optical path by bending due to the high pressure difference. This bending would act as an additional lens leading to a change in the focal length and therefore to a change in the Raman intensity if the distance to the sample stays constant. To prove this optical passivity the laser is focused on the sample and measurements are done with a laser power of $P = 2$ mW for $t = 120$ s once with an evacuated chamber at a pressure of 1×10^{-10} mbar and then repeated after the chamber was ventilated without changing the working distance. The two measurement show the same Raman intensities as can be seen in Fig. 6.21 excluding any influence due to the transition from air to the UHV.
The functionality of our silver and gold coatings and our ambient condition setup is proven by

tip-enhanced measurements in air. The UHV setup provides expected confocal Raman measurements and applicability of the chosen system. So with the before described setup, all necessary requirements are fulfilled to now combine tip-enhancement and UHV Raman to eventually demonstrate the full performance.

7 Summary

This work comprises two major parts, one devoted to electromechanical force microscopy that will be summarized first and a second one dealing with tip-enhanced Raman spectroscopy that will be summarized thereafter.

- **Piezoresponse Force Microscopy**
  Several different material systems were investigated by PFM providing insight into local structures of hollow $BaTiO_3$ particles and ferroelectric ordering in $NaNbO_3$. The geometrical constraints of the tip curvature to the imaging quality of PFM at the perimeter of ferroelectric nanoislands is shortly discussed.

- **Dynamic PFM**
  Exceeding the coercive field upon scanning within the piezoresponse force mode results in a loss of the domain imaging contrast. In exchange, it provides highly rewarding data on the nature of the electrical contact and its dynamics that are used to propose a novel detection scheme for ferroelectric domain reversal and a new method to estimate ferroelectricity in thin structures without a restriction due to the coercive field.

- **Adsorbate-induced phase shift in PFM experiments**
  Adsorbates are modeled by a voltage divider. This work incorporates them as part of the realistic AC-circuit. As a function of frequency, the domain-dependent RC-time constants contribute another, sometimes dominant, term to the existing theory of the phase difference.

- **Electromechanical Force microscopy**
  Polar and nonpolar surfaces can be imaged for local dielectric heterogeneities by a novel scanning probe microscopy technique at $2\,\omega$ that has been filed as a patent. The feasibility is demonstrated on misfit dislocations of relaxed $BaTiO_3$ on a $SrTiO_3$ (100) surface. The data are in excellent quantitative agreement with FEM simulations of the defect signature and independent studies of the dislocation density and ordering.

- **Tip-enhanced Raman microscopy**
  During this work two tip-enhanced Raman microscopes were set up, one for use under ambient conditions, another one for use in UHV. Both of them are designed for resonant excitation of gold and silver nanoparticles at the respective wavelengths. Successful operation under ambient conditions was demonstrated with a typical enhancement factor of $5{\cdot}10^4$. The system is characterized for UHV conditions in terms of beam diameter, numerical aperture, photon efficiency, and operation with the multichannel analyzer of the

Raman spectrometer. Confocal Raman measurements under UHV conditions confirmed the calculated photon efficiency.

8 Outlook

Piezoreponse force microscopy is spreading as a popular tool to investigate ferroelectrics. However, the level of understanding the imaging mechanism throughout literature is asking for more research to eliminate doubts, ambiguities and common artifacts. This research will comprise high-frequency PFM, PFM under UHV conditions, temperature-dependent PFM and other variations of external parameters such as illumination. In this sense PFM will soon become a standard technique in engineering departments but still offers a lot of scientific challenges for solid state physics.

The frequency-dependent PFM-measurements should be complemented by investigations of the surface conductivity and Nano-XPS examinations of domain-specific adsorbates. Such experiments have already been conducted, but with the only objective to qualitatively identify adsorbates with a domain-specific polarity. Now quantitative experiments become mandatory to determine the RC-time constants in the model.

Electromechanical force microscopy should and will be applied to nonpolar materials including industrially relevant semiconducting systems. The non-destructive scanning technique with a lateral resolution of a few nanometers is absolutely unrivalled. This non-destructive method only requires a contact-mode AFM and a lock in amplifier.

Tip-enhanced Raman spectroscopy is probably the most promising method to look into finite size effects in ferroelectric nanostructures as it does not rely on electrical contacts or other sources of artifacts. The Curie-Weiss-like condensation of the soft-mode phonon is a quantitative handle on the proximity of a phase transition. Using this for individual nanoparticles means to transfer a successful and well established technique for temperature-driven phase transitions to size-driven ones.

References

[1] Y. Cho. Nanoscale ferroelectric information storage based on scanning nonlinear dielectric microscopy. *Journal of Nanoscience and Nanotechnology*, 7:105–116, 2007.

[2] Gene H. Haertling. Ferroelectric ceramics: History and technology. *Journal of the American Ceramic Society*, 82(4):797–818, 1999.

[3] O. Auciello, J. F. Scott, and R. Ramesh. The physics of ferroelectric memories. *Physics Today*, 51(7):22–27, 1998.

[4] A. Gruverman and A. Kholkin. Nanoscale ferroelectrics: Processing, characterization and future trends. *Reports on Progress in Physics*, 69:2443–2459, 2006.

[5] N. A. Spaldin and M. Fiebig. The renaissance of magnetoelectric multiferroics. *Science*, 309:391, 2005.

[6] D. A. Scrymgeour and V. Gopalan. Nanoscale piezoelectric response across a single antiparallel ferroelectric domain wall. *Physical Review B*, 72(2):024103, 2005.

[7] T. Jungk, A. Hoffmann, and E. Soergel. Quantitative analysis of ferroelectric domain imaging with piezoresponse force microscopy. *Applied Physics Letters*, 89:163507, 2006.

[8] A. Gruverman, B. J. Rodriguez, C. Dehoff, J. D. Waldrep, A. I. Kingon, R. J. Nemanich, and J. S. Cross. Direct studies of domain switching dynamics in thin film ferroelectric capacitors. *Applied Physics Letters*, 87(8):082902, 2005.

[9] A. Ruediger, T. Schneller, A. Roelofs, S. Tiedke, T. Schmitz, and R. Waser. Nanosize ferroelectric oxides - tracking down the superparaelectric limit. *Applied Physics A*, 80:1247, 2005.

[10] A. Roelofs. *Size Effects in Ferroelectric Thin Films*. Dissertation RWTH Aachen, 2004. ISBN 3-89700-405-4.

[11] B. Peterson, S. Ducharme, V. M. Fridkin, and T. J. Reece. Mapping surface polarization in thin films of the ferroelectric polymer P(VDF-TrFE). *Ferroelectrics*, 304:51–54, 2004.

[12] M. Dawber, D. J. Jung, and J. F. Scott. Perimeter effect in very small ferroelectrics. *Applied Physics Letters*, 82(3):436–438, 2003.

[13] D. D. Fong, G. B. Stephenson, S. K. Streiffer, J. A. Eastman, O. Auciello, P. H. Fuoss, and C. Thompson. Ferroelectricity in ultrathin perovskite films. *Science*, 304:1650, 2004.

[14] M. Dawber, C. Lichtensteiger, M. Cantoni, M. Veithen, P. Ghosez, K. Johnston, K. M. Rabe, and J.-M. Triscone. Unusual behavior of the ferroelectric polarization in $\mathrm{PbTiO_3}/\mathrm{SrTiO_3}$ supperlattices. *Physical Review Letters*, 95:177601, 2005.

[15] K. Ishikawa, K. Yoshikawa, and N. Okada. Size effect on the ferroelectric phase transition in $\mathrm{PbTiO_3}$ ultrafine particles. *Physical Review B*, 37(10):5852, 1988.

[16] B. J. Rodriguez, S. Jesse, M. Alexe, and S. V. Kalinin. Spatially resolved mapping of polarization switching behavior in nanoscale ferroelectrics. *Advanced Materials*, 20:109–114, 2008.

[17] F. Peter, K. Szot, R. Waser, B. Reichenberg, S. Tiedke, and J. Szade. Piezoresponse in the light of surface adsorbates: Relevance of defined surface conditions for perovskite materials. *Applied Physics Letters*, 85(14):2896–2898, 2004.

[18] S. V. Kalinin, E. Karapetian, and M. Kachanov. Nanoelectromechanics of piezoresponse force microscopy. *Physical Review B*, 70(18):184101, 2004.

[19] F. Peter, A. Rüdiger, R. Dittmann, R. Waser, K. Szot, B. Reichenberg, and K. Prume. Analysis of shape effects on the piezoresponse in ferroelectric nanograins with and without adsorbates. *Applied Physics Letters*, 87(8):082901, 2005.

[20] K. Seal, S. Jesse, B. Rodriguez, A. P. Baddorf, and S. V. Kalinin. High frequency piezoresponse force microscopy in the 1-10 Mhz regime. *Applied Physics Letters*, 91:232904, 2007.

[21] C. Harnagea, A. Pignolet, M. Alexe, and D. Hesse. Higher-order electromechanical response of thin films by contact resonance piezoresponse force microscopy. *IEEE Transactions on ultrasonics, ferroelectrics, and frequency control*, 53(12):2309, 2006.

[22] S. Jesse, A. P. Baddorf, and S. V. Kalinin. Dynamic behaviour in piezoresponse force microscopy. *Nanotechnology*, 17:1615, 2006.

[23] Seungbum Hong, Jungwon Woo, Hyunjung Shin, Jong Up Jeon, Y. Eugene Pak, E.L. Colla, N. Setter, Eunah Kim, and Kwangsoo No. Principle of ferroelectric domain imaging using atomic force microscope. *J. Appl. Phys.* , 1998.

[24] B. Pettinger, B. Ren, G. Picardi, R. Schuster, and G. Ertl. Nanoscale probing of adsorbed species by tip-enhanced Raman spectroscopy. *Physical Review Letters*, 92:096101, 2004.

[25] B. Pettinger, X. Bao, I. C.Wilcock, M. Muhler, and G. Ertl. Surface-enhanced Raman-scattering from surface and subsurface oxygen species at microscopically well-defined Ag surfaces. *Physical Review Letters*, 72:1561, 1994.

[26] A. Hartschuh, E. J. Sanchez, X.S. Xie, and L. Novotny. High-resolution near-field Raman microscopy of single-walled carbon nanotubes. *Physical Review Letters*, 90(9):095503, 2003.

[27] L. Eng, Private Communication.

[28] F. Peter, A. Rüdiger, R. Waser, K. Szot, and B. Reichenberg. Contributions to in-plane piezoresponse on axially symmetrical samples. *Review of Scientific Instruments*, 76(10):106108, 2005.

[29] F. Jona and G. Shirane. *Ferroelectric crystals*. Clarendon Press, 1962.

[30] B. Jaffe, W.R. Cook, and H. Jaffe. *Piezoelectric ceramics*. Academic Press, 1971.

[31] M. E. Lines and A. M. Glass. *Principles and applications of ferroelectrics and related materials*. Clarendon Press, 1977.

[32] B. A. Strukov and A. Levanyuk. *Ferroelectric phenomena in crystals*. Springer, 1998.

[33] K. M. Rabe, C. H. Ahn, and J.-M. Triscone, editors. *Physics of Ferroelectrics A Modern Perspective*. Springer, 2007.

[34] J. Valasek. Piezo-electric and allied phenomena in rochelle salt. *Physical Review*, 17(4):475, 1921.

[35] C. Kittel. *Einführung in die Festkörperphysik*. R. Oldenbourg Verlag, München, Wien, 2005.

[36] L. D. Landau and E. M. Lifshitz, editors. *Statistical Physics*. Pergamon, Oxford, 1959.

[37] D. ter Haar, editor. *Collected Papers of L. D. Landau*. Pergamon, Oxford, 1965.

[38] A. F. Devonshire. Theorie of barium titanate.1. *Philosophical Magazine*, 40:1040, 1949.

[39] A. F. Devonshire. Theorie of barium titanate.2. 42:1065, 1951.

[40] A. F. Devonshire. Theorie of ferroelectrics. *Advances in Physics*, 3:85, 1954.

[41] E. Fatuzzo and W. M. Mertz, editors. *Ferroelectricity*. North-Holland, Amsterdam, 1967.

[42] W. Merz. The effect of hydrostatic pressure on the curie point of barium titanate single crystals. *Physical Review*, 78:52, 1950.

[43] P. W. Forsbergh. Effect of a two-dimensional pressure on the curie point of barium titante. *Physical Review*, 93(686), 1954.

[44] www.doitpoms.ac.uk.

[45] W. L. Zhong, B. D. Qu, P. L. Zhang, and Y. G. Wang. Thickness dependence of the dielectric susceptibility of ferroelectric thin films. *Physical Review B*, 50(17):12375, 1994.

[46] K. A. Mueller and H. Burkhard. $SrTiO_3$: An intrinsic quantum paraelectric below 4 K. *Physical Review B*, 19:3593, 1979.

[47] K. Choi, M Biegalski, Y. L. Li, A. Sharan, J. Schubert, R. Uecker, P. Reiche, Y. B. Chen, X. Q. Pan, V. Gopalan, L.-Q. Chen, D. G. Schlom, and C. B. Eom. Enhancement of ferroelectricity in strained $BaTiO_3$ thin films. *Science*, 306:1005, 2004.

[48] N. A. Pertsev, A. G. Zembilgotov, and A. K. Tagantsev. Effect of mechanical boundary conditions on phase diagrams of epitaxial ferroelectric thin films. *Physical Review Letters*, 80(9):1988–1991, 1998.

[49] Z. G. Ban and S. P. Alpay. Phase diagrams and dielectric response of epitaxial barium strontium titanate films: A theoretical analysis. *Journal of Applied Physics*, 91:9288, 2002.

[50] O. Dieguez, K. Rabe, and D. Vanderbilt. First-principles study of epitaxial strain in perovskites. *Physical Review B*, 72:144101, 2005.

[51] N. A. Pertsev and E. K. H. Salje. Thermodynamics of pseudoproper and improper ferroelastic inclusions and polycrystals: Effect of elastic clamping on phase transitions. *Physical Review B*, 61(2):902, 2000.

[52] D. Balzar, P. A. Ramakrishnan, and A. M. Hermann. Defect-related lattice strain and the transition temperature in ferroelectric thin films. *Physical Review B*, 70:092103, 2004.

[53] H. F. Kay and J. W. Dunn. Thickness dependence of the nucleation field of triglycine sulphate. *Philosophical Magazine*, 7:2027, 1962.

[54] J. F. Scott. *Ferroelectric Memories*. Springer, 2000.

[55] M. Dawber, I. Szafraniak, M. Alexe, and J. F. Scott. Self-patterning of arrays of ferroelectric capacitors: description by theory of substrate mediated strain interactions. *Journal of Physics: Condensed Matter*, 15:L667, 2003.

[56] H. K. Chan, C. H. Lam, and F. G. Shin. Time-dependent space-charge-limited conduction as a possible origin of the polarization offsets observed in compositionally graded ferroelectric films. *Journal of Applied Physics*, 95:2665, 2004.

[57] S. Ducharme, V. M. Fridkin, A. V. Bune, S. P. Palto, L. M. Blinov, N. N. Petukhova, and S. G. Yudin. Intrinsic ferroelectric coercive fields. *Physical Review Letters*, 84:175, 2000.

[58] M. Dawber, P. Chandra, P. B. Littlewood, and J. F. Scott. Depolarization corrections to the coercive field in thin-film ferroelectrics. *Journal of Physics: Condensed Matter*, 15:L393, 2003.

[59] N. A. Pertsev, J. Rodriguez Contreras, V. G. Kukhar, B. Hermanns ans H. Kohlstedt, and R. Waser. Coercive field of ultrathin $\mathrm{Pb}(\mathrm{Zr}_{0.52}\mathrm{Ti}_{0.48})\mathrm{O}_3$ epitaxial films. *Applied Physics Letters*, 83:3356, 2003.

[60] L. Lian and N. Sottos. Effects of thickness on the piezoelectric and dielectric properties of lead zirconate titanate thin films. *Journal of Applied Physics*, 87:3941, 2000.

[61] C. Basceri, S. K. Streiffer, A. I. Kingon, and R. Waser. The dielectric response as a function of temperature and film thickness of fibertextured $(\mathrm{Ba},\mathrm{Sr})\mathrm{TiO}_3$ thin films grown by chemical vapor deposition. *Journal of Applied Physics*, 82:2497, 1997.

[62] Z. Li, C.M. Foster, D. Guo, H. Zhang, G. R. Bai, P. M. Baldo, and L. E. Rehn. Growth of high quality single-domain single-crystal films of PbTiO_3. *Applied Physics Letters*, 65:1106, 1994.

[63] C. D. Theis and D. G. Schlom. Domain structure of epitaxial PbTiO_3 films grown on vicinal (001) SrTiO_3. *Journal of Material Research*, 12:1297, 1997.

[64] J. Speck, A. Seifert, W. Pompe, and R. Ramesh. Domain configuration due to multiple misfit relaxation mechanism in epitaxial ferroelectric thin films. II. Experimental verification and implications. *Journal of Applied Physics*, 76:477, 1994.

[65] A. Schilling, R. M. Bowman, J. M. Gregg, G. Catalan, and J. F. Scott. Ferroelectric domain periodicities in nanocolumns of single crystal barium titanate. *Applied Physics Letters*, 89:212902, 2006.

[66] C. Kittel. Theory of the structure of ferromagnetic domains in films and small particles. *Physical Review*, 70:965, 1946.

[67] R. Blinc and B. Žekš, editors. *Soft Modes in Ferroelectrics and Antiferroelectrics*. North-Holland, Amsterdam, 1974.

[68] C. V. Raman and T. M. K. Nedungadi. The $\alpha - \beta$ transition of quartz. *Nature*, 145(3363):147, 1940.

[69] W. Cochran. Crystal stability and the theory of ferroelectricity. *Physical Review Letters*, 3:412, 1959.

[70] S. Machlup and L. Onsager. Fluctuations and irreversible processes. 2. systems with kinetic energy. *Physical Review*, 91:1512, 1953.

[71] K. Ishikawa, K. Yoshikawa, and N. Okada. Size effect on the ferroelectric phase transition in $\mathrm{PbTiO_3}$ ultrafine particles. *Phys. Rev. B*, 37:5852, 1988.

[72] J.F. Nye. *Physical Properties of Crystals*. Clarendon Press Oxford, 1985.

[73] R. E. Newnham, V. Sundar, R. Yimnirun, J. Su, and Q. M. Zhang. Electrostriction: Nonlinear electromechanical coupling in solid dielectrics. *Journal of Physical Chemistry B*, 101:10141, 1997.

[74] K.-H. Hellwege, editor. *Landolt-Börnstein Condensed Matter III*, volume 16A. Springer-Verlag Heidelberg, 1981.

[75] C. R. Li, S. F. Cui, B. T. Liu, A. J. Zhu, X. M. Jiang, B. R. Zhao, and Z. H. Mai. Dependence of lattice constant on layer thickness of $\mathrm{Pb(Zr_{0.52}Ti_{0.48})O_3}$ thin films. *Journal of Materials Science Letters*, 17:1263, 1998.

[76] C. Pithan, Y. Shiratori, J. Dornseiffer, F.-H. Haegel, A. Magrez, and R. Waser. Microemulsion mediated synthesis of nanocrystalline $\mathrm{(K_x, Na_{1-x})NbO_3}$ powders. *Journal of Crystal Growth*, 280:191, 2005.

[77] H. Xu, Y. Su, M. L. Balmer, and A. Navrotsky. A new series of oxygen-deficient perovskites in the $\mathrm{NaTi_xNb_{1-x}O_{3-0.5x}}$ system: Crystal chemistry and energetics. *Chemical Materials*, 15:1872, 2003.

[78] R. Waser, editor. *Nanoelectronics and Information Technology*. Wiley-VCH, 2003.

[79] E. Vasco, S. Karthäuser, R. Dittmann, J.-Q. He, C.-L. Jia, K. Szot, and R. Waser. Nanopatterning using self-organized $\mathrm{SrRuO_3}$ as a template. *Advanced Materials*, 17(3):281, 2005.

[80] R. W. Schwartz, T. Schneller, and R. Waser. Chemical solution deposition of electronic oxide films. *Comptes Rendus Chimie*, 7(5):433–461, 2004.

[81] PZT9906, Chemat Technology, Inc.

[82] I. Szafraniak, C. Harnagea, R. Scholz, S. Bhattacharyya, D. Hesse, and M. Alexe. Ferroelectric epitaxial nanocrystals obtained by a self-patterning method. *Applied Physics Letters*, 83(11):2211–2213, 2003.

[83] I. Szafraniak, M.W. Chu, C. Harnagea, R. Scholz, D. Hesse, and M. Alexe. Epitaxial lead zirconate titanate nanocrystals. *Integrated Ferroelectrics*, 61:231–238, 2004.

[84] A. Ruediger, Private Communication.

[85] M. T. Buscaglia, V. Buscaglia, and R. Alessio. Coating of $BaCO_3$ crystals with TiO_2: Versatile approach to the synthesis of $BaTiO_3$ tetragonal nanoparticles. *Chemistry of Materials*, 19:711, 2007.

[86] M. T. Buscaglia, V. Buscaglia, M. Viviani, G. Dondero, S. Röhrig, A. Rüdiger, and P. Nanni. Ferroelectric hollow particles by solid-state reaction. fabrication and properties. *Nanotechnology*, 19:225602, 2008.

[87] Y. Shiratori, A. Magrez, J. Dornseifferand, F.-H. Haegel, C. Pithan, and R. Waser. Polymorphism in micro-, submicro-, and nanocrystalline $NaNbO_3$. *Journal of Physical Chemistry B*, 109(43):20122, 2005.

[88] T. Jungk, Á. Hoffmann, and E. Soergel. Consequences of the background in piezoresponse force microscopy on the imaging of ferroelectric domain structures. *Journal of Microscopy*, 227:72, 2007.

[89] K. Szot, editor. *Probing the Nanoworld*. Forschungszentrum Jülich, 2007.

[90] K. Prume, A. Roelofs, T. Schmitz, B. Reichenberg, S. Tiedke, and R. Waser. Compensation of the parasitic capacitance of a scanning force microscope cantilever used for measurements on ferroelectric capacitors of submicron size by means of finite element simulations. *Japanese Journal of Applied Physics*, 41(1):7198–7201, 2002.

[91] I. Szafraniak, S. Bhatracharyya, C. Harnagea, R. Scholz, and M. Alexe. Self-assembled ferroelectric nanostructures. *Integrated Ferroelectrics*, 68:279–286, 2004.

[92] M. Alexe, Private Communication.

[93] Y. Saito, H. Takao, T. Tani, T. Nonoyama, K. Takatori, T. Homma, T. Nagaya, and M. Nakamura. Lead-free piezoceramics. *Nature*, 432:84, 2004.

[94] Y. Shiratori, A. Magrez, K. Kasezawa, M. Kato, S. Röhrig, F. Peter, C. Pithan, and R. Waser. Noncentrosymmetric phase of submicron $NaNbO_3$ crystallites. *Journal of Electroceramics*, 19:273, 2007.

[95] K.-H. Hellwege, editor. *Landolt-Börnstein Condensed Matter III*, volume 36A1. Springer-Verlag Heidelberg, 1981.

[96] H. Fujisawa, M. Okaniwa, H. Nonomura, M. Shimizu, and H. Niu. Ferroelectricity of the 1.7 nm-high and 38 nm-wide self-assembled $PbTiO_3$ island. *Journal of the European Ceramic Society*, 24(6):1641–1645, 2004.

[97] A. Roelofs, T. Schneller, K. Szot, and R. Waser. Towards the limit of ferroelectric nanosized grains. *Nanotechnology*, 14(2):250–253, 2003.

[98] F. Peter, J. Kubacki, K. Szot, B. Reichenberg, and R. Waser. Influence of adsorbates on the piezoresponse of $KNbO_3$. *phys. stat. sol. (a)*, 203(3):616–624, 2006.

[99] C. Harnagea, A. Pignolet, M. Alexe, and D. Hesse. Piezoresponse scanning force microscopy: What quantitative information can we really get out of piezoresponse measurements on ferroelectric thin films? *Integrated Ferroelectrics*, 44:113–124, 2002.

[100] M. Abplanalp, editor. *Piezoresponse scanning force microscopy of ferroelectric domains*.

[101] J. Halbritter. Charge transfer via interfaces, especially of nanoscale materials. *Applied Physics A: Materials Science and Processing*, 68:153–162, 1999.

[102] S. V. Kalinin and D. A. Bonnell. Local potential and polarisation screening on ferroelectric surfaces. *Physical Review B*, 63:125411, 2001.

[103] F. Peter, A. Rüdiger, R. Waser, K. Szot, and B. Reichenberg. Comparison of in-plane and out-of-plane optical amplification in AFM measurements. *Review of Scientific Instruments*, 76:046101, 2005.

[104] M. Alexe, C. Harnagea, D. Hesse, and U. Gösele. Polarization imprint and size effects in mesoscopic ferroelectric structures. *Applied Physics Letters*, 79(2):242–244, 2001.

[105] Frank Peter. *Piezoresponse Force Microscopy and Surface Effects of Perovskite Ferroelectric Nanostructures*. Dissertation RWTH Aachen, 2006. ISBN 3-89336-444-7.

[106] Y. Cho, S. Hashimoto, N. Odagawaand K. Tanaka, and Y. Hiranaga. Realization of 10 Tbit/in^2 memory density and subnanosecond domain switching time in ferroelectric data storage. *Applied Physics Letters*, 87:232907, 2005.

[107] G. Le Rhun, I. Vrejoiu, and M. Alexe. Piezoelectric response hysteresis in the presence of ferroelastic 90^o domain walls. *Applied Physics Letters*, 90:012908, 2007.

[108] J. A. Christman, S.-H. Kim, H. Maiwa, J.-P. Maria, B. J. Rodriguez, A. I. Kingon, and R. J. Nemanich. Spatial variation of ferroelectric properties in $\mathrm{Pb}(\mathrm{Zr}_0.3, \mathrm{Ti}_0.7)\mathrm{O}_3$ thin films studied by atomic force microscopy. *Journal of Applied Physics*, 87(11):8031–8034, 2000.

[109] M. Abplanalp, L.M. Eng, and P. Günter. Mapping the domain distribution at ferroelectric surfaces by scanning force microscopy. *Applied Physics A: Materials Science & Processing*, 66(0):S231, 1998.

[110] P. Gerber, C. Kügeler, U. Böttger, and R. Waser. Effects of ferroelectric switching on the piezoelectric small-signal response d_{33} and electrostriction M_{33} of lead zirconate titanate thin films. *Journal of Applied Physics*, 95:4976, 2004.

[111] F. Peter, A. Rüdiger, R. Waser, K. Szot, and B. Reichenberg. Comparison of in-plane and out-of-plane optical amplification in AFM measurements. *Review of Scientific Instruments*, 76(4):046101, 2005.

[112] C. L. Jia, M. Lentzen, and K. Urban. Atomic-resolution imaging of oxides in perovskite ceramics. *Science*, 299:870, 2003.

[113] P. M. Voyles, D. A. Muller, J. L. Grazul, P. H. Citrin, and H.-J. L. Gossmann. Atomic-scale imaging of individual dopant atoms and clusters in highly n-type bulk Si. *Nature*, 416:826, 2002.

[114] M. Abplanalp and P. Gunter. Influence of stress on the domain formation in barium-titanate films. *Ferroelectrics*, 258, 2001.

[115] L. M. Eng, H.-J. Güntherodt, G. Rosenman, A. Skliar, M. Oron, M. Katz, and D. Eger. Nondestructive imaging and characterization of ferroelectric domains in periodically poled crystals. *Journal of Applied Physics*, 83(11):5973–5977, 1998.

[116] B. J. Rodriguez, A. Gruverman, A. I. Kingon, R. J. Nemanich, and J. S. Cross. Three-dimensional high-resolution reconstruction of polarization in ferroelectric capacitors by piezoresponse force microscopy. *Journal of Applied Physics*, 95(4):1958–1962, 2004.

[117] K.-H. Hellwege and A. M. Hellwege, editors. *Landolt-Börnstein: Numerical Data and Functional Relationships in Science and Technology*, volume 16. Springer-Verlag Heidelberg, 1981.

[118] H. P. Sun, W. Tian, X. Q. Pan, J. H. Haeni, and D. G. Schlom. Evolution of dislocation arrays in epitaxial $BaTiO_3$ thin films grown on (100) $SrTiO_3$. *Applied Physics Letters*, 84(17):3298–3300, 2004.

[119] U. Poppe, J. Schubert, R.R. Arons, W. Evers, C. H. Freiburg, W. Reichert, K. Schmidt, W. Sybertz, and K. Urban. Direct production of crystalline superconducting thin-films of $YBa_2Cu_3O_7$ by high-pressure oxygen sputtering. *Solid State Communications*, 66:661, 1988.

[120] A. Petraru, N. A. Pertsev, H. Kohlstedt, U. Poppe, R. Waser, A. Solbach, and U. Klemradt. Polarization and lattice strains in epitaxial $BaTiO_3$ films grown by high-pressure sputtering. *Journal of Applied Physics*, 101:114106, 2007.

[121] J.T.M. De Hosson and B.J. Kooi, editors. *Handbook of Surfaces and Interfaces in Materials*. Academic Press, New York, 2001.

[122] H. Kohlstedt, A. Petraru, K. Szot, A. Ruediger, P. Meuffels, H. Haselier, R. Waser, and V. Nagarajan. Method to distinguish ferroelectric from nonferroelectric origin in case of resistive switching in ferroelectric capacitors. *Applied Physics Letters*, 92:062907, 2008.

[123] C. V. Raman and K. S. Krishnan. A new type of secondary radiation. *Nature*, 121:501, 1928.

[124] C. V. Raman. A change of wave-lenght in light scattering. *Nature*, 121:619, 1928.

[125] C. V. Raman and K. S. Krishnan. The optical analogue of the compton effect. *Nature*, 121:711, 1928.

[126] N. Peica. *Vibrational spectroscopy and density functional theory calculations on biological molecules*. Dissertation Universität Würzburg, 2006.

[127] M. Fleischmann and P. J. Hendra amd A. J. McQuilian. Raman spectra of pyridine adsorbed at a silver electrode. *Chemical Physics Letters*, 26:163, 1974.

[128] V. M. Shalaev and A. K. Sarychev. Non-linear optics of random metal-dielectric films. *Physical Review B*, 57:13265, 1998.

[129] V. M. Shalaev. Optical nonlinearities of fractal composites. *Optical Properties of Nanostructured Random Media*, 82:93, 2002.

[130] M. Moskovits and D. H. Jeong. Engineering nanostructures for giant optical fields. *Chemical Physics Letters*, 397:91, 2004.

[131] M. L. Brongersma and P. G. Kik. *Surface Plasmon Nanophotonics*. Springer, 2007.

[132] V. G. Bordo and H.-G. Rubahn. *Optics and Spectroscopy at Surfaces and Interfaces*. Wiley-VCH, 2005.

[133] A. Otto. Surface-enhanced Raman scattering of adsorbates. *Journal of Raman Spectroscopy*, 22:743, 1991.

[134] A. Otto. Theory of first layer and single molecule surface-enhanced Raman scattering (SERS). *Physica Status Solidi (a)*, 188:1455, 2001.

[135] M. I. Stockman, V. M. Shalaev, M. Moskovits, R. Botet, and T. F. George. Enhanced Raman scattering by fractal clusters-scale invariant theory. *Physical Review B*, 46:2821, 1992.

[136] D. G. W. Goad and M. Moskovits. Colloidal metal in aluminium oxide. *Journal of Applied Physics*, 49:2929, 1978.

[137] G. Picardi. *Raman spectroscopy and light emission at metal surfaces enhanced by the optical near field of a scanning tunneling tip*. Freie Universität Berlin, 2003.

[138] L. Novotny, R. X. Bian, and X. S. Xie. Theory of nanometric optical tweezers. *Physical Review Letters*, 79:645, 1997.

[139] A. Bouhelier, M. Beversluis A. Hartschuh, and L. Novotny. Near-field second-harmonic generation induced by local field enhancement. *Physical Review Letters*, 90:13903, 2003.

[140] J. Wessel. Surface-enhanced optical microscopy. *Journal of the Optical Society of America B*, 2:1538, 1985.

[141] B. Pettinger, B. Ren, G. Picardi, R. Schuster, and G. Ertl. Tip-enhanced Raman spectroscopy (TERS) of malachite green isothiocyanate at Au(111): Bleaching behavior under the influence of high electromagnetic fields. *Journal of Raman Spectroscopy*, 36:541, 2005.

[142] A. Downes, D. Salter, and A. Elfick. Simulations of tip-enhanced optical microscopy reveal atomic resolution. *Journal of Mocroscopy*, 229:184, 2008.

[143] F. Festy, A. Demming, and D. Richards. Resonant excitation of tip plasmons for tip-enhanced Raman SNOM. *Ultramicroscopy*, 100:437, 2004.

[144] R. J. C. Brown, J. Wang, R. Tantra, R. E. Yardley, and M. J. T. Milton. Electromagnetic modelling of Raman enhancement from nanoscale substrates: A route to estimation of the magnitude of the chemical enhancement mechanism in SERS. *Faraday Discussions*, 132:201, 2006.

[145] I. Notingher and A. Elfick. Effect of sample and substrate electric properties on the electric field enhancement at the apex of SPM nanotips. *Journal of Physical Chemistry B*, 109:15699, 2005.

[146] K. F. Domke. *Tip-enhanced Raman spectroscopy - Topographic and chemical information on the nanoscale*. Freie Universität Berlin, 2006.

[147] R.W. Rendell and D. J. Scalapino. Role of local plasmon modes in light emission from small-particle tunnel junctions. *The American Physical Society*, 41:1746, 1928.

[148] A. Otto. Excitation of nonradiative surface plasma waves in silver by method of frustrated total reflection. *Zeitschrift für Physik*, 216:398, 1968.

[149] E. Kretschmann and H. Raether. Radiative decay of nonradiative surface plasmons excited by light. *Zeitschrift für Naturforschung A*, 23:2135, 1968.

[150] http://monet.unibas.ch/ bouhelie/plasmon1.html.

[151] H. Raether. *Surface Plasmons on Smooth and Rough Surfaces and on Gratings*. Springer-Verlag, Berlin, 1988.

[152] J. Stratton. *Electromagnetic Theory*. Mc Graw-Hill Book Company, New York, 1941.

[153] PointProbe tips obtained from Nanosensors.

[154] C. Chin, L. J. Guo, and B. Lucas. Fabrication of metallic nanoparticle arrays. *The Journal of Young Investigators*, 16, 2008.

[155] V. Deckert, Private Communication.

[156] Coherent BeamMasterPC manual.

[157] A. E. Siegman. *Lasers*. University Science Books Stanford, 1986.

[158] Schäfter und Kirchhoff Polarimeter manual.

Acknowledgements

First I am greatly indebted to Prof. Dr. R. Waser for giving me the opportunity to do research at the *Institut für Festkörperforschung* of the *Forschungszentrum Jülich,* Germany in the exciting field of nanoscale ferroelectrics. I would like to thank him for giving me the freedom and resources from which I greatly benefited.

I am also indebted to Prof. Dr. S. Tautz who kindly agreed to be the co-examiner.

I am immensely grateful and deeply indebted to my supervisor Dr. A. Rüdiger for his inspiration and enthusiasm, his guidance and the tremendous support.

Furthermore I would like to thank Prof. Dr. A. Gruverman from the North Carolina State University and Dr. B Pettinger from the Department of Physical Chemistry of the Fritz-Haber-Institute, Berlin, for the fruitful discussions.

V. Buscaglia from Institute of Energetics and Interphases at the National Research Council, Genova for the cooperation

Dr. F. Peter for introducing me into the fascinating world of AFM and especially PFM and for discussions and support. H. John for support on setting up the measurement equipment. Dr. R. Dittmann, Dr. A. Petraru, Dr. T. Schneller, S. Clemens, Dr. I. Szafraniak and Dr. M. Alexe for providing samples Dr. N. Peica for her support with tip-enhanced Raman spectroscopy. My colleagues: Lars Müller-Meskamp, Sebastian Albiez, Christian Nauenheim, Christina Schindler, Marcel Gerst, Martin Weides, Peter Kowalzik, Rohit Soni and everyone else at the *Institut für Festkörperforschung,* and the *Institut für Werkstoffe der Elektrotechnik 2* of the *RWTH Aachen* for their help and support.

I am grateful to my family and parents for their encouragement and support.

Schriften des Forschungszentrums Jülich
Reihe Information / Information

1. **Ferrocenes as Potential Building Blocks for Molecular Electronics**
   Self-Assembly and Tunneling Spectroscopy
   by L. Müller-Meskamp (2008), 153 pages
   ISBN: 978-3-89336-509-8

2. **Magnetic Proximity Effects in Highly-ordered Transition Metal Oxide Heterosystems studied by Soft x-Ray Photoemission Electron Microscopy**
   by I. P. Krug (2008), XX, 180 pages
   ISBN: 978-3-89336-521-0

3. **Seltenerd-basierte ternäre Oxide als alternative Gatedielektrika**
   von J. M. Roeckerath (2008), 148 Seiten
   ISBN: 978-3-89336-543-2

4. **Strominduzierte Magnetisierungsdynamik in einkristallinen Nanosäulen**
   von R. Lehndorff (2009), I, 86 Seiten
   ISBN: 978-3-89336-564-7

5. **Magnetization Dynamics in Magnetically Coupled Heterostructures**
   von A. Kaiser (2009), X, 121 Seiten
   ISBN: 978-3-89336-577-7

6. **Resistive switching in Pt/TiO_2/PT**
   by D. S. Jeong (2009), vii, 133 pages
   ISBN: 978-3-89336-579-1

7. **Electromechanical Force Microscopy and Tip-Enhanced Raman Spectroscopy for Polar Oxide Nanoparticles**
   by S. Röhrig (2009), vi, 114 pages
   ISBN: 978-3-89336-600-2

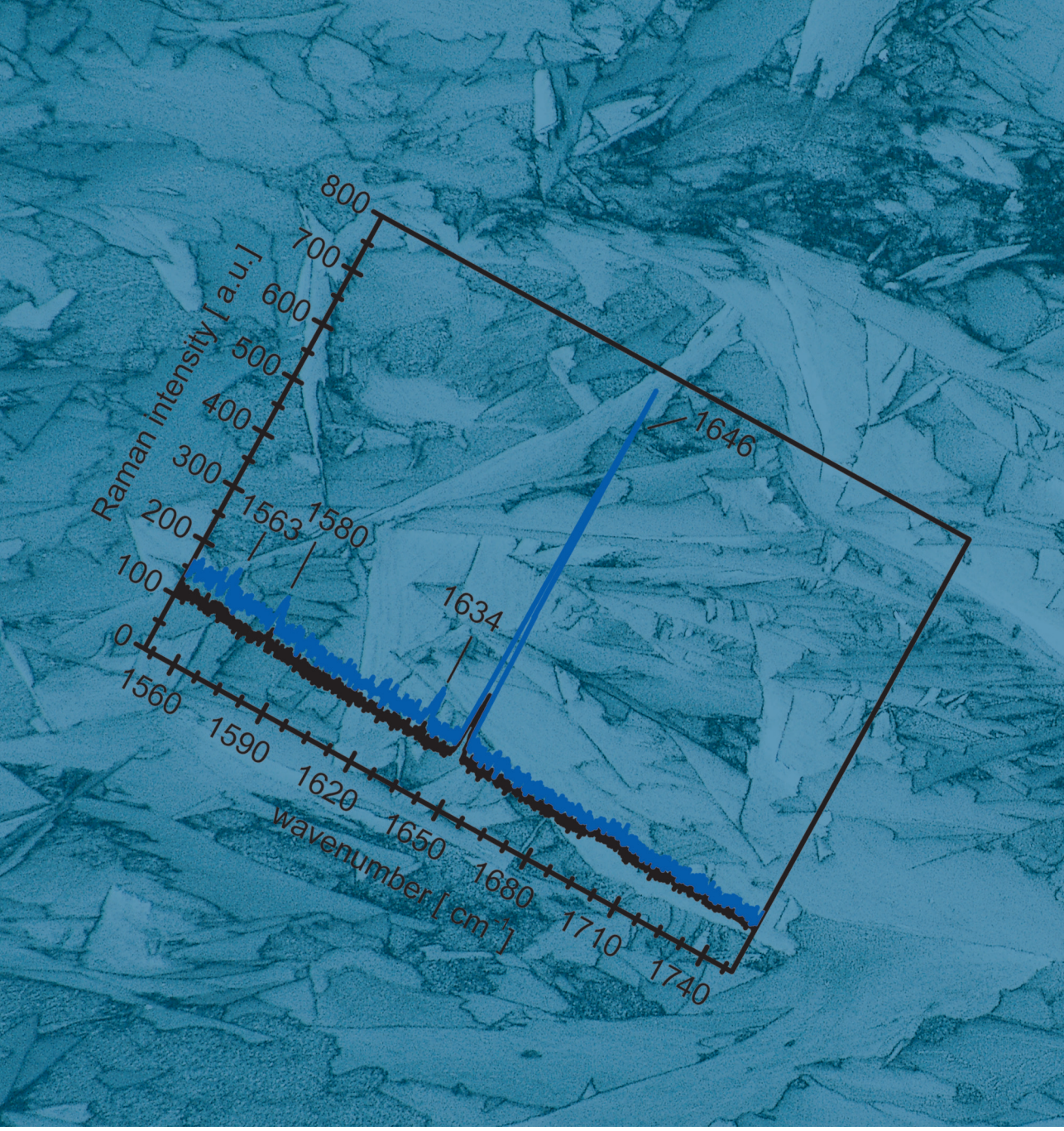

Information / Information
Band / Volume 7
ISBN 978-3-89336-600-2

JÜLICH
FORSCHUNGSZENTRUM